Erythrocyte aggregates dynamics under pathophysiological conditions

Mehdi Abbasi

THÈSE

Pour obtenir le grade de

DOCTEUR DE L'UNIVERSITÉ GRENOBLE ALPES

École doctorale : PHYS - Physique
Spécialité : Physique pour les Sciences du Vivant
Unité de recherche : Laboratoire Interdisciplinaire de Physique

Dynamique des agrégats érythrocytaires dans des conditions physiopathologiques

Erythrocyte aggregates dynamics under pathophysiological conditions

Présentée par :

Mehdi ABBASI

Direction de thèse :

Chaouqi MISBAH DIRECTEUR DE RECHERCHE, Université Grenoble Alpes	Directeur de thèse
Alexander FARUTIN CHARGE DE RECHERCHE, Université Grenoble Alpes	Co-encadrant de thèse

Rapporteurs :

MARC LEONETTI
Directeur de recherche, CNRS DELEGATION PROVENCE ET CORSE
STEPHAN GEKLE
Professeur, Universität Bayreuth

Thèse soutenue publiquement le **19 décembre 2022**, devant le jury composé de :

MARC LEONETTI Directeur de recherche, CNRS DELEGATION PROVENCE ET CORSE	Rapporteur
STEPHAN GEKLE Professeur, Universität Bayreuth	Rapporteur
CHRISTIAN WAGNER Professeur, Universität des Saarlandes	Examinateur
PHILIPPE PEYLA Professeur des Universités, UNIVERSITE GRENOBLE ALPES	Président

Erythrocyte aggregates dynamics under pathophysiological conditions.

Mehdi Abbasi

Laboratoire Interdisciplinaire de Physique Grenoble

Université Grenoble Alpes

A thesis submitted for the degree of

Doctor of Physics

December 19, 2022

Acknowledgements

First of all, I would like to thank my two thesis supervisors for their wise advices and their support throughout the duration of this thesis. Thank you for devoting the time to listening and guiding the young bioinformatician/physicist that I was towards a field where mathematics, physics and biology complement each other (at least in theory) in an attempt to unravel the mysteries of life at scale. microscopic.

I am particularly grateful to Abdelillah Benyoussef and Hamid Ez-Zahraouy, of the faculty of sciences of Rabat for their supports and guidance during my studies in the University of Mohammed 5 and specially on the topic of blood flow, I also thank them for the inspirations and encourage- ment in many fruitful communications.

Special thanks to Mr Philippe Peyla who did me the honor of chairing the Jury, to Mrs Marc Leonetti, Stephan Gekle, Christian Wagner, Alexander Farutin and Chaouqi Misbah for their participation in the Jury and the stimulating discussion that followed the defense. I address all my gratitude to the rapporteurs Stephan and Gekle, Marc Leonetti who, through their remarks and suggestions, have participated in improving the quality of this work which, in my eyes and in its current version, remains unfinished (for lack of time).

I am very grateful to my collegues and friends of LIPhy: Suhail, Abdessamad, Hengdi, Mariam, Ananta, Zhe, Min, Haythem, George, Dalal, Priti, Gopal and Somnath for their contributions, advice throughout this thesis, and the nice time we shared together.

I had the opportunity to have a good environment of researchers, engineers and technicians who helped me a lot during the thesis, I thank Salima, Lionel, Gwennou, Marc, Philippe, Claude, Daria, Mathilde, Philippe, Vikhram and Daniel. Many thanks to Kristina, Chantal, Sabine, Nadine and Sandrine for their administrative help.

I would like to thank the members of the thesis follow-up committee: Lionel Bureau, Marc Leonetti and Emmanuel Bossy (my thesis tutor) for their availability, support and advice during the difficult times of the thesis.

Thank you very much my dear friends Yassine, Zineb, Rachid, Ikram, Jebril (my lovely cousin), Imane, Reda, Ahmed, Adam, Chaimae, Salah, Mariam (Thank you for the good time we shared in our office), Marouane, Sara, Mohammed, Youssef, Mamoune, Mehdi, Majda, Imad, Rana, Hind, Omar, Salwa, Othmane (support and help from Nuremberg) and Selma. With these lovely people, my life is enjoyable. And I'm sorry if I forgot a name.

Finally, I would like to thank all my family members who gave me an atmosphere full of love and encouragement.

I dedicate this thesis to my dear parents and my lovely family.

Abstract

Blood is a complex fluid, and the major components of which are red blood cells (RBCs). Under healthy conditions the flow properties are dictated by RBCs. However, in several diseases, other components may enter into play, such as platelet activation, fibrin formation (a network of fibrinogen, a plasma protein), and may compromise blood flow, leading potentially to blood occlusions. Occlusions can be due to thrombus formation (a collection of platelets, RBCs, and fibrin network, ...). They can also be due only to clusters of RBCs, as happens in diabetes, where occlusion in microcirculation can lead to ischemia and several pathologies may follow (like retinopathy, nephropathy, and neuropathy). Therefore, understanding the basic mechanisms of RBCs aggregation is crucial not only for fundamental reasons, but also for potentially identifying its link to pathologies.

The formation of RBCs aggregates is due to plasma proteins (e.g. fibrinogen), but several other factors may affect the aggregation processes such as (i) physical properties of RBCs (like mechanical properties) (ii) a structural alteration (example: glycoproteins) of the surface of RBCs, (iii) the internal composition of RBCs (like in malaria), etc... This thesis aim is to contribute to the understanding of dynamics and rheology of RBC aggregates. We adopted 2D vesicle and 3D capsule model to mimic RBCs. We first decided to analyze the role of cytoskeleton in dynamics of a single RBC. We showed that many shapes, and especially multilobe shapes, do not need cytoskeleton, in contrast to several recent claims. These shapes are observed here for a 2D vesicle and are only due to membrane tension. This preliminary study provides further confidence in the importance of 2D model, albeit several studies on 3D are also presented regarding aggregation. For aggregation, we have analyzed both low and high hematocrit situations. In addition to simulations, we carried out microfluidic experiments in order to identify the role of glycoproteins in the aggregation process. Using boundary integral formulation

in 2D and lattice Boltzmann method in 3D, we produced a rich phase diagram of RBC-RBC doublet aggregate configurations showing features never evoked before. In particular, we showed that RBCs doublet may be robust even for very high shear stress compromising oxygen delivery to organs and tissues. We provided an explanation for the resistance of RBCs doublet to the dissociation at high shear stress and we highlighted the important role of the membrane tank-treading on the RBCs doublet disaggregation. It is believed that under physiological conditions, the aggregates form in a reversible way. At high enough viscosity contrast (the ratio between the inner and outer fluid viscosities of the membrane), the aggregation process is irreversible: once the aggregates form they acquire strong stability, in that they resist to very high shear stress (even for the highest values of shear stress encountered in microcirculation –arterioles). Analyzing RBCs flow at various hematocrits (Ht), we described in details the RBCs flux as a function of Ht and flow strength. We showed that a weak enough adhesion can boost transport of RBCs to a level attaining up 30% in comparison to the case without adhesion. A higher adhesion energy leads to a collapse of RBCs flux (lower perfusion rate). Finally, we focused on an experimental study by analyzing the role of glycocalyx cleavage in the aggregation process. We used an enzyme (amylase) to cleave glycocalyx. We found a large increase of aggregation size, a modification of shape aggregate (they are more rounded, as compared to classical rouleaux), and an increase in stability against shear stress. This finding may contribute to deciphering the origin of vascular complications due to glycocalyx cleavage, such as in diabetes.

Keywords: Simulation, microfluidic experiments, red blood cells, adhesion, rheology, cardiovascular diseases.

Résumé

Le sang est un fluide complexe dont les principaux composants sont les globules rouges. Dans les conditions physiologiques, les propriétés d'écoulement sont controlées par les globules rouges. Cependant, dans plusieurs cas de maladies cardiovasculaires, d'autres composants peuvent entrer en jeu, tels que l'activation plaquettaire, la formation de fibrine (par polymérisation de fibrinogène, une protéine plasmatique), et peuvent affecter le flux sanguin, entraînant potentiellement des occlusions sanguines. Les occlusions peuvent être dues à la formation de thrombus (une collection de plaquettes, de globules rouges et de réseau de fibre de fibrine, ...). Elles peuvent également être dus uniquement à des amas de globules rouges, comme cela se produit dans le diabète, où l'occlusion de la microcirculation peut entraîner une ischémie et plusieurs pathologies peuvent suivre (comme la rétinopathie, la néphropathie et la neuropathie). Par conséquent, comprendre les mécanismes de base de l'agrégation des globules rouges est crucial non seulement pour des raisons fondamentales, mais aussi pour identifier potentiellement ses liens avec les pathologies.

La formation des agrégats de globules rouges est due aux protéines plasmatiques (par exemple, le fibrinogène), mais plusieurs autres facteurs peuvent affecter les processus d'agrégation tels que (i) les propriétés physiques des globules rouges (comme les propriétés mécaniques) (ii) une altération structurale (exemple : les glycoprotéines) de la surface des globules rouges, (iii) la composition interne des globules rouges (comme dans le paludisme), etc... Cette thèse a pour objectif de contribuer à la compréhension de la dynamique et de la rhéologie des agrégats de globules rouges. Nous avons adopté un modèle de vésicule 2D et de capsule 3D pour mimer les globules rouges. Nous avons d'abord décidé d'analyser le rôle du cytosquelette dans la dynamique d'un seul globule rouge. Nous avons montré que de nombreuses formes, et en particulier les formes multilobes, n'ont pas besoin de cytosquelette, contrairement à plusieurs affirmations récentes. Ces formes

sont observées ici pour une vésicule 2D et ne sont dues qu'à la tension membranaire. Cette étude préliminaire renforce ll'importance du modèle 2D, bien que plusieurs études en 3D soient également présentées ici au sujet de l'agrégation. Pour l'agrégation des globules rouges, nous avons analysé les situations d'hématocrite faible et élevé. En plus des simulations, nous avons réalisé des expériences microfluidiques afin d'identifier le rôle des glycoprotéines dans le processus d'agrégation. En utilisant la formulation des intégrales aux frontières en 2D et la méthode de Boltzmann en réseau en 3D, nous avons produit un diagramme de phase riche des configurations d'agrégats de doublets dee globules rouges montrant des caractéristiques jamais évoquées auparavant. En particulier, nous avons montré que le doublet de globules rouges peut être robuste même pour des contraintes de cisaillement très élevées compromettant l'apport d'oxygène aux organes et aux tissus. Nous avons fourni une explication de la résistance du doublet de globules rouges à la dissociation à forte contrainte de cisaillement et nous avons mis en évidence le rôle important du tank-treading de la membrane sur la désagrégation du doublet de globules rouges. On pense que dans des conditions physiologiques, les agrégats se forment de manière réversible. A un contraste de viscosité suffisamment élevé (le rapport entre les viscosités fluides interne et externe de la membrane), le processus d'agrégation est irréversible : une fois les agrégats formés, ils acquièrent une forte stabilité, en ce sens qu'ils résistent à des contraintes de cisaillement très élevées (même pour les valeurs les plus élevées des contraintes de cisaillement rencontrées dans la microcirculation –artérioles). En analysant le flux de globules rouges à divers hématocrites (Ht), nous avons décrit en détail le flux de globules rouges en fonction de Ht et de la force d'écoulement. Nous avons montré qu'une adhérence suffisamment faible peut augmenter le transport des globules rouges à un niveau atteignant jusqu'à 30 % par rapport au cas sans adhérence. Une énergie d'adhésion plus élevée entraîne un effondrement du flux de globules rouges (taux de perfusion plus faible). Pour terminer, nous nous sommes concentrés sur une étude expérimentale en analysant le rôle de la dégradation du glycocalyx dans le processus d'agrégation. Nous avons utilisé une enzyme (amylase) pour cliver le glycocalyx. Nous avons trouvé une forte augmentation de la taille des agrégats, une modification de la forme des agrégats (ils sont plus arrondis, par rapport aux rouleaux classiques),

et une augmentation de la stabilité contre les contraintes de cisaillement. Cette découverte peut contribuer à déchiffrer l'origine des complications vasculaires dues à la dégradation du glycocalyx, comme dans le diabète.

Mots clés : Simulation, expériences microfluidiques, globules rouges, adhésion, rheologie, maladies cardiovasculaires.

Table des matières

Table des figures

Liste des tableaux

Chapitre 1

Introduction

In this chapter, a brief review of human blood, its components and blood vessels are given in Section 1.1. In section 1.2 the red blood cells aggregation phenomenon is described as well as the known theoretical models that explain the adhesion between red blood cells. Section 1.4 is dedicated to present the main contributions of this thesis.

1.1 Brief review on blood flow

Blood is a complex fluid, about 55% of its volume consists of plasma and 45% is composed of red blood cells (RBCs) called also erythrocytes, whereas white blood cells and platelets together account for less than 1%. The RBCs are responsible for oxygen transport from lungs to the tissues and the removal of the carbon dioxide from the tissues to the lungs. RBCs are not oxygen carriers only, but also they transport several other chemical species, the most prominent of which is Adenosine triphosphate (ATP), playing a pivotal role in blood flow regulation via a complex biochemical signaling involving endothelial cells (which cover the internal face of all vessels) [Schwiebert and Zsembery, 2003, Zhang et al., 2018a]. At equilibrium, a healthy RBC adopts a biconcave shape with a diameter $8\mu m$ and a thickness of $2.5\mu m$ as shown in figure. The volume of a single RBC is about $90\mu m^3$ and its surface is about $130\mu m^2$ [Tomaiuolo, 2014]. Blood flow is highly affected by RBCs properties, their deformation, the interactions among cells as well as with blood vessels. Blood is pumped by the heart through blood vessels that are classified as either arteries, capillaries and veins. Arteries are the blood vessel that transport blood rich in oxygen away from heart, where they diverge into smaller vessels. The smallest arteries called arterioles that branch into capillaries, where wastes and nutrients are exchanged in organs and tissues. The capillaries are combined to form venules that transport blood to the veins,

returning carbon dioxide-rich blood to the heart [Betts et al., 2013]. Table 1.1 summarizes the diameter and mean velocity of arterioles, venules and capillaries, as our study will focus on small scales, relevant for microvasculature.

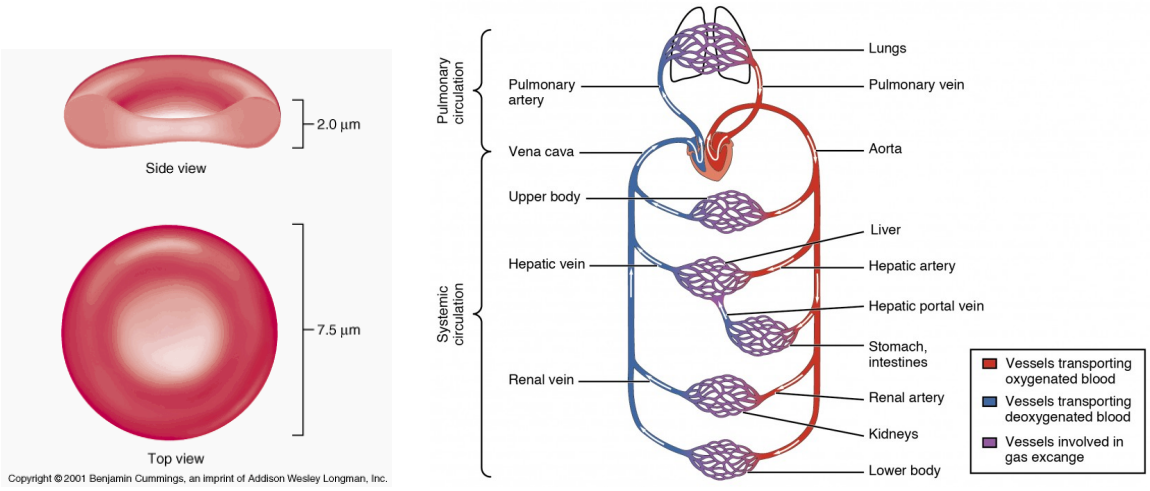

FIGURE 1.1 : Left : Red blood cell. Right : Blood vessels.

	Diameter (μm)	Mean velocity (mm/s)
Arterioles	60 - 15	12 - 7
Capillaries	5	0.2
Venules	72 - 18	2.4 - 0.2

TABLE 1.1 : Typical micro-circulatory parameters [Popel and Johnson, 2005].

The blood vessels have slightly the same structures. The inner surface of the all types of vessels is covered with mono-layer of cells called endothelial cells. The endothelium (the monolayer of endothelial cells) is considered as an organ. The endothelial cells cover all the vessels from heart to tissues and they are involved in vascular diseases, diabetes, tumor growth, heart diseases, venous thrombosis and many more [Rajendran et al.,]. Endothelial cells play a central role for many molecular exchanges between blood and tissues, they control the regulation of blood homeostasis, vascular health and immune system.

Endothelial cell (EC) and RBCs surface are both covered by a layer of brushy glycoprotein called glycocalyx [Jiang et al., 2021] as shown in Fig .1.2. The glycocalyx plays many roles in cell signaling and adhesion between cells. The glycocalyx is known to be charged negatively. The electrical negative charge enhance the repulsion

between RBCs and between RBCs and endothelial cells. An alteration of the glycocalyx, as suspected in some cardiovascular diseases, may results in enhancement of blood aggregats and strong interaction between RBCs and endothelial cells.

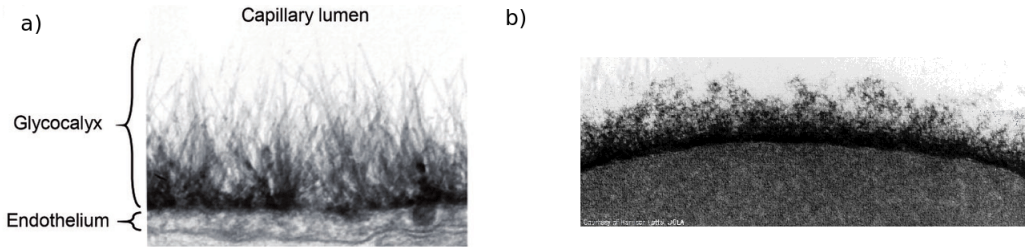

FIGURE 1.2 : Electron microcopy showing the glycocalyx. a) endothelial cells [Oshima et al., 2017] b) RBC (*https ://www3.nd.edu/ aseriann/CHAP12B.html/sld071.htm*), .

1.2 Red blood cells aggregation

RBCs have a tendency to form aggregates that initially consist of face-to-face linear structures that resemble a stack or roll of coins. Several cardiovascular dysfunctions and RBC anomalies may impair proper blood perfusion of the organism. For example, drepanocytosis [Di Liberto and Bartolucci, 2016, Lemonne and Etienne-Julan, 2012], which results in a stiff cytoplasm of RBCs under low oxygen conditions, compromises a proper RBC flow in small blood vessels due to a formation of occlusions. In several blood diseases, such as diabetes and hypercholesterolemia, as well as coronary heart disease, an enhanced tendency of RBCs to form aggregates [Groeneveld et al., 1999, Prasad and Kalra, 1993, Lugovtsov et al., 2019, Razavian et al., 1994, Kaul, 2008, Potron et al., 1994, Dunn and Ariëns, 2004, Fusman et al., 2002] has been reported. Fibrinogen (a protein contained in plasma) is the main cause of adhesion between RBCs [Brust et al., 2014]. Under physiological conditions the range of human fibrinogen level is approximately 1.8 - 4 mg/ml [Comeglio et al., 1996], and RBCs aggregate and disaggregate reversibly under flow. In contrast, under pathological conditions the level of fibrinogen may become high enough leading to more stable aggregates [Razavian et al., 1992, Dunn and Ariëns, 2004]. Foresto et al [Foresto et al., 2000] compared the aggregability of RBCs from diabetic and healthy patients, using direct microscopic observation and numerical processing. They found that the RBCs aggregation is highly enhanced in the case of diabetic patients compared to healthy patients. It has been documented [Rogers et al., 1992, Mazzanti et al., 1997] that within these patients a degradation of the glycoprotein surface of the RBC membrane (which controls the

electrical as well as steric repulsion between RBCs) favors aggregation. In addition, it has been reported that under pathological conditions, such as diabetes and drepanocytosis, the fibrinogen concentration may be significantly higher than for the normal range [Razavian et al., 1992, Dunn and Ariëns, 2004, Potron et al., 1994]. It is to be noted also that blood from pregnant women shows an important aggregability level which is correlated with a high fibrinogen concentration [Huisman et al., 1988]. It seems thus that enhanced adhesion can result both from an increase of fibrinogen level and alteration of RBCs surface properties (as is reported for diabetic patients, for example).

Theoretically, two models are evoked to describe the mechanism of adhesion between RBCs. The first one, which was prevailing for a long time, is the bridging model and has been adopted to account for fibrinogen and neutral dextran macromolecule-induced RBCs aggregation [Chien and Jan, 1973]. This model assumed that the proteins adsorb onto the RBC membrane and form a cross-link to the nearby RBC [Brooks, 1988]. The second model is the depletion one, stating that configurational entropy of the suspended molecules (e.g. fibrinogen) is lowered close to RBC surface, leading to a depletion layer, so that when the gap between two RBCs becomes of the order of depletion layer, the gap becomes less populated by fibrinogen molecules than elsewhere, and this results into osmotic attraction between RBCs.

1.3 A brief overview on literature about RBCs aggregation

Studies of RBCs aggregates are traced, at least, back to the beginning of 19th century. Indeed in 1827, RBCs aggregation was observed by Hodgkin and Lister [Hodgkin and Lister, 1827]. They reported that RBCs stack on each other forming a long cylindrical structure "rouleau", similar to piles of money. Each rouleau adheres to other rouleaux and a network is produced with intervals of colorless liquid sanguinis. Several decades later, Robin Fahraeus was among the first scientists who was interested in blood aggregation from a physical point of view [Fåhraeus, 1929, Fahraeus and Lindqvist, 1931, FÅHRAEUS, 1958]. He investigated the effect of aggregation on blood rheology and the suspension stability of the blood. Based on his observations of aggregate behavior in blood from both helathy and diseased subjects, he concluded that aggregates in pathological blood show more robust structure. As stated above plasma proteins (e.g. fibrinogen) are major actors in the aggregation process.

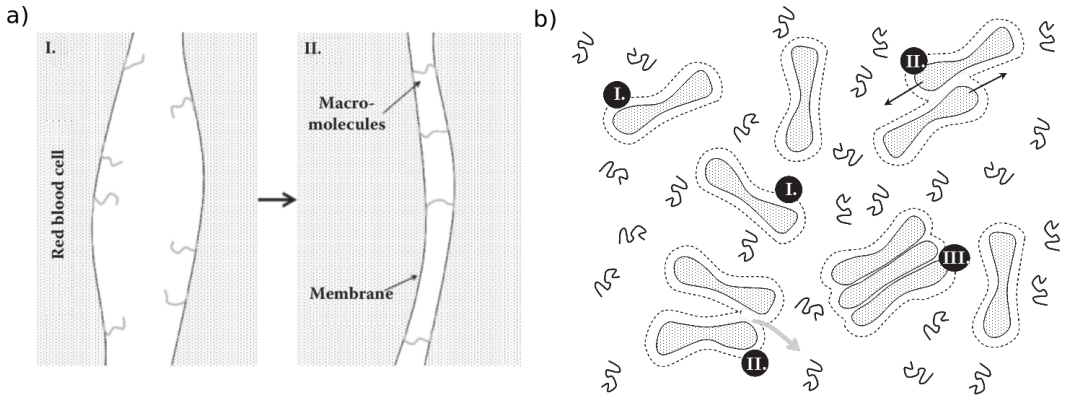

FIGURE 1.3 : a) Schematic illustration of how macromolecular bridging brings adjacent cells into intimate contact : I. Macromolecules are adsorbed onto adjacent RBC surfaces. II. Aggregation of RBC occurs due to macromolecular bridging [Baskurt et al., 2011]. b) Schematic picture of how macromolecular depletion interaction brings adjacent cells into intimate contact : (I) macromolecules are depleted from RBC surfaces ; (II) attraction develops when depletion layers overlap due to solvent displacement from the depletion zone into the bulk phase (grey arrow), and adjacent cells slide along each other to maximize the contact area and thus the loss in free energy (black arrows) ; (III) the resultant intimate cell–cell contact facilitates RBC aggregation [Baskurt et al., 2011].

The simplest and basic question about RBCs aggregation is how two interacting RBCs may adhere to each other forming a "doublet" due to plasma proteins. The erythrocyte doublet aggregation is the primary process in the formation of erythrocyte aggregates in blood flow. Bertoluzzo et al [Bertoluzzo et al., 1999] studied the erythrocytes aggregation, using light transmission through blood sample and observed that the aggregation starts by the formation of a collection of RBC doublets. The doublet formation is a first basic building block for aggregation that should be clarified. Many numerical simulations based on a minimal model of adhesion which takes into account an adhesion energy potential having a Lennard-Jones type, have been undertaken. They focused on the doublet morphology in a quiescent fluid [Ju et al., 2013, Hoore et al., 2018, Quaife et al., 2019, Flormann et al., 2017]. Depending on the adhesion energy between RBCs, the doublet adopts many configurations that have been validated experimentally [Flormann et al., 2017, Hoore et al., 2018]. A central question is : how the doublet responds to an applied flow ? does the doublet persist to dissociation in the case of high flow strength ? if not, then what are the main ingredients involved in the resistance of the doublet to dissociation ? These questions will be analyzed in this thesis.

Several experimental techniques allowed to have access to the adhesion energy between two RBCs. P. Steffen et al [Steffen et al., 2013] quantified the energy of adhesion induced by Dextran using atomic force microscopy-based single cell force spectroscopy. This has led to the determination of adhesion energy for different values of Dextran concentration. The same technique was adopted by M. Brust et al by measuring the adhesion energy as a function of fibrinogen concentration [Brust et al., 2014]. Bronkhorst et al [Bronkhorst et al., 1997] used optical tweezers techniques to probe RBCs aggregation process. Later, this technique was adopted to study and measure the adhesion between RBCs in various environment [Lee et al., 2016, Maklygin et al., 2012, Fontes et al., 2008]. Confrontation between experiments and simulations has found a remarkable agreement regarding doublet of RBCs at equilibrium [Flormann et al., 2017].

Blood rheology is an important determinant of blood flow characteristics. The blood viscosity depends on many factors such as hematocrite, RBCs deformability, shear rate and the interaction between RBCs. Fahraeus [Fahraeus and Lindqvist, 1931] showed that the blood rheology is highly affected by the RBCs aggregation. A high enough concentration of fibrinogen increases the RBCs aggregation, leading to enhanced viscosity [Chien et al., 1967, Brust et al., 2014]. It is also known that blood viscosity may be strongly affected in some cardiovascular diseases, such as sickle cells anemia and diabetes [Nader et al., 2019, Richards and Nwose, 2010].

Despite numerous studies since more than a century, several questions still remain open, and especially under flow. For example, does a doublet of RBCs always dissociate once formed is shear stress is large enough, or are there situations where a doublet becomes robust ? Once doublet dynamics is understood, what is dynamics for high hematocrits ? Is adhesion beneficial or hampering for blood perfusion ? Besides plasma proteins, what are the impact of structural properties (e.g. glycocalyx) on RBCs clusters. Numerical simulations (in 2D and 3D) will help us to answer the first three questions, and experimental studies will clarify the role of glycocalyx (4 th question) in the process of aggregation.

1.4 Contribution of the present thesis

This thesis contributes to the understanding of dynamics and rheology of RBC aggregates. We will adopt 2D vesicle and 3D capsule models to mimic RBC. In addition to simulations, we carried out microfluidic experiments presented in chapter 6. The main goal of this thesis is to investigate more deeply the RBC-RBC aggregate dynamics

and rheology, as well overall as transport properties (like global RBCs flux) in the presence of RBC aggregates. We will also pay a special experimental attention to the role of glycocalyx cleavage (to mimic diseases) in RBC aggregates stability. The main contributions of this thesis are discussed in the following subsections.

1.4.1 The dynamics and the rheology of a single 2D multilobe vesicle in a confined geometry.

Chapter 3, after chapter 2 presenting the methods and techniques, addresses a central question about the relevance, or not, of RBC cytoskeletton in the manifestation of some shapes (called multilobes). For that purpose, we addressed the question whether such shapes are manifested by a vesicle, and even in 2D. In Chapter 2, we analyze the dynamics and rheology of a single 2D vesicle in a confined geometry. The vesicle is subject to a shear flow and bounded by two planar rigid walls on each side. A phase diagram is determined in a wide range of viscosity contrast (the ratio between the inner and the outer fluid viscosities of the membrane) and shear rates. The multilobe shape are observed at high values of shear rates, and viscosity contrast. The cytoskeleton of a RBC is not necessary for the multilobe manifestation, in contrast with recent claims. We demonstrate that the multilobe shapes are due to membrane tension only. We investigate the rheology of the multilobe shapes in the dilute regime. We discuss the stability of the centered solutions and the emergence of the of the off-center ones.

This work has been published : Mehdi Abbasi, Alexander Farutin, Abdessamad Nait-Ouhra, Hamid Ez-Zahraouy, Abdelilah Benyoussef, and Chaouqi Misbah, Dynamics and rheology of a single two-dimensional multilobe vesicle in a confined geometry, Phys. Rev. Fluids, 7, 093603 (2022).

1.4.2 Erythrocyte-erythrocyte aggregation dynamics under shear flow

A main objective of this chapter (chapter 4) is to build a basic understanding of stability of RBCs aggregates. For this reason we have concentrated on a doublet of RBCs, which allowed us to identify some unsuspected facts, like regimes of strong stability of doublets, even for adhesion energies within physiological ranges.

In chapter 4 the dynamics and rheology of RBC doublet are investigated numerically using a boundary integral method in 2D and Lattice Boltzmann method in 3D. We sum up our results on the dynamics of doublet in a rich phase diagram in the parameter space (flow strength, adhesion energy) showing four different types of

doublet configurations and dynamics. We find that membrane tank-treading plays an important role in doublet disaggregation, in agreement with experiments on RBCs. A remarkable feature found here is that when a single cell performs tumbling (by increasing vesicle internal viscosity) the doublet formed due to adhesion (even very weak) remains stable even under a very strong rate. It is seen in this regime that an increase of shear rate induces an adaptation of the doublet conformation allowing the aggregate to resist cell-cell detachment. We show that the normalized effective viscosity of doublet suspension increases significantly with the adhesion energy, a fact which should affect blood perfusion in microcirculation. We also investigate the effect of adhesion energy on the ATP release from RBCs.

The work on 2D has been published : M. Abbasi, A. Farutin, H. Ez-zahraouy, A. Beenyoussef, C. Misbah, Erythrocyte-erythrocyte aggregation dynamics under shear flow ; Phys Rev. Fluids, 6, 023602 (2021). The article for 3D is under preparation.

1.4.3 Red blood cells aggregates transport for finite concentration

Once we have analyzed in details thee doublet aggregation, the basic building block, we are in a position to study flow of RBCs at finite concentration, in a pipe-like flow. In chapter 5, we analyze the aggregation properties of RBCs suspensions under Poiseuille flow. We investigate the effect of adhesion energy on the RBCs transport (RBCs flux), and the RBC suspension rheology. At high viscosity contrast the aggregation is irreversible whereas at low viscosity contrast the aggregation is reversible in the physiological range of adhesion. We show that the physiological adhesion is important for optimal transport of RBCs and the fluidity of blood. Indeed, we found a counter-intuitive fact : the RBCs flux is higher in the presence of moderate aggregates than in their absence. When the adhesion is too strong the flux is lower, meaning that there exists an optimal adhesion energy (depending on flow strength) for which flow of RBCs is optimal. Thus a moderate adhesion energy seems to be beneficial for a better perfusion. The gain in flow efficiency may attain up to 30 % .

An article is under preparation.

1.4.4 The effect of pancreatic amylase activity on erythrocyte aggregation stability.

The erythrocyte glycocalyx plays crucial role in the adhesion between RBCs and between RBCs and endothelial cells. It is known that the erythrocytes are charged

negatively at their surface due to the glycocalyx structure. In chapter 6 we perform experiments in order investigate how does the glycocalyx cleavage alter the RBCs aggregation. Here, the glycocalyx degradation is induced by the incubation of RBCs in α-amylase solution. This enzyme is known to show high activity for patients with pancreatitis and for cosmonauts during long space missions. After the incubation step we induce adhesion between RBCs using dextran 150 with a fixed concentration in this study. We have evaluated the glycocalyx layer using confocal microscopy, and have found that the glycocalyx is damaged when the RBCs are incubated in solution containing a high enough concentration of amylase, corresponding to a pathological situation. In the absence of flow, the number of RBCs per aggregates increases with the amylase concentration, and the aggregates show a rounded shape at high concentration of amylase, in contrast to the classical rouleaux shape. We have further shown that the degradation of erythrocyte glycocalyx confers more stability to aggregates, in that a higher hydrodynamic stress is required to break the aggregates.Under flow, the probability distribution of thee aggregates size increases significantly with amylase concentration.

An article is under preparation.

Chapitre 2

Model, numerical methods and experiment set-ups and materials

In this chapter we describe the numerical method used in this work, and specify the adhesion model adopted to study the RBCs aggregation. Both 2D and 3D simulations are used throughout this work. In the second part of this chapter we present the experimental set-up as well as experimental techniques and materials.

2.1 Red blood cells and other biomimetic particles

The dynamics and the morphology of RBCs under flow, and of their biomimetic counterparts (vesicles and capsules) have been the subject of intensive studies during the last two decades, theoretically [Keller and Skalak, 1982, Seifert, 1999, Misbah, 2006a, Kessler et al., 2009], experimentally [Fischer et al., 1978b, Abkarian et al., 2007, Kantsler et al., 2008, Tomaiuolo et al., 2009, Coupier et al., 2012, Dupire et al., 2012, Abkarian et al., 2008, Fischer and Korzeniewski, 2013a, Minetti et al., 2019] and numerically [Quéguiner and Barthès-Biesel, 1997, Pozrikidis, 2005, Kaoui et al., 2009a, Biben et al., 2011a, Zhao and Shaqfeh, 2011, Fedosov et al., 2014, Farutin and Misbah, 2012, Trozzo et al., 2015, Agarwal and Biros, 2020]. One of the principal questions is identify whether or not the behavior of RBC is common to a wide range of soft particles (like vesicles, capsules, RBCs), or if it is specific to the RBC only. The strategy followed in this thesis is to address the problem by performing two dimensional simulations in the first step. Due to computational cost, our two dimensional simulations offers the possibility to explore a wide range of the control parameter space. Subsequently, three dimensional simulations are carried out including the effect of other RBC components (such as cytoskeletton) to draw more practical conclusions.

Interestingly, as will be seen later, in many cases the 2D simulations capture the essential 3D features, providing a legitimate status to 2D simulations. Several experiments will be performed in this thesis, with a special emphasisis on RBCs aggregation. Microfluidic tools will be used in the experiments. We will especially explore later in this thesis novel aspects affecting RBCs aggregation, namely how glycocalyx (a brush of glycoproteins attached to cell membrane) cleavage can alter properties of aggregation.

2.1.1 Two-dimensional model : vesicles system

We consider a 2D model, namely phospholipid vesicles. The two-dimensional vesicle model has proven to capture several features known for RBCs. Shapes like parachute and slipper [Guckenberger et al., 2018,Kaoui et al., 2009a], dynamics, such as tumbling and tank-treading [Biben et al., 2011a, Kaoui et al., 2009b] are also manifested by both systems. Other phenomena such as lateral migration of RBCs [Nait-Ouhra et al., 2018b], and the shapes of RBCs within aggregates [Flormann et al., 2017,Brust et al., 2014, Clavería et al., 2016] have been shown to be captured by the 2D vesicle model.

The force applied by the membrane on the surrounding fluid is obtained by a functional derivative of the following energy, which is the sum two contributions : the bending energy (the Helfrich energy [Zhong-Can and Helfrich, 1989]) and the membrane incompressiblity contribution :

$$E = \frac{k_b}{2} \oint_m c^2 ds + \oint_m \zeta ds, \tag{2.1}$$

where s represents the curvilinear coordinate on the vesicle contour, c is the local curvature of the membrane, k_b is the membrane bending rigidity, and ζ is a local Lagrange multiplier associated with the constraint of local perimeter inextensibility. The functional derivative (providing the force) of the bending energy can be found in [Kaoui et al., 2008]. The total force has the following form :

$$\mathbf{f} = k_b[\frac{d^2c}{ds^2} + \frac{1}{2}c^3]\mathbf{n} - c\zeta\mathbf{n} + \frac{d\zeta}{ds}\mathbf{t}, \tag{2.2}$$

$\mathbf{n}$ and $\mathbf{t}$ are the normal and tangential unit vectors respectively. The force can be rewritten in a dimensionless form :

$$\bar{\mathbf{f}} = [\frac{d^2\bar{c}}{d\bar{s}^2} + \frac{1}{2}\bar{c}^3]\mathbf{n} - \bar{c}\bar{\zeta}\mathbf{n} + \frac{d\bar{\zeta}}{d\bar{s}}\mathbf{t}, \tag{2.3}$$

where dimensionless variables are defined as follows :

$$\bar{f} = \frac{R_0^3 f}{k_b}, \quad \bar{c} = cR_0, \quad \bar{s} = \frac{s}{R_0}. \tag{2.4}$$

Here $R_0 = (A/\pi)^{1/2}$ is the characteristic size of the vesicle. Due to some computational reasons, we do not use $\bar{\zeta}$ directly in the numerical scheme of the force. The local extension of the membrane is instead prevented by the penalization energy E_{tens} which is substituted to the second term on the right hand side of Eq. (2.1) :

$$E_{tens} = \frac{k_s}{2} \int_0^1 \left(\frac{ds}{d\alpha} - L \right)^2 d\alpha, \tag{2.5}$$

where k_s is the extension modulus of the membrane, L is the prescribed perimeter of the vesicle, and α is a parametrization of the 2D curve; This coordinate is used to parametrize the position of the membrane points as $\mathbf{r}_{mem}(\alpha)$. We choose the parametrization in such a way that the position $\mathbf{r}_{mem}(\alpha)$ spans the whole membrane as α increases continuously from 0 to 1. The parametrization is continued periodically for other value of alpha : $\mathbf{r}_{mem}(\alpha + 1) = \mathbf{r}_{mem}(\alpha)$.

The tension force energy (2.5) is

$$\mathbf{f}_{tens} = \frac{d\tilde{\zeta}}{ds}\mathbf{t} - c\tilde{\zeta}\mathbf{n}, \text{ where } \tilde{\zeta} = k_s(ds/d\alpha - L), \tag{2.6}$$

which coincides with the tension contribution in Eq. (2.2) with the Lagrange multiplier ζ replaced by the local tension $\tilde{\zeta}$. Furthermore, the tension $\tilde{\zeta}$ in Eq. (2.6) tends to the Lagrange multiplier ζ as k_s is increased to infinity.

Equation (2.6) provides an explicit link between the stretching of the membrane and the local tension. The cost of this simplification is that the local arc length is never exactly equal to the prescribed value L. However, this difference is negligible for large enough k_s. We set $k_s R_0^3/k_b = 4 \cdot 10^3$ in our simulations which results in a good conservation of local arc length for all parameters explored in this study.

We define the reduced area which combines the vesicle perimeter L and its enclosed area A_0 as follow :

$$\tau_{2D} = \frac{(A/\pi)}{(L/2\pi)^2}. \tag{2.7}$$

2.1.2 Adhesion model

Each RBC interacts with other RBCs via hydrodynamic interaction but also via plasma proteins (like fibrinogen) which has tendency to making RBCs adhering (adhesion) to each other. Generally, at long range the cells attract each other due to the presence of protein (it is often assumed that this due to depletion force, leading to osmosis), while at short range the cells repel each other due to the glycoprotein

layer called glycocalyx. The adhesion energy in our model is represented using the Lennard-Jones potential as follow :

$$E_{i,j}^{adh} = \varepsilon \oint_{m_i} ds(\mathbf{X}_i) \oint_{m_j} ds(\mathbf{X}_j)\phi(|\mathbf{X}_i - \mathbf{X}_j|) \tag{2.8}$$

$E_{i,j}^{adh}$ is the energy of adhesion between i-th and j-th vesicle. The variable s represents the curvilinear coordinate on the vesicle contour, c is the local curvature of the membrane, k is the membrane bending rigidity, ζ is a local Lagrange multiplier associated with the constraint of local perimeter inextensibility, $\phi = -2\left(\frac{h}{r_{ij}}\right)^6 + \left(\frac{h}{r_{ij}}\right)^{12}$ is Lennard-Jones potential which describes attractive interaction at long ranges and repulsive interaction at short ranges. Here $\mathbf{r}_{ij} = \mathbf{X}_i - \mathbf{X}_j$, where $\mathbf{X}_i$ and $\mathbf{X}_j$ are two position vectors of two material points on two different vesicles i and j. h is the equilibrium distance between two points of the i-th and j-th vesicle and ε is the minimum energy associated to this distance. The functional derivative of the adhesion energy has the following form :

$$\mathbf{f}(\mathbf{X}_i)^{adh} = -\varepsilon \sum_{j \neq i} \int_{m_j} \left[\frac{d\phi(r_{ij})}{dr_{ij}} \left(\frac{\mathbf{r}_{ij}}{r_{ij}} . \mathbf{n}(\mathbf{X}_i) \right) + c(\mathbf{X}_i)\phi(r_{ij}) \right] \mathbf{n}(\mathbf{X}_i) ds(\mathbf{X}_j). \tag{2.9}$$

$\mathbf{n}$ and $\mathbf{t}$ are the normal and tangential unit vector respectively.

2.1.3 Three-dimensional model : capsules system

2.1.3.1 Membrane model

We deem here the RBC as a two-dimensional hyper-elastic thin shell enclosing an inner fluid of viscosity η_1 and suspended in an outer fluid of viscosity η_o. The membrane is embedded with resistances to volume variation, area dilatation, bending and shear deformations. The membrane is discretized into a triangular mesh, the forces are evaluated on each membrane nodes. We use 3380 triangles and 1692 nodes to discretize each RBC. The force applied by the membrane on the surrounding fluid is obtained by a derivative of the membrane energy, which has the following form :

$$E = \sum_{i=1} (E_i^b + E_i^{sb} + E_i^v), \tag{2.10}$$

The membrane bending energy [Helfrich, 1973] reads as :

$$E_i^b = \frac{k_b}{2} \oint_A H^2 dA, \tag{2.11}$$

where k_b is the membrane bending rigidity, H is the mean curvature and A is the membrane area. The shear elastic energy of the membrane obeys to the Skalak constitutive law, which is written as :

$$E_i^{sk} = \int_A \frac{k_s}{4}[I_1^2 + 2(I_1 - I_2) + k_\alpha I_2^2]dA \tag{2.12}$$

where k_s is the shear elastic modulus, k_α is the area dilatation modulus, I_1 and I_2 are the in-plane strain invariants ; see [Krüger et al., 2011] for more deetails. The RBC volume conservation corresponding to membrane impermeability condition is carried out using a volume penalty function which reads as :

$$E_i^v = \frac{k_v}{2}\frac{(V - V_0)^2}{V_0} \tag{2.13}$$

where V is the RBC volume, V_0 is the reference volume corresponding to the stress-free shape and k_v is the volume modulus expressed in unit of energy per volume. The membrane force is calculated on each membrane node $\mathbf{R^m}$ using the principle of virtual work, such that :

$$\mathbf{W} = -\frac{\partial(E_i^{sb} + E_i^v)}{\partial \mathbf{R^m}} \tag{2.14}$$

and the functional derivative of the bending energy reads [Zhong-Can and Helfrich, 1989] (for an alternative derivation see [Laadhari et al., 2010]) :

$$\mathbf{f^b} = k_b[2H(2H^2 - 2K) + 2\Delta_s H]\mathbf{n} \tag{2.15}$$

where K is the Gaussian curvatures, Δ_s is the Laplace-Beltrami operator and $\mathbf{n}$ is the normal vector pointing outward. The total membrane force is then written as :

$$\mathbf{f_T} = \mathbf{f^b} + \mathbf{W}, \tag{2.16}$$

We define The reduced volume that controls the RBC shape as follow :

$$\tau_{3D} = \frac{6\sqrt{\pi}V}{S^{3/2}} \tag{2.17}$$

S and V are the cell surface area and volume respectively. The maximum value $\tau_r = 1$ corresponds to a sphere. In the next section we will present two numerical methods used in this thesis.

2.2 Methods for solving hydrodynamic equations

In the present section methods used to solve the hydro-dynamical equations are presented. Spectral boundary integrals method (SBIM) and Lattice Boltzmann method (LBM) are used throughout this thesis, each method presents advantages and disadvantages for a given situation. Advantages and disadvantages will be discussed in the last part of this section.

2.2.1 Spectral boundary integral method : SBIM

2.2.1.1 Fluid flow

The RBCs typical linear size is about $3\mu m$, and under physiological conditions the typical shear rate value at the vessel wall, which depends on vessel diameter, ranges from $10^2 s^{-1}$ to $10^4 s^{-1}$ [Vennemann et al., 2007]. The blood plasma viscosity is about $\eta_0 = 10^{-3} mPa.s$. The Reynolds number, by taking the RBC size as a length scale, is quite small (in the range 10^{-4} to 10^{-2}), so that it is legitimate to take the zero Reynolds number limit. In this case the velocity of the inner (i.e. inside the vesicle) and the outer fluids is described by the Stokes equations :

$$-\nabla P + \eta_i \Delta \mathbf{v} = 0, \tag{2.18}$$

$$\nabla . \mathbf{v} = 0, \tag{2.19}$$

where $i = 0$ inside the vesicle and $i = 1$ outside the vesicle, P is the pressure and $\mathbf{v}$ is the velocity field. The Stokes equations (2.18) and (2.19) are supplemented by the following boundary conditions :

- The no-slip boundary conditions at the walls,
- The periodic boundary conditions for the velocity $\mathbf{v}$ and the pressure P,
- The continuity of the fluid velocity at the membrane,
- The force balance at the membrane, which dictates that the sum of the viscous forces applied by the inner and outer fluids on the membrane is balanced by the membrane force $\mathbf{f}$, the expression for which is given below.

These boundary conditions define a unique solution of the equations (2.18) and (2.19), which depends on the membrane conformation and forces $\mathbf{f}$.

2.2.1.2 Flow solver

Due to the linearity of Stokes equations we can transform the set of fluid equations into an integral equation. This is based on the use of Green's function techniques [Pozrikidis, 1992], and is a quite accurate method for interface problems. More precisely, the velocity at any point $\mathbf{r}$ in the simulation domain satisfies the following equation

$$\Lambda(\mathbf{r})\mathbf{v}(\mathbf{r}) = \mathbf{v}^{\infty}(\mathbf{r}) + \mathbf{v}^{ves}(\mathbf{r}) + \mathbf{v}^{wall}(\mathbf{r}), \tag{2.20}$$

where $\mathbf{v}^{\infty}(\mathbf{r})$ is the imposed velocity field, $\mathbf{v}^{ves}$ is the velocity field produced by the vesicles, and $\mathbf{v}^{wall}$ is the velocity field produced by the wall. The coefficient Λ is defined as

$$\Lambda(\mathbf{r}) = \begin{cases} \lambda & \text{if } \mathbf{r} \text{ is inside a vesicle.} \\ (1+\lambda)/2 & \text{if } \mathbf{r} \text{ is on a vesicle membrane.} \\ 1 & \text{if } \mathbf{r} \text{ is outside all vesicles or is on a wall.} \end{cases} \tag{2.21}$$

Here λ is the viscosity contrast defined as $\lambda = \dfrac{\eta_1}{\eta_0}$. The vesicle contribution is defined as

$$\mathbf{v}^{ves}(\mathbf{r}) = \frac{1}{\eta_0} \oint_m \underline{\underline{G}}(\mathbf{r}_0, \mathbf{r}) \cdot \mathbf{f}(\mathbf{r}_0) ds(\mathbf{r}_0) + (1-\lambda) \oint_m \mathbf{v}(\mathbf{r}_0) \cdot \underline{\underline{\underline{T}}}(\mathbf{r}_0, \mathbf{r}) \cdot \mathbf{n}(\mathbf{r}_0) ds(\mathbf{r}_0), \tag{2.22}$$

where $\underline{\underline{G}}(\mathbf{r}_0, \mathbf{r})$ and $\underline{\underline{\underline{T}}}$ are the Green's functions (G_{ij} refers to the so-called single-layer contribution, while T_{ijk} accounts for the double-layer contribution). The full description of integral equations and green's function is exposed in appendix A.

2.2.1.3 General outline of the numerical procedure

In order to preserve high accuracy we use Fourier basis for discretization of all functions on the membrane contour and compute all derivatives in Fourier domain [Veerapaneni et al., 2009, Dalal et al., 2020]. The shape of the vesicle at time t is described by a periodic function $\mathbf{r}_{mem}(\alpha, t)$ of the reference coordinate α, as defined above. We parametrize this function by a Fourier series

$$r_{mem,x}(\alpha) + i r_{mem,y}(\alpha) = \sum_{k=-k_{max}}^{k_{max}} r_k e^{2\pi i k \alpha}, \tag{2.23}$$

where the complex amplitudes r_k are the shape parameters of the membrane and k_{max} defines the number of Fourier harmonics used to represent the membrane shape (typically, we use $k_{max} = 31$, which gives 63 harmonics in total).

One time step of the simulation takes a set of values of r_k and proceeds as follows :

1. We use r_k to reconstruct the shape of the membrane $\mathbf{r}_{mem}(\alpha, t)$, and the derivatives $\partial_\alpha \mathbf{r}_{mem}(\alpha, t)$, $\partial_{\alpha\alpha} \mathbf{r}_{mem}(\alpha, t)$.

2. We use $\mathbf{r}_{mem}(\alpha, t)$, $\partial_\alpha \mathbf{r}_{mem}(\alpha, t)$, and $\partial_{\alpha\alpha} \mathbf{r}_{mem}(\alpha, t)$ to compute the membrane force, membrane normal, arc length element of the membrane, perimeter, enclosed area, and so on.

3. We use the above force, shape, normal and arc element to compute the flow in the channel.

4. We expand the velocity field at the membrane into a Fourier series and update the Fourier components r_k.

The implementation details for the steps 2 and 3 are given below. The step 4 is done using a simple explicit Euler scheme. This step also involves a procedure to conserve exactly the area enclosed by the membrane contour. Physically, this area is conserved by the incompressibility of the enclosed fluid and the impermeability of the membrane but this exact conservation is lost after numerical discretization. We thus use homogeneous deflation or inflation along the normal direction to conserve the area inside the vesicle at each time step.

2.2.1.4 Force calculation

We compute the force directly in the Fourier space by taking the variation of the membrane energies (2.1) and (2.5) with respect to the amplitudes r_k. The energy itself is calculated in the coordinate space, by discretizing the membrane contour by a large number of points homogeneously distributed in the α space $\alpha_i = i/N_{mem}$, $i \in \{0, 1, ..., N_{mem} - 1\}$. Here N_{mem} is the number of points used to discretize the membrane, we take $N_{mem} \geq 2(k_{max} + 1)$.

The derivatives with respect to the arc length are calculated as $\partial_s = \partial_\alpha/(ds/d\alpha)$. The integration with respect to the arc length element is reduced to the integration with respect to α by the substitution $ds = d\alpha(ds/d\alpha)$. Here $ds/d\alpha = |d\mathbf{r}_{mem}/d\alpha|$. The integration with respect to α is performed using the trapezoid rule (here the sum over all α_i divided by N_{mem}). This method shows super-algebraic convergence with N_{mem} for smooth periodic functions. The Fourier components of the membrane force are calculated from the virtual work principle, using the variation $E \to E + \delta E$ of the energy upon a small variation of the membrane shape $\mathbf{r}_{mem}(\alpha) \to \mathbf{r}_{mem}(\alpha) + \delta\mathbf{r}_{mem}(\alpha)$:

$$\delta E = -\oint \mathbf{f} \cdot \delta\mathbf{r}_{mem} ds = -\sum_{k=-k_{max}}^{k_{max}} \Re(F_k^* \delta r_k), \tag{2.24}$$

where F_k and δr_k are the coefficients of the Fourier series for $(f_x(\alpha) + if_y(\alpha))ds/d\alpha$ and $\delta r_{mem,x}(\alpha) + i\delta r_{mem,y}(\alpha)$, respectively. We thus define the force amplitudes from Eq. (2.24) as

$$\Re F_k = -\frac{\partial E}{\partial \Re r_k}, \quad \Im F_k = -\frac{\partial E}{\partial \Im r_k}. \tag{2.25}$$

Calculating the amplitudes F_k allows us to reconstruct the forces $\mathbf{f}ds/d\alpha$ which are used to calculate the fluid velocity as explained below.

In appendix B membrane discretization quality and comparison with other methods are discussed.

2.2.2 Lattice Boltzmann method : LBM

The Navier-Stokes equations are solved in the limit of small Knudsen and Mach numbers using the lattice Boltzmann method (LBM) which is based on the discretisation of the Boltzmann-BGK [Succi, 2001, Aidun and Clausen, 2010, Bhatnagar et al., 1954, Krüger et al., 2017] equation in time and space. In LBM, the fluid is seen as cluster of pseudo-fluid particles. The main quantity in LBM is the distribution function $f_i(\mathbf{x}, t)$, which gives the probability of finding a particle at position x and time t having a microscopic velocity $\mathbf{c}_i = (c_{ix}, c_{iy}, c_{iz})$, where $i = 1, ..., Q$, on a regular D-dimensional lattice in discrete time steps Δt. We consider here a $D3Q19$ model corresponding to a three dimensional lattice with $Q = 19$ velocities. The lattice Boltzmann equation has the following form :

$$f_i(\mathbf{x} + \mathbf{c}_i\Delta t) - f_i(\mathbf{x}, t) = \Omega_i(\mathbf{x}, t) + F_i(\mathbf{x}, t)\Delta t, \tag{2.26}$$

Where $F_i(\mathbf{x}, t)$ is a bulk force term to be specified below and $\Omega_i(\mathbf{x}, t)$ is the collision operator which is written as follows :

$$\Omega_i(\mathbf{x}, t) = -\frac{\Delta t}{\tau}[f_i(\mathbf{x}, t) - f_i^{eq}(\mathbf{x}, t)], \tag{2.27}$$

$f_i^{eq}(\mathbf{x}, t)$ is the equilibrium distribution, is obtained from an approximation of the Maxwell distribution and can be expressed as :

$$f_i^{eq}(\mathbf{x}, t) = \omega_i\rho[1 + \frac{(\mathbf{c_i} \cdot \mathbf{u})}{c_s^2} + \frac{1}{2}\frac{(\mathbf{c_i} \cdot \mathbf{u})^2}{c_s^4} - \frac{1}{2}\frac{|\mathbf{u}|^2}{c_s^2}], \tag{2.28}$$

where τ is a dimensionless relation time, related to the kinematic viscosity of the fluid $\nu = \rho_0 c_s^2(\tau - \Delta t/2)$ (ρ_0 is the main fluid density). Here $c_s = (1/\sqrt{3})(\Delta x/\delta t)$ called the lattice speed of sound, ω_i are lattice weights, Δx is the lattice constant, ρ the fluid density, $\mathbf{u}$ is the velocity fields as a truncated expansion of the Maxwell–Boltzmann

distribution (valid at small Mach number, $Ma = |\mathbf{u}|/c_s \ll 0.1$). For a $D3Q19$ LBM model, the lattice weights are 1/3, 1/18 and 1/36 for $i = 1$, $i = 2, ..., 7$ and $i = 8, ..., 19$ respectively. The local macroscopic density ρ and velocity $\mathbf{u}$ can be computed as :

$$\rho = \sum_{i=1}^{19} f_i(\mathbf{x}, t), \tag{2.29}$$

$$\mathbf{u} = \sum_{i=1}^{19} f_i(\mathbf{x}, t)\mathbf{c_i}/\rho, \tag{2.30}$$

The time step, the lattice constant, the the relaxation time and the mean fluid density are fixed at unity. More explanations about the used method and immersed boundary method can be found in [Aouane et al., 2021].

The coupling between the fluid flow and the membrane dynamics is performed using the immersed boundary method (IBM), which is developed originally by Peskin to analyze blood flow in the heart [Peskin, 1977]. In the IBM, the moving Lagrangian membranes nodes coupled with the fixed Eulerian fluids nodes [Peskin, 2002], where the flow velocity is calculated using the LBM. Once the The force density acting by the cell membrane nodes on the surrounding Eulerian fluid nodes $\mathbf{x}$ is calculated by the following spreading equation :

$$\mathbf{F}(\mathbf{x}, \mathbf{t}) = \int_A \mathbf{f_T}\delta(\mathbf{x} - \mathbf{X}_m)dA \tag{2.31}$$

Where δ is a three dimensional approximation of the Dirac delta function.

2.2.3 Comparison between SBIM and LBM

In this thesis, we deal with several problems such as : the dynamics and the rheology of a single vesicle, the adhesion between two red blood cells (vesicles in 2D and capsule in 3D), flow of RBCs suspension in straight channel and RBCs flow in complex geometry. However, each problem present different complexity in order to solve it. Two numerical methods are used in this thesis : Spectral integral boundary method and Lattice Boltzmann method. Here, we expose some advantages and disadvantages of the two methods.

- Advantages of spectral integral boundary method
  - Tracking high deformations of the vesicle membrane
  - Easy implementation of the vesicle membrane force

  - No need to solve the problem in the fluid bulk, direct computational of the vesicle membrane velocity.

- disadvantages of spectral integral boundary method
  - Evaluating integral equations with integrals exhibiting singularities (logarithmics for G and 1/r for T).
  - Time consuming for high suspension concentration.
  - Limited geometrical configurations for which the Green's functions exist.

- Advantages of Lattice Boltzmann method
  - Parallel computing.
  - Simple coding.
  - Easy to implement complex geometries.

- disadvantages of Lattice Boltzmann method
  - The accuracy is limited to 2nd order.
  - To reduce the inertia effect, a small Reynolds number must be used.
  - The use of immersed boundary method further reduce the accuracy, such that the accuracy at the boundary might be just 1st order.
  - The single-relaxation-time scheme is used, which leads to error at large viscosity contrast

2.2.4 Dimensional numbers

Dimensionless numbers are used to describe the vesicle and the flow characteristics :

- The capillary number : allows to quantify the flow strength over bending rigidity of the membrane
$$C_a = \frac{\eta_0 < \dot{\gamma} > R_0^3}{k} \equiv \dot{\gamma}\tau_c \tag{2.32}$$
$< \dot{\gamma} >$ is the applied shear rate and k is the bending rigidity modulus.

- The capillary number related to the membrane shear elasticity :
$$C_s = \tau_s \dot{\gamma} = \frac{\eta_0 R_0 \dot{\gamma}}{k_s} \tag{2.33}$$

- The viscosity contrast : the ratio between the viscosities of the internal and external fluids

$$\lambda = \frac{\eta_1}{\eta_0} \tag{2.34}$$

- The reduced area : combining the vesicle perimeter L and its enclosed area A

$$C_n = \frac{2R_0}{L_y} \tag{2.35}$$

where L_y is the channel width.

2.3 Detail of microfluidic experiments

2.3.1 Red blood cell samples

2.3.1.1 Blood preparation

In all the microfluidic experiments we manipulated fresh blood collected from the local blood bank (Etablissement Français du Sang, Grenoble, France). Blood is sampled from healthy donors, tested and transported in citrate tube of volume $3mL$ inside appropriate box. All the preparation of samples are made in L2 (L2 means a certain level of security for manipulation of human cells) room, wearing gloves and blouse. The bench and equipment are disinfected immediately after work.

In order to get a fresh RBCs, we firstly centrifuge (Mini-centrifugeuse, Fisher scientific, France) a small volume of blood (generally $1mL$) at $6000rpm$ for 3 minutes at room temperature to remove all substances except RBCs. The liquid phase and buffy coat is removed by aspiration (see Fig 2.1). Subsequently, the sedimented RBCs is suspended in $1ml$ of physiological buffer solution (PBS, phosphate buffered saline, Sigma-Aldrich, Germany) and the centrifugation and washing steps are repeated three times.

When working with RBCs, care must be taken with the acidity of the solution used. RBCs proprieties are very sensitive to the osmolality. Three kinds of osmalilaty situations can be categorized : i) Hypotonic : in this situation, the solute is presented with very low concentration ; in this case, almost RBCs are spherocytes. ii) isotonic : is the normal situation, the RBCs are in their normal shape (biconcave) as in plasma. iii) Hypertonic : for solutions with a very high concentration of solute, the characteristic shape in this case is echynocyte. In order to work in isotonic we choose to work PBS as basic solution.

The collected blood is stored in the fridge for three days. After that, the RBCs start showing echynocyte shape, and their deformation is affected.

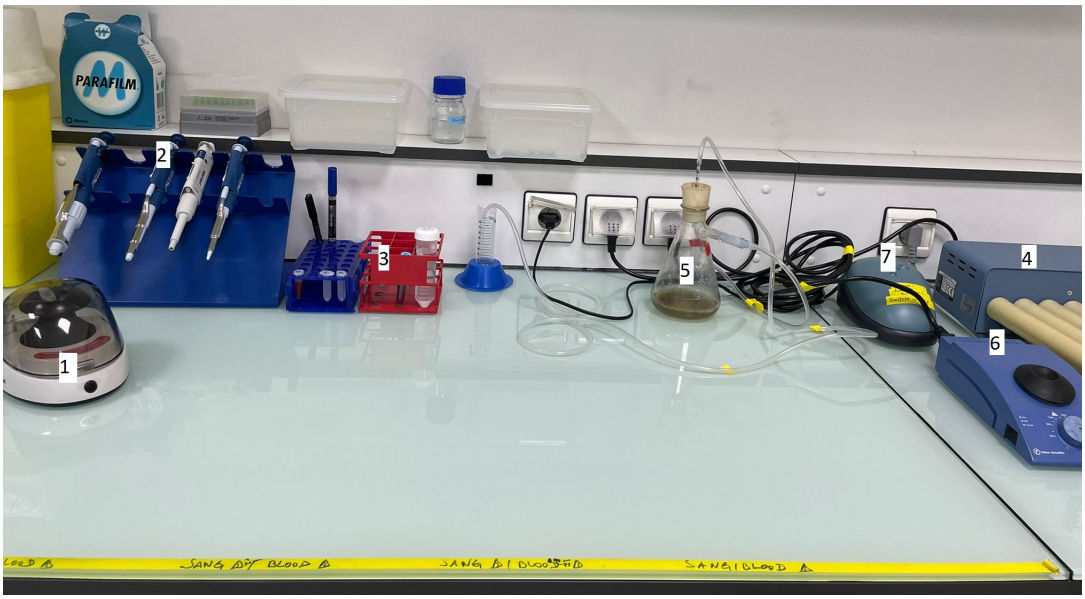

FIGURE 2.1 : Setup for place of sample preparation. 1 : Centrifuge. 2 : Micropipette. 3 : Tubes rack. 4 : Tube roller . 5 Round-bottom flask for liquid waste. 6 : Vortex device. 7 : Vacuum pump.

2.3.1.2 Degradation of red blood cells glycocalyx

The RBCs were then suspended in a solution of PBS + α-amylase from porcine pancreas type VI-B (Sigma-Aldrich, Germany) and incubated three hours on a tube roller uniRoller 6 (Lab Unlimited, Dublin, Ireland). The tubes roller were used to avoid RBCs sedimentation during incubation. In order to mimic the physiophatological conditions, four concentrations of α-amylase were chosen. After incubation, the RBCs were centrifuged and washed three times to remove definitely the α-amylase enzyme from the suspension. Remaining of α-amylase enzyme in the suspension may digest the macro-molecules of dextran 150 (Sigma Aldrich, Taufkirchen, Germany) and then the aggregation process may be affected.

The washed RBCs were suspended in a solution of PBS that contains 15mg/mL of dextran 150 and 1 g/L bovine serum albumin (BSA, Sigma-Aldrich ; Taufkirchen, Germany), the hematocrite was fixed at 5%.

2.3.2 Microfluidic chips preparation

The preparation of the PDMS (Polydimethylsiloxane) microchip consists first of preparing the mold. Firstly, a silicon wafer (substrate) is cleaned in the plasma oxygen 5 minutes and placed on a hot plate at 130°C for dehydration. Secondly, an epoxy negative photosensitive resin (SU8 from Gersteltec) is spin coated at specific speed

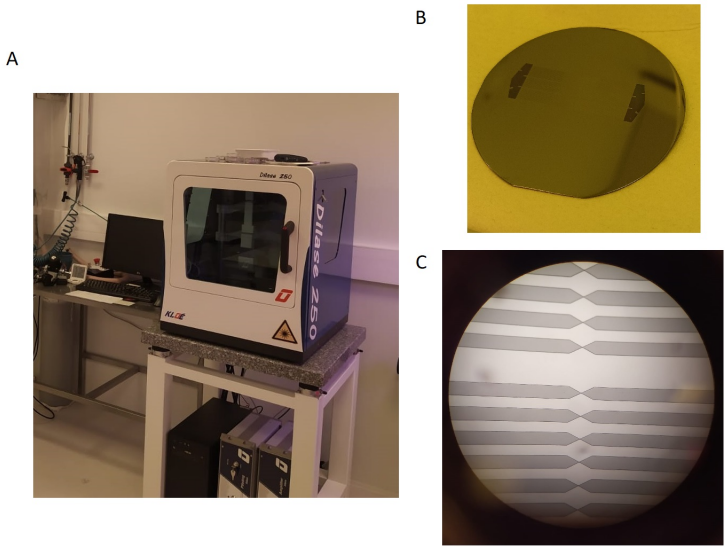

FIGURE 2.2 : A : Photography of the lithography machine. B : Circuit printed on the silicon wafer. C : The silicon wafer under microscope.

depending on the desired thickness. After that, the pre-baking step is necessary to remove the solvent from the resin, the wafer is placed on a programmable hot plate. The design of the microchannel circuit is drawn with inkscape software and saved as DXF file. Subsequently, the wafer is placed inside laser lithography machine Dilase 250 (KLOE, France) (Fig. 2.2. A)

The drawn design is transferred to the Dilase software and is written on the wafer using the laser. The laser intensity, writing speed and beam size are specified depending on the circuit design. In order to accelerate the cross-linking of the exposed area the wafer is placed on the programmable hot plate, this step makes the exposed area of the resin insoluble in the developer. The non-crosslinked resin is remove using PGMEA (Propylene glycol methyl ether acetate) bath, rinsed with isopropanol and dried with nitrogen. The last step is the hard baking of 2 hours at 135°C in the oven to avoid cracking of the resin. Before the hard bake the silicon wafer (Fig. 2.2. C) is observed under microscope to check the design as shown in (Fig. 2.2. B). The entire process is summarized in the Fig. 2.3.

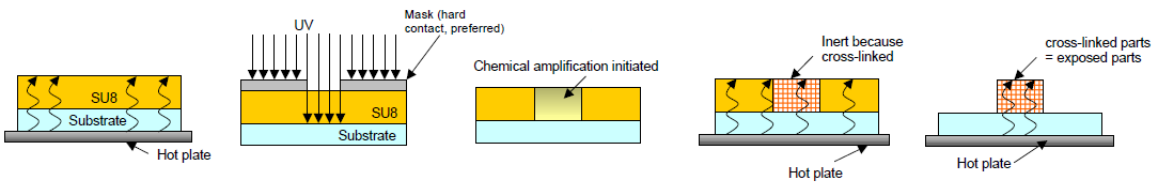

FIGURE 2.3 : Schmeatics of the process (from technical datasheet of Gersteltec Sarl).

The prepared wafer is used as a positive mold for the circuit preparation. In a plastic beaker, the PDMS (Sylgard 184) and its curing agent (ratio 1/10) are mixed and placed in a vacuum chamber to eliminate bubbles. When the bubbles are definitely removed the PDMS is poured onto the wafer. The PDMS is then placed in oven for two hours. The size of the channel is measured by cutting a slice of the PDMS and observing it under the inverted microscope. The hardened PDMS chip can be cut out with a scalpel. Inlet and outlet wells are punched at a size of 2mm. The PDMS chip and glass cover slip are placed in a plasma oxygen chamber before being bonded. Oxygen plasma had a hydrophilic effects on surfaces. All this procedure is done in a clean room. This avoids dust contamination. The equipment used are shown in Fig. 2.4.

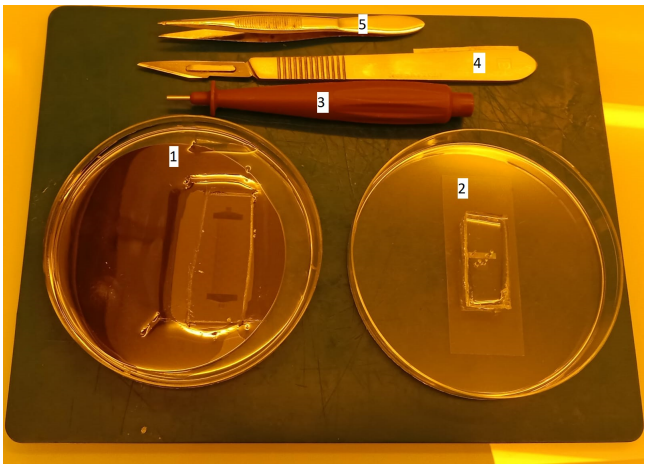

FIGURE 2.4 : 1 : Microfluidic chip. 2 : Wafer in petri dish containing the PDMS and curing agent mixture. 3 : PDMS Puncher. 4 : Scalpel . 5 Tweezers.

2.3.3 Sample observation and image processing

2.3.3.1 Inverted microscope

The microfluidic chip was placed on an inverted microscope (Olympus IX71, France) equipped with a digital fast camera (FASTCAM Mini UX, Photron, Tokyo, Japan) and a blue LED illumination (wave length is $455nm$). The microfluidic device starts and ends at an inlet reservoir of approximately $2mm$ of diameter. The inlet and outlet are connected with flexible medical-grade polyethylene tubing of inner diameter $0.86mm$ to the sample and waste containers respectively. The RBCs samples are pumped through the microfluidic channels using a high-precision pressure controller device (OB1-MK3, Elveflow ; Paris, France), the operating pressure range is $0 \leq p \leq 2000$.

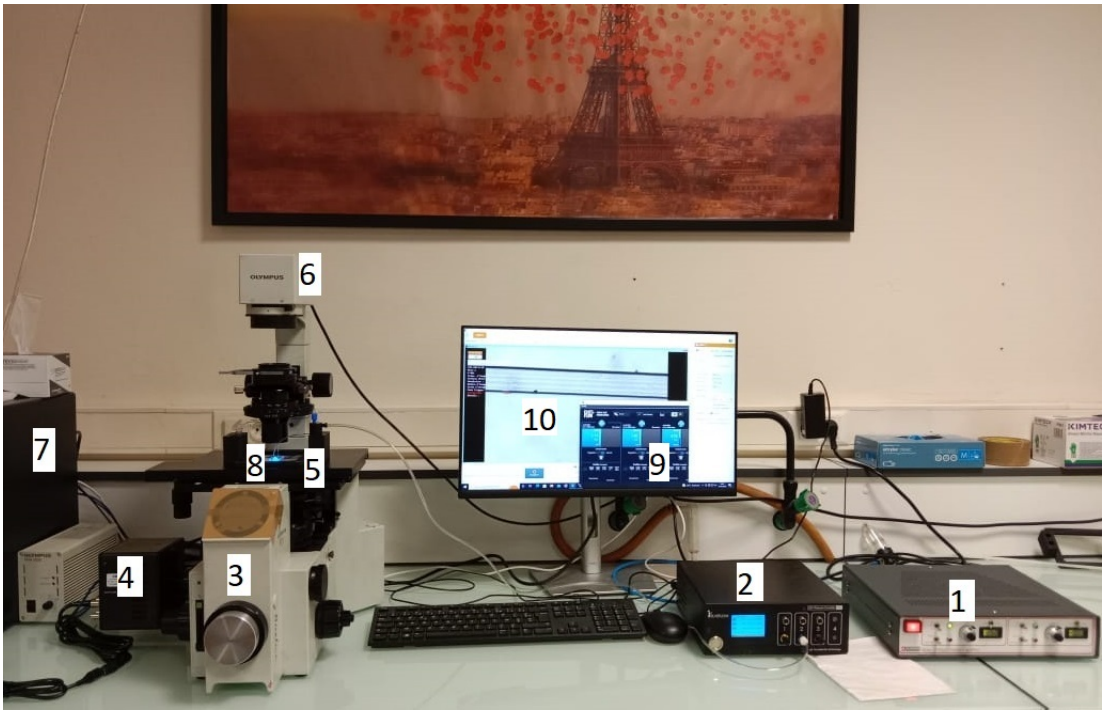

FIGURE 2.5 : Setup for microfluidic experiments I built during my thesis. 1 : Power Supply and Controllers of the blue LED (light-emitting diode). 2 : Pressure controller. 3 : Inverted microscope. 4 : High speed camera. 5 X-Y piezostage and sample holder. 6 : Blue LED. 7 : Computer. 8 : Microfluidic chip. 9 : Software interface of pressure controller. 10 : Software interface of high speed camera.

Images were acquired with a high frame rate of 2000fps and high magnification (60× objective) at a fixed position at the middle of the microfluidic chip. The microfluidic setup that I built during my thesis is shown in Fig. 2.5.

The maximal velocity in the channel was calculated by following individual RBCs by tracking the cell position over the image sequence within the field of view. A home-made image processing script (Python, scikit-image) allowed to determine area, perimeter and mass center position of RBCs aggregates and the number of RBCs per aggregates.

2.3.3.2 Confocal microscopy

In order to perform Confocal fluorescence microscopy, the RBCs were suspended in PBS + Wheat Germ Agglutinin (WGA) conjugated with a fluorophore (Alexa 488). WGA is a plant lectin that known to bind carbohydrate moieties of the glycocalyx from RBCs [Salzer et al., 2002]. For the staining the glycocalyx on the RBCs the usd WGA concentration was fixed at $5\mu g/ml$. Confocal fluorescence microscopy was performed on an inverted microscope (Ziess, France). Images of RBCs were obtained in raster mode using a Zeiss LSM710 module and a $40\times/NA1.3$ oil-immersion objective.

2.4 Summary

This chapter presents the model used to represent numerically RBCs in two and three dimensional. Two numerical methods are exposed in chapter 2.2 : Spectral integral boundary method and Lattice Boltzmann method. The last section is dedicated to the different equipments used in the setup I built in the experimental room for microfluidic experiments. The preparation method of microfluidic device and samples are also exposed in this chapter.

Chapitre 3

The dynamics and the rheology of a single 2D multilobe vesicle in a confined geometry.

In this chapter, we will show our 2D simulations results of a single vesicle in confined shear flow in order to study the dynamics and the rheology of a single vesicle. Two previous studies [Lanotte et al., 2016, Mauer et al., 2018] have shown that the RBC under flow may show a deformed multilobe shape, which was attributed to RBC cytoskeleton. In contrast to this claim our study revealed that cytoskeleton is not essential, since the multilobes are found in a vesicle system and even in 2D. We will present in this chapter a rich phase diagram for the occurrence of multi-lobe shapes. In addition, we will analyze the rheology as well as lateral migration and its correlation with to normal stress difference.

3.1 Introduction

During last decades a growing interest in studying the dynamics and morphology of RBCs under flow has been witnessed, due to the direct biological application and pertinence physical mechanisms which govern the observed RBC shapes and dynamics. In blood circulation, RBCs have the ability to assume several morphologies. The most known shapes are, i) Parachute, which is a symmetric shape [Skalak and Branemark, 1969, Chen and Liu, 2012], ii) asymmetric shape, called Slipper [Tomaiuolo et al., 2009, Chen and Liu, 2012, Kihm et al., 2018, Kaoui et al., 2009a], to cite a few examples. More recent studies reported on the existence of other shapes (Snaking, Pin, Peanut) [Aouane et al., 2014]. Under shear flow, a single RBC exhibits three main dynamics, i) tank-treading motion (TT) where the cell adopts a fixed orientation and

its membrane rotates like a tank tread [Schmid-Schönbein and Wells, 1969, Goldsmith et al., 1972, Tran-Son-Tay et al., 1984], ii) tumbling (TB) motion where the cell flips like a solid particle [Goldsmith et al., 1972, Dupire et al., 2012] and iii) vacillating breathing (also called swinging) [Misbah, 2006a, Noguchi and Gompper, 2007], where the cell orients along some direction and its long axis undergoes oscillations.

In the community of physicists, one of the main question that arises is to recognize whether or not a given morphology or dynamics is common to a wide range of soft particles (like vesicles, capsules, RBCs), or if it is specific to a given type of particle. Most of the aforementioned dynamics, both under shear and Poiseuille flows, are common to RBCs, vesicles and capsules [Deschamps et al., 2009, Shi et al., 2013, Kaoui et al., 2012, Quint et al., 2017, Guckenberger et al., 2018, Dupire et al., 2012, Abkarian et al., 2007, Biben et al., 2011b, Farutin et al., 2014, Cordasco et al., 2014]. From mechanical point of view, vesicles differ from RBCs by the absence of shear elasticity due to cytoskeleton. Despite this simplification, vesicles have often revealed to have many shapes and dynamics in common with RBCs. The comparison between vesicles and RBCs can help identifying features which are specific or not to cytoskeleton. For example, at low shear rates the RBC model exhibits TB, whereas vesicles show TT at low enough viscosity contrast for any shear rate. The occurrence of TB for RBCs at low shear rates is due to cytoskeleton, since TT of RBCs would be accompanied by a distortion of cytoskeleton that is significant in comparison to a TB regime. It is only at high enough shear rate (when hydrodynamic shear stress overcomes elastic stress due to cytoskeleton) that RBCs show TT. Regarding shapes, such as slipper, parachute, they are known to be exhibited both by RBCs and vesicles, and the role of cytoskeleton affects only their occurrence region in the parameter space.

In a previous research [Lanotte et al., 2016], Lanotte et al. have reported experimentally on a type of RBCs shapes at high enough shear rates, which has been named multilobe shape. This shape was observed earlier by Fischer [Fischer and Schmid-Schönbein, 1978]. Afterwards, Mauer et al. [Mauer et al., 2018] have conducted a systematic numerical study devoted to the multilobe morphology using two different simulation techniques (dissipative particle dynamics and volume of fluid method). In their model [Mauer et al., 2018], they took into account the cytoskeleton shear elasticity, bending rigidity and cytosol viscosity. A transition from tumbling to multilobe is found at high shear rate and viscosity contrast. They concluded that the cytoskeleton elasticity has an essential role in the manifestation of the MB shape.

3.2 Model and method

The 2D vesicle is represented by a membrane contour that contains a viscous fluid inside and is suspended in another fluid filling the channel. The internal fluid viscosity is denoted as η_1 and the suspending fluid viscosity as η_0. The system is bounded by two rigid walls located at $y = 0$ and $y = L_y$, where L_y is the channel width. The stokes equation is solved using spectral boundary integral equations that described in chapter 2. The fluid in the channel is subject to a linear shear flow :

$$v_x^{\infty}(y) = \dot{\gamma}(y - L_y/2) \tag{3.1}$$

where $\dot{\gamma}$ is the shear rate. Periodic boundary conditions are used along x axis (the flow direction). The period L_x is taken large enough in order to avoid any artifact due to periodic boundary conditions. Typically $L_x = 4L_y$ has proven to be sufficient for our purposes. In this chapter, the reduced area is fixed to 0.65 which is the typical value for RBCs.

3.3 Results and discussion

The aim of the present work is to contribute to the understanding of the minimal ingredients for the occurrence of the MB shapes and investigate the effect of this shape on the rheology. To do that, a systematic 2D simulations study on the vesicle shape was conducted. In our confined 2D vesicle model, only membrane bending is taken into account (we exclude the effect of cytoskeleton). Our results show that MB do exist in this model, ruling thus out the necessity of cytoskeleton. In addition, as these shapes appear at high enough shear rates, bending elasticity is not essential neither (they occur in a regime where hydrodynamic shear stress overcome bending stress). We present a full phase diagram, in the parameter space of viscosity contrast and flow strength. As obtained in 3D for the RBC model [Mauer et al., 2018], the multilobe shapes occur at high enough shear rates and high enough viscosity contrast. The next part will be didacted to the study of the effect of vesicle dynamics on the rhological properties of the vesicle suspension.

3.3.1 The phase diagram of vesicle dynamics and the effect of the confinement on the multilobe occurrence.

In this chapter, a systematic study was conducted at low confinement ($C_n = 0.2$) where the walls play a minor role. The vesicle center was located on the central axis

of the channel. The stability of such centered solutions is discussed below. Several previous studies [Kaoui et al., 2011, Beaucourt et al., 2004, Kaoui and Harting, 2016, Kim and Lai, 2012, Kaoui et al., 2009b] have investigated the dynamics of a single vesicle under shear flow using 2D simulations, but I am not aware of a previous report on a multilobe vesicle. Despite quite high values of shear rates the perimeter and the surface of the vesicle are well conserved during the simulation ; the relative error of the perimeter is less than 1% in all our simulations. Three regimes have been identified : Tank-treading (TT), tumbling (TB) and multilobe (MB). The present phase diagram is in a good qualitative agreement with that of Mauer et al. [Mauer et al., 2018] (their Fig.2). In other words, the topologies of both phase diagrams are quite similar, in the sense that the relative positions of the three modes in the phase diagram present the same typical picture : at low viscosity contrast λ TT always prevails as shown in [Kaoui et al., 2009b]. In our phase diagram TT remains stable at high capillary number showing no transition, whereas at high viscosity contrast λ, the TB prevails at small shear rate $\dot{\gamma}$ and undergoes a transition towards MB at high shear rate $\dot{\gamma}$. Note that the rolling stomatocyte, dyscocyte and tumbling stomatocytes in 3D [Mauer et al., 2018] all degenerate into TB in 2D, since there is no analogue of these shapes in 2D. Figure. 3.1-a shows three transitions, from TB to MB occuring at $\lambda \geq 5.8$ and in the range of $35 \leq C_a \leq 50$, the second transition corresponds to TT-MB, occurring at $\lambda \geq 5.7$ and $C_a \geq 38$, and the last transition is between TT and TB at $C_a < 35$ and $5.5 \leq \lambda \leq 5.8$.

The confinement plays a key role on the multilobe shape manifestation. As we can see in Fig. 3.1-b, the area of MB phase shrinks by about twice when the confinement is doubled ($C_n = 0.4$). It is likely that walls affect excursion of membrane protrusions (which are pronounced for multilobe), and tend to reduce the domain of existence of MB phase. Figure 3.2 shows snapshots of the MB mode. Two types of MB motions can be identified : the irregular one (Fig. 3.2-a) and the regular one (Fig. 3.2-b,c). These two motions correspond to different branches of MB solutions that can coexist in a certain region of λ : We have analyzed this coexistence by analyzing the bending energy of the vesicle as a function of λ for $C_n = 0.2$ and $C_a = 100$ using two initial configurations, one corresponding to the irregular MB solution (such as the one shown in Fig. 3.2-a) and the other one corresponding to the regular MB solution (such as the one shown in Fig. 3.2-c). The final state of the two MB solutions at a nearby value of λ was used as the initial states of the simulation in order to follow both branches as far as possible. The results are shown in Fig. 3.3. As can be seen, three different branches of multilobe dynamics can be identified : a chaotic motion with irregular protrusions

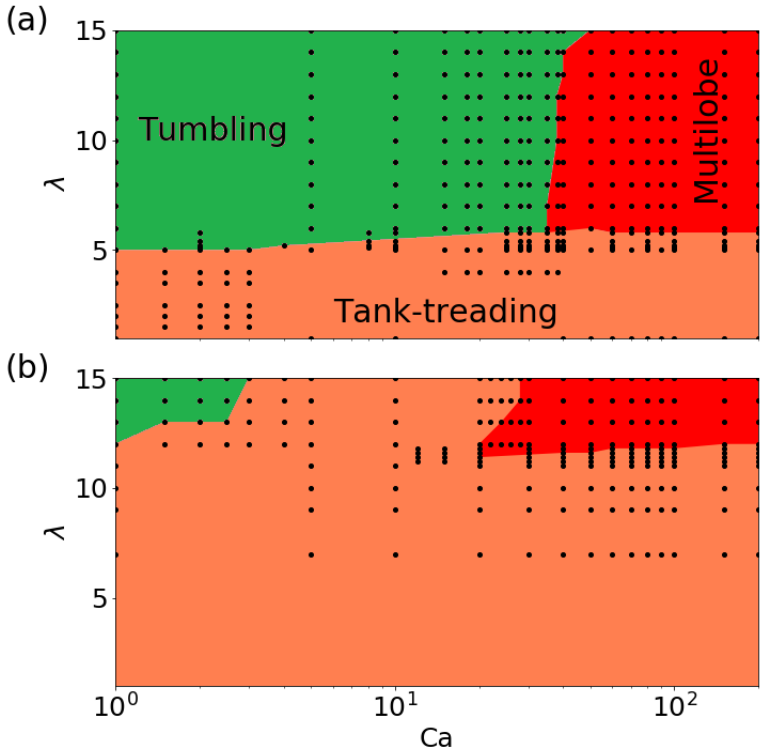

FIGURE 3.1 : Phase diagrams showing the dynamics of a single vesicle. The simulation data are shown as dots. (a) $C_n = 0.2$, (b) $C_n = 0.4$. Top and bottom have the same color code.

traveling along the membrane and two types of tri-lobe dynamics. Interestingly, the transitions between the states are discontinuous.

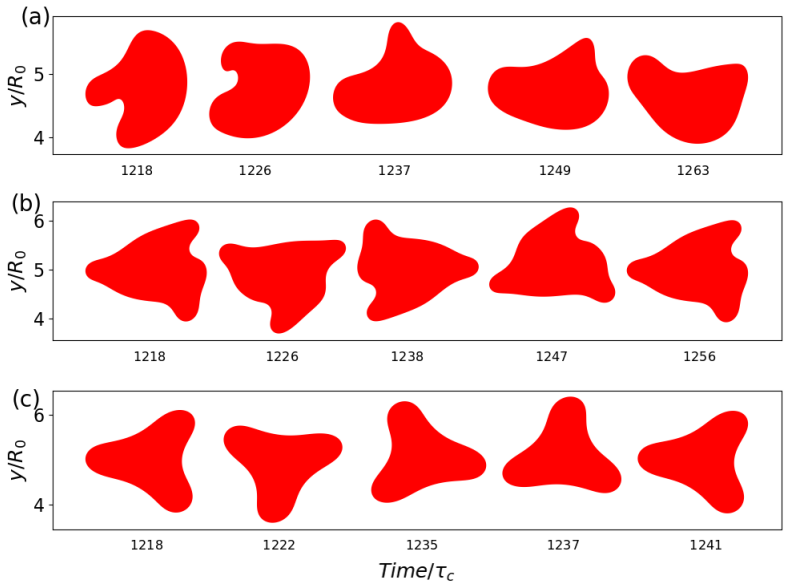

FIGURE 3.2 : Snapshots showing dynamics of a single vesicle. Here we set $C_n = 0.2$ and $C_a = 60.0$. (a) $\lambda = 5.8$, (b) $\lambda = 7.0$, (c) $\lambda = 14.0$. Snapshots (a) show the evolution of the vesicle shape. (b) and (c) show the dynamics of a vesicle over one period.

The initial configuration is prepared to be an elliptical vesicle in the channel center as shown in Fig. 3.4. In the multilobe regime the vesicle starts tumbling and after a few $\tau_c's$ it undergoes a transition towards a quadrilobe shape which is unstable (transient state) and persists for less than $1000\tau_c$. Over long time the shape becomes a trilobe (a stable shape). Note, in agreement with our finding, the quadrilobe shape is not observed as a permanent state in the 3D simulations of [Mauer et al., 2018, Lanotte et al., 2016]. We clearly see that the MB shape occurrence does not require a shear elasticity of the cytoskeleton. The MB shapes occur at large enough capillary numbers where also the bending rigidity is not essential (large capillary number, where MB occurs, means that bending stress is small in comparison to imposed hydrodynamic stress). These shapes result solely from an interplay between tension (resisting compression or dilatation) and the imposed flow.

3.3.2 The rheology of multilobe vesicle

The present section is dedicated to the study of rheological properties, namely the effective viscosity and normal stress difference. The MB transition is accompanied by

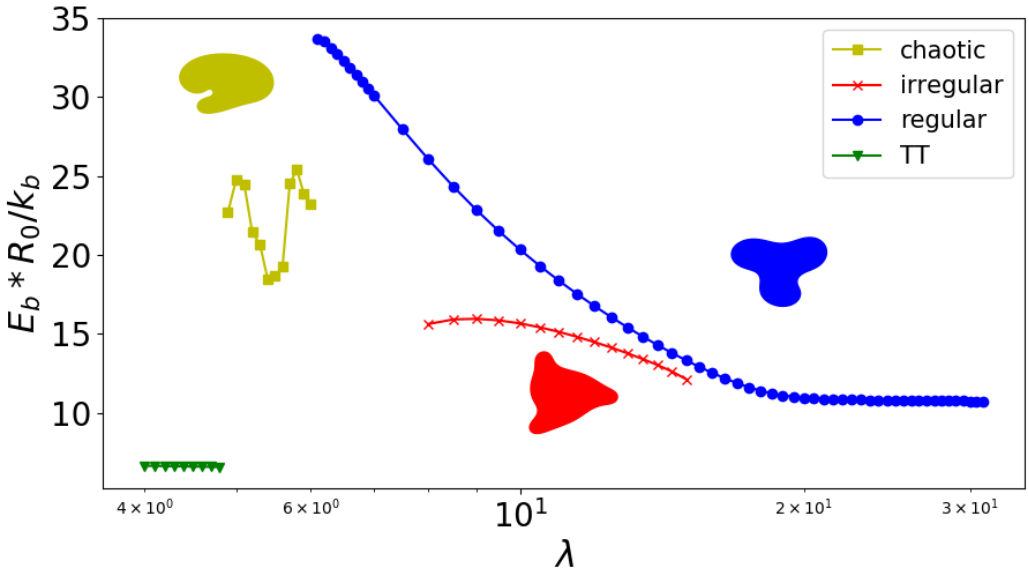

FIGURE 3.3 : Average bending energy of vesicle shapes as a function of viscosity contrast. Insets show characteristic shape sequences for different types of multilobe dynamics. $C_n = 0.2$, $C_a = 100$.

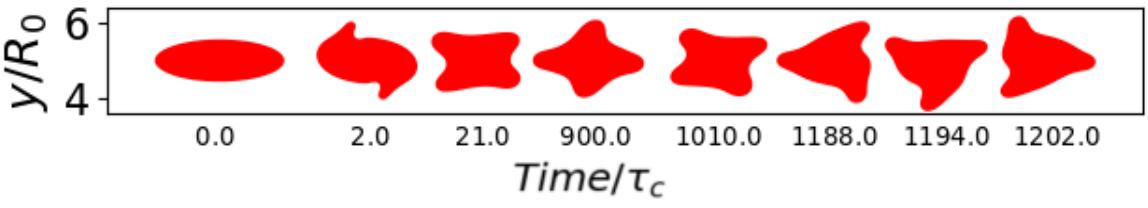

FIGURE 3.4 : Snapshots show the evolution of the vesicle shape from the initial configuration to the steady state. Here we set the confinement $C_n = 0.2$, the capillary number $C_a = 60.0$ and the viscosity contrast $\lambda = 7.0$.

a significant change of the intrinsic viscosity as well as the normal stress difference. We provide few qualitative explanations for these behaviors. The effective viscosity has the following form :

$$\eta = \eta_0(1 + [\eta]\phi), \tag{3.2}$$

where ϕ is the suspension concentration, equal to the ratio between the vesicle area and the area of the calculation domain, and $[\eta]$ is the normalized viscosity (called also the intrinsic viscosity when $\phi \to 0$) representing the vesicle contribution to the viscosity. The effective viscosity is the ratio between the xy component of stress tensor and the applied shear rate :

$$\eta = \frac{< \sigma_{xy} >}{\dot{\gamma}} \tag{3.3}$$

where bracket $< ... >$ denotes an average over the wall length. Alternatively the viscosity can also be obtained as an integral over the vesicle perimeter. Following Batchelor formula [Batchelor, 1970], the normalized effective viscosity is given by :

$$[\eta] = \frac{\eta - \eta_0}{\eta_0 \phi} = \frac{1}{\eta_0 A_0 \dot{\gamma}}[- \int_m y f_x ds + \eta_0(\lambda - 1) \int_m (n_x v_y + n_y v_x) ds]. \tag{3.4}$$

The first term of the normalized viscosity describes the dynamical contribution which is due to the membrane force, and the second term is the kinematic contribution of the vesicle (the membrane velocity). The normal stress difference is defined as $N =< \sigma_{xx} > - < \sigma_{yy} >$. It has been normalized as

$$[N] = \frac{< \sigma_{xx} > - < \sigma_{yy} >}{(\eta - \eta_0)\dot{\gamma}} \tag{3.5}$$

in [Thiébaud et al., 2014]. Here the averaged stress tensor is given by

$$< \sigma_{ij} >= \frac{1}{L_x L_y} \int_{box} (-P\delta_{ij} + \eta_0(\partial_i v_j + \partial_j v_i)) dA - \frac{1}{L_x L_y} \int_m r_j f_i ds + \eta_0 \frac{(1-\lambda)}{L_x L_y} \int_m (n_i v_j + n_j v_i) ds, \tag{3.6}$$

where δ_{ij} is the Kronecker symbol, and r_i is a component (x or y) of the membrane position vector. The first integral is performed over the calculation domain.

We analyze here the evolution of viscosity as a function of capillary number. It has been reported that the effective viscosity of a vesicle suspension may exhibit both shear-thinning and shear-thickening depending on the viscosity contrast [Nait-Ouhra et al., 2018a]. For a given viscosity contrast and upon increasing capillary number, we have a transition from TB to MB (Fig. 3.1). In the TB regime we find a weak shear thinning (Fig. 3.5). At the TB-MB transition the viscosity exhibits a large jump. In this sense the system exhibits a sudden shear thickening. Within the MB regime,

and for not too large viscosity contrast, the suspension shows a shear thinning. For a large enough viscosity contrast the suspension viscosity exhibits a plateau. The sudden increase of the viscosity in the MB regime is traced back to a higher cross section (as explained above). The increase of viscosity in the MB regime is consistent with the experimental report shown in Fig. 4 of Ref. [Lanotte et al., 2016]. The shear-thinning in the MB regime (red triangles in Fig. 3.5), is due to the fact that the MB shape explores less space as the capillary number increases. To quantify this effect, we plot the center of mass as a function of time for two capillary numbers (Fig. 3.6). For each case the center of mass describes an ellipse with an area which decreases with C_a, causing a smaller viscosity.

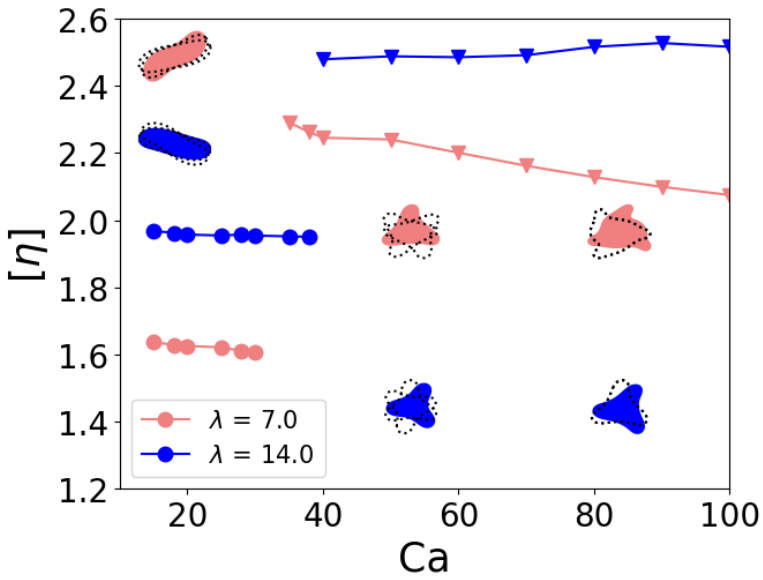

FIGURE 3.5 : The normalized viscosity $[\eta]$ as a function of capillary number C_a for different viscosity contrast λ. The confinement is $C_a = 0.2$. Circles correspond to the TB and triangles to MB dynamics.

In order to investigate the origin of the behavior of the viscosity, we determine the average (over long time) of the occupancy of the cell in the channel. This is reported in Fig. 3.7 as a function of C_a for different values of viscosity contrast λ. We find the following features : (i) when we cross the boundary (as a function of C_a) of the TB-MB phase (occurring at about $Ca \sim 40$) the average occupancy jumps meaning the cell explores more the channel width, and this triggers a jump in the viscosity. (ii) For the upper panel, in the MB regime space occupancy decreases with C_a, explaining the shear thinning for $\lambda = 7$. (iii) In the lower panel the occupancy in the MB phase remains practically constant leading to a plateau in the viscosity behavior.

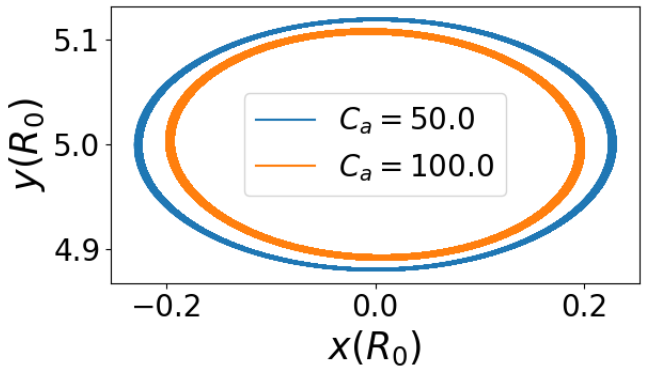

FIGURE 3.6 : The center of mass trajectory for two capillary numbers.

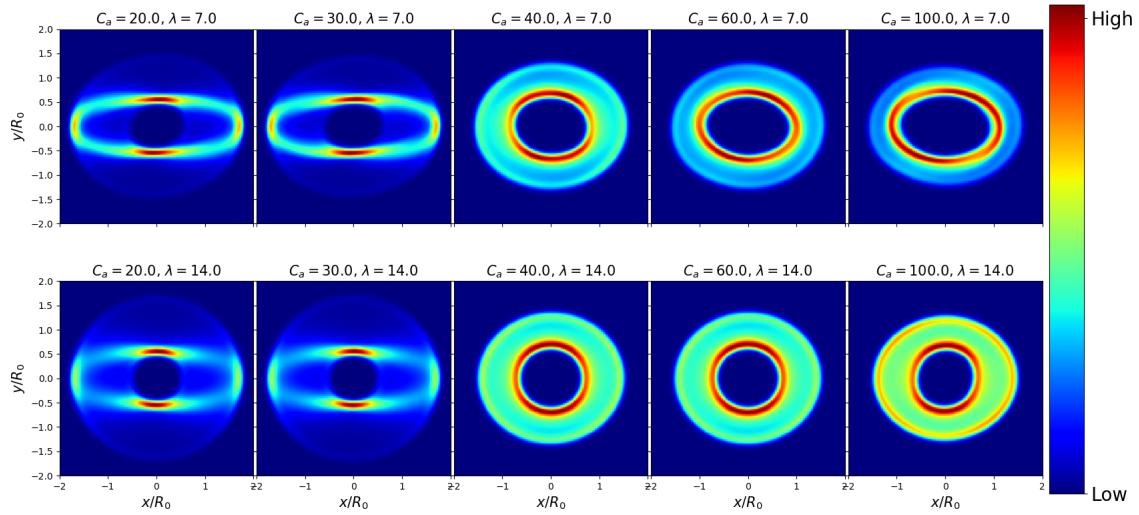

FIGURE 3.7 : The average occupancy as a function of C_a for two different values of λ.

The interpretation of the normalized normal stress difference is more complicated than the normalized effective viscosity. In the TB regime the normal stress difference (Fig. 3.8) is almost zero, before becoming negative (meaning contractile stress) and then acquires a large enough positive value in the MB regime. The membrane incompressibility is a main ingredient, but it enters in an indirect way. The sign of the normal stress difference in the TT regime is fixed by the angle between the flow direction and the long axis of the vesicle (see analytical study in [Danker and Misbah, 2007]). In the TB regime there is periodic evolution of normal stress difference during time (the modulus of the maximum and the minimum are equal), and due to the fact that it switches from positive to negative, the value vanishes when averaged over a period. In the MB regime the vesicle undergoes a complex dynamics. In the vicinity of the TB-MB transition N is negative (contractile), before becoming positive. Sufficiently far from the transition point the vesicle with a lower viscosity contrast has the highest value of normal stress difference. This is traced back to the flexible nature of the shape deformation for low enough viscosity contrast. In Ref. [Danker and Misbah, 2007] it has been shown that normal stress difference depends quadratically with shape amplitude deformation. This gives a hint that less viscous vesicles provide a higher stress due to their larger flexibility

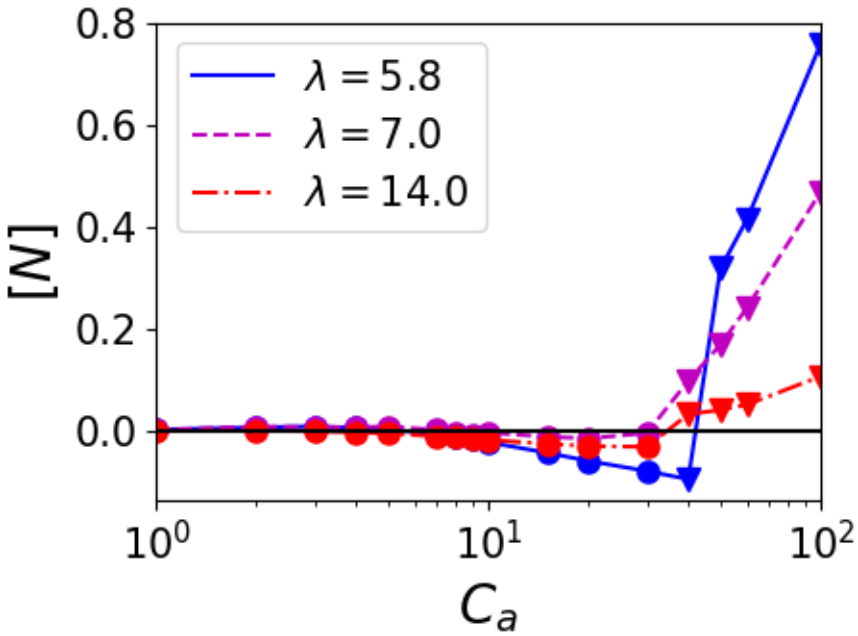

FIGURE 3.8 : The normalized normal stress difference $[N]$ as a function of capillary number C_a for different viscosity contrast λ. $C_a = 0.2$. Circles correspond to TB and triangles to MB dynamics.

3.3.3 Relation between normal stress difference and migration

It is known that the sign of normal stress difference is related to the lateral migration of particles in a suspension [Smart and Leighton, 1991]. Here we use this relation and the measurements of N, obtained above, to analyze the stability of the centered position of the vesicle. Let us first write the relation between N and migration velocity in a channel which will inform us on the direction of migration as a function of the sign of the normal stress difference. For a semi-confined geometry, in which the migration is caused by a single wall (or in a channel so wide that the effect of the farther wall can be neglected), the migration velocity v_m can be calculated analytically and reads :

$$v_m = \frac{N L_x L_y}{8\pi\eta_0(y_0 - y_{wall})}, \tag{3.7}$$

where y_0 is the lateral position of the vesicle center and y_{wall} is the wall position. Equation (3.7) is an asymptotic expression, valid for $|y_0 - y_{wall}| \gg R_0$. This equation is valid whether the wall is above ($y_0 - y_{wall} < 0$) or below ($y_0 - y_{wall} > 0$) the vesicle. For more details and explanations on the Eq. (3.7) see [Crowdy and Or, 2010].

For a vesicle close to the channel center the contributions of both walls have to be taken into account. The sum of the expressions (3.7) with y_{wall} equal to the upper and lower wall positions gives the migration velocity that is only qualitatively correct. This sum however gives the correct scaling for the migration velocity close to the channel center :

$$v_m = -\chi \frac{N(y_0 - L_y/2)L_x}{\eta_0 L_y}, \tag{3.8}$$

where χ is a numerical constant independent of the channel geometry. The asymptotic expression (3.8) is valid under assumptions $|y - L_y/2| \ll R_0 \ll L_y$. We find $\chi = 0.488$ by analyzing the flow due to a point stresslet in an infinite channel.

Figure 3.9 shows the comparison between the migration velocity predicted by eq. (3.8) and the numerical simulation : We place a vesicle close to a wall and measure the lateral migration velocity v_m as a function of the lateral position y. We then compare the rescaled velocity $v_m L_y/\dot{\gamma}R_0^2$ with the theoretical prediction $-\chi N(y - L_y/2)L_x/(\dot{\gamma}\eta_0 R_0^2)$. As can be seen, the agreement is only qualitative for $L_y = 10R_0$ because of the effect of higher-order multipoles in the flow perturbation produced by the vesicle. Increasing L_y to $20R_0$ gives a much better agreement because the effect of higher-order multipoles neglected in (3.8) diminishes with increasing channel width. Further increasing L_y to $40R_0$ makes the numerical curve almost coinciding with the analytical expression close to the channel center. We also observe that changing

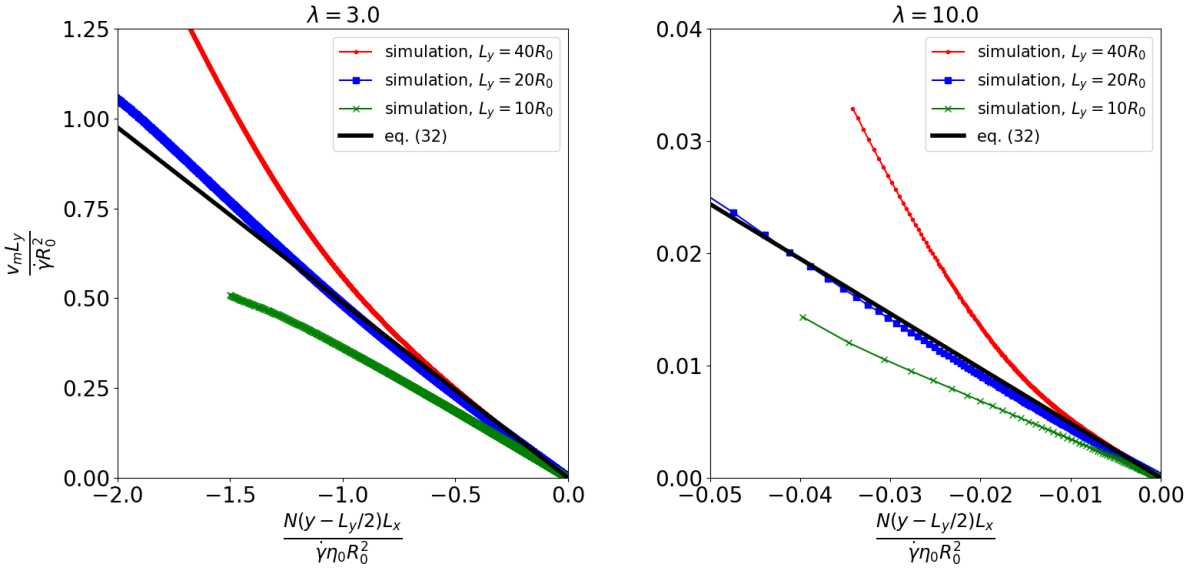

FIGURE 3.9 : Rescaled migration velocity as a function of rescaled lateral position, measured numerically and predicted with eq. (3.8). Left : $\lambda = 3.0$ the vesicle shows tank-treading and right $\lambda = 10.0$ the vesicle shows multilobe.

vesicle parameters, such as viscosity contrast, or reduced area (not shown) does not affect the validity of (3.8).

Expressions (3.7) and (3.8) show that both the particle's migration close to a wall and the stability of its centered position are intimately linked to the sign of the normal stress difference generated by the particle.

According to formula (3.8), the migration is directed towards center of the channel when $N > 0$ and away from center in the opposite case. When $N > 0$ we see that an initial position away from center always leads to an inward migration that pushes the vesicle towards the center. The steady final position (which is defined by the y-position reaching a fixed position in time ; note also that by perturbing the final position we could ascertain the stability of the final position) is at the center (Fig.3.10) (red circles ; the channel width is $L_y = 10R_0$ and center of the channel is at $y/R_0 = 5$). When $N < 0$ the migration is found to be outwards, and the vesicle settles at an off-centered position (red crosses in Fig.3.10). It is seen that the value of C_a at which there is a transition from an off-centered to a centered position occurs is approximately equal to that corresponding to the passage of N from positive to negative (see Fig.3.8). The blue symbols in Fig.3.10 refer to situations where the final position depends on initial position. These position values correspond to a coexistence zone between a centered and off-centered position. The bifurcation structure in Fig.3.10 reveals a

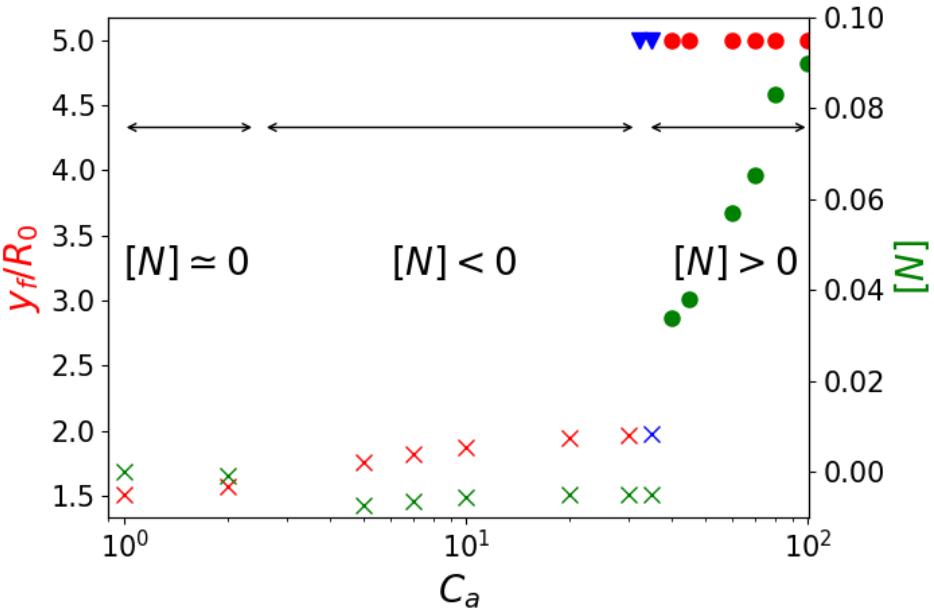

FIGURE 3.10 : Final vesicle position y_f/R_0 for different values of C_a. $L_y = 10R_0$; the center of the channel is at $y_f/R_0 = 5$. $\lambda = 14$. The red circles correspond to final position with $N > 0$, the red crosses to $N < 0$. The blue symbols represent positions which depend on initial conditions. The green symbols represent the normal stress difference.

subcritical nature. Thus we see that the migration and the normal stress difference are intimately related.

3.4 Summary and concluding remarks

A main outcome in this chapter is the fact that the cytoskeleton of a RBC in not essential for the MB shape manifestation ; only membrane tension is responsible for this effect, since the MB phase takes place at high enough capillary number, meaning that shear stress overcomes bending resistance. This finding corroborates the fact that most of the shapes and dynamics observed so far for RBCs are also common to pure lipid vesicles. Typical examples are parachute shape, slipper, bullets, croissant and so on, exhibited by vesicles and RBCs both experimentally and numerically [Franke et al., 2011, Misbah, 2012, Vlahovska et al., 2009, Vitkova et al., 2008, Thiébaud et al., 2014, Barthes-Biesel, 2016, Shen et al., 2018] . The present finding provides further evidence highlighting that a 2D vesicle model already captures many important features. The 2D model can be (due to its rapid handling from computational point of view) very useful in exploring new phenomena, especially for dense suspensions, before resorting to the computationally more expensive RBC model.

Chapitre 4

Erythrocyte-erythrocyte aggregation dynamics under shear flow

The erythrocyte aggregation and disaggregation are two processes taking place reversibly in blood circulation in vivo under physiological conditions. However, in some pathological conditions (diabetes, sickle cell anemia,) the dissociation of aggregates more and more improbable. The mechanism of separation between two adhered RBCs is unclear. In this research, we will provide some explanations of the dissociation as well as of robust aggregation mechanism of erythrocyte-erythrocyte aggregates [Abbasi et al., 2021]. A link to pathological conditions (several common blood diseases) is highlighted.

4.1 Introduction

In a previous work [Bertoluzzo et al., 1999], it has been shown that the RBCs aggregation process starts by the formation of RBC doublets. The doublet formation is a first basic building block for aggregation that should be clarified. Ju et al [Ju et al., 2013] found numerically, using a Morse potential to account for cell-cell interaction (representing depletion forces), that RBC doublet with a homogeneous deformability sustains the adhesion, while an increased deformability difference between the two RBCs forming the doublet favors the doublet dissociation. In another numerical study, Bagchi et al [Bagchi et al., 2005] modeled adhesion between RBCs by the ligand-receptor model (the bridging model). Recently, Flormann et al [Flormann et al., 2017] analyzed the doublet shape in a quiescent fluid *in vitro* and *in silico*, and observed that the contact surface of the doublet is flat for weak adhesion and becomes

of sigmoid-type upon an increase of the adhesion energy (the protein concentration) as shown in figure 4.1. Their results [Flormann et al., 2017] show a good agreement between 2D and 3D simulations and with in vitro experiments. Hoore et al. [Hoore et al., 2018] studied the effect of the spectrin network elasticity on the doublet shapes in equilibrium, and found qualitatively the same doublet shapes found in 2D [Flormann et al., 2017]. More recently Quaife et al. [Quaife et al., 2019] investigated dynamics of a doublet under extensional and shear flows by using a 2D vesicle model. Under a linear shear flow (which is of interest to our study) they observed that the doublet undergoes a tumbling regime, that we shall refer to as *rolling* (for the sake of distinction with the classical single cell tumbling). In our previous work [Abbasi et al., 2021] which is the topic of this chapter, we investigated by means of numerical simulation, the dynamics of RBCs doublets under shear flow and the impact on rheology. We discovered a rich phase diagram of RBCs doublets configurations showing features never evoked before. In particular, we showed that RBCs doublet may be robust even for very high shear stress compromising oxygen delivery to organs and tissues.

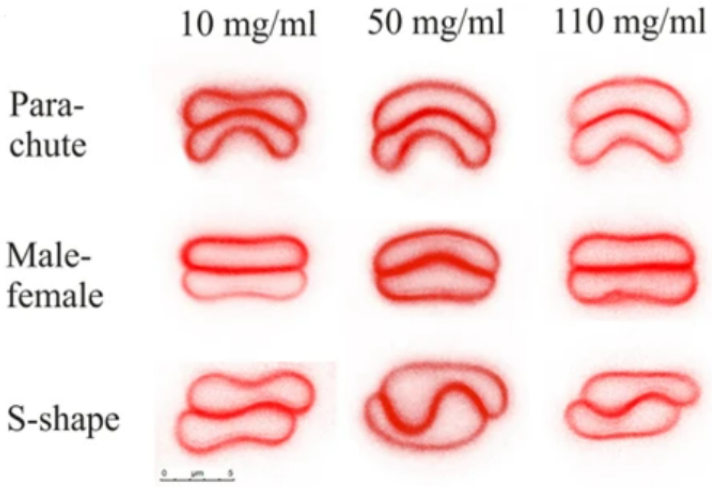

FIGURE 4.1 : Representative shapes of sedimenting doublets for different concentrations of dextran. At each concentration three different types of shapes can be identified : parachute, S-shape and male-female shape [Flormann et al., 2017].

4.2 Method and parameters

Previously, Brust et al [Brust et al., 2014] quantified the interaction energy between two RBCs at various fibrinogen and dextran levels using single cell force microscopy. From their data (table 4.1), we can estimate which range of protein level corresponds

to our simulation condition. When the contact length of two adhering vesicles is larger than the equilibrium distance h, the interaction energy per unit surface is practically the energy of adhesion between two infinite plates. The distance h corresponds to the minimal energy between two points, and does not necessary correspond to the minimal energy for two planar surfaces. Let us denote that distance h_p (see Fig.4.2). We first calculate the energy for a given separation h_p, the adhesion energy is defined in subsection **??**

$$\varepsilon_{adh} = -\varepsilon \int_{-\infty}^{\infty} \phi(\sqrt{x^2 + h_p^2}) dx = \varepsilon \int_{-\infty}^{\infty} \left[2 \left(\frac{h^2}{h_p^2 + x^2} \right)^3 - \left(\frac{h^2}{h_p^2 + x^2} \right)^6 \right] dx, \tag{4.1}$$

$$\varepsilon_{adh} = \varepsilon \left(\frac{3\pi h^6}{4h_p^5} - \frac{63\pi h^{12}}{256 h_p^{11}} \right) \tag{4.2}$$

where x is the coordinate along the vesicle-vesicle contact line. We easily find that this energy has a minimum for $h_p = (231/320)^{1/6} h$, and is equal to :

$$\varepsilon_{adh} \simeq 1.6862 h\varepsilon. \tag{4.3}$$

This will define the adhesion energy of the doublet. The dimensionless macroscopic adhesion energy (to be referred to in all following results) is defined as

$$\bar{\varepsilon}_{adh} = \frac{\varepsilon_{adh} R_0^2}{k} \tag{4.4}$$

We will take typical values of RBC membrane rigidity $k = 4\ 10^{-19}$ J and radius $R_0 = 3\ \mu$m.

Fibrinogen concentration mg/ml |	0.898	2.391	6.597	8.098
Interaction energy $\mu J/m^2$ |	-1.884	-2.719	-4.922	-6.566
Dimensionless macroscopic adhesion energy $\bar{\varepsilon}_{adh}$ |	42.38	61.17	110.74	147.73

TABLE 4.1 : Fibrinogen level versus Interaction energy between two RBC measured using atomic force microscopy [Brust et al., 2014]

The strategy followed in this work consists in preparing initially two vesicles in the middle of the channel, separated by a small distance that allows them to adhere to each other in the absence of an applied flow as describe in Eq. 3.1. Once they adhere to each other and reach a steady state configuration, which depends on the adhesion strength, a shear flow is applied. The study of conformation of vesicle doublet in the absence of flow allowed us to perform benchmarking of our code by reproducing previous results [Hoore et al., 2018, Flormann et al., 2017].

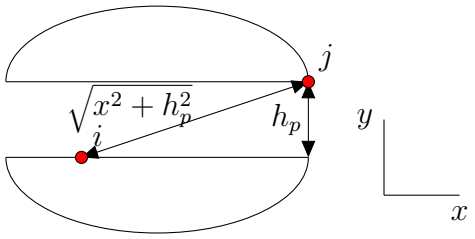

FIGURE 4.2 : Notations

4.3 Results and discussion

4.3.1 Effect of viscosity contrast, flow strength and adhesion on the phase diagram of doublet

The simulation parameters are chosen in a way to produce tank-treading and tumbling of a single vesicle. Firstly, the confinement value is fixed 0.4 where the walls play a minor role, and the doublet dynamics is explored in wide range of adhesion strength and flow strength for two values of viscosity contrast ($\lambda = 1.0, 10.0$). A single vesicle exhibits tank-treading dynamics in the viscosity contrast range from ($\lambda = 1.0$) (and also below that value) to approximately ($\lambda = 12.0$). The reduced area value is fixed to 0.65 (which is inspired by that of human RBCs).

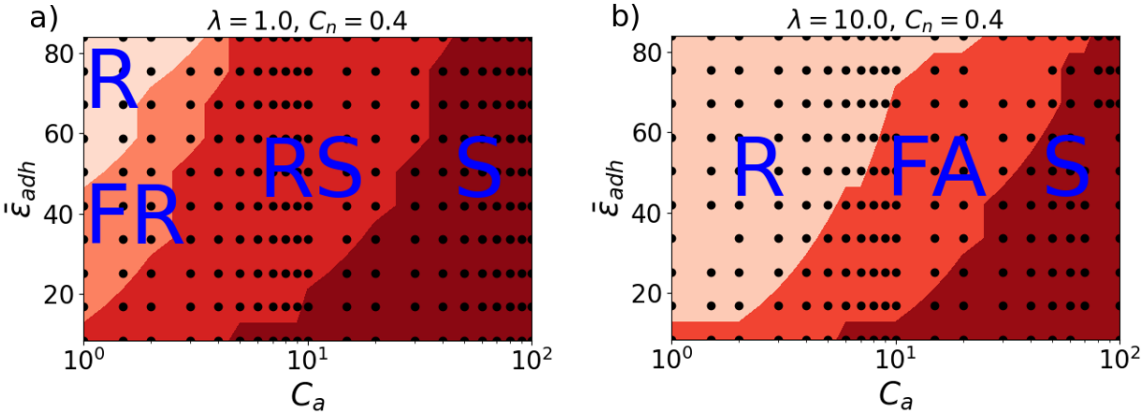

FIGURE 4.3 : Phase diagrams showing the different behaviors of doublet in the parameter space of the capillary number and the dimensionless macroscopic adhesion energy. The simulation data are shown as dots. (a) $\lambda = 1.0$, (b) $\lambda = 10.0$.

Immediately after the doublets reaches the steady state configurations at equilibrium (i.e. in the absence of external flow), a linear shear flow is applied with different shear rate values to the suspension and we analyzed the doublet dynamics. Let us first describe the phase diagram before giving a theoretical foundation to each phase exhibited by the doublet. Four regimes have been identified in the case of $\lambda = 1.0$:

- At low capillary number the rolling phase : the two vesicles remain attached with constant contact length and show a rolling motion (akin to tumbling ; see Fig. 4.4-a). This regime is denoted as R in Fig. 4.3-a.
- When the adhesion energy decreases the contact interface shape transits from sigmoid to a flat interface during time as shown in the snapshots of (Fig. 4.4-b).
- Increasing the capillary number the phase (FR) undergoes a transition towards a phase of rolling+sliding (RS ; the doublet shows rolling accompanied with a sliding between the vesicles ; the length contact changes during time by oscillating between two values (Fig. 4.4-c)). The sliding of the two vesicles on each other is due to the competition between the aggregation and dis-aggregation (flow) forces, as well as due to tank treading of each membrane. This regime is denoted as RS in (Fig. 4.3-a
- At high capillary number the separation between the vesicles takes place, meaning the dis-aggregation force due to flow is high enough to overcome the adhesion between vesicles. This regime is denoted as S in Fig. 4.3-a. We will see below situations where a doublet may persist whatever the magnitude of the shear flow is.

In order to check the robustness of our results and to investigate the effect of the cytoskeleton effect on the doublet dissociation, we will show and discuss our 3D simulations in section 4.3.5 where the RBCs is modeled by adopting a capsule model with shear elasticity.

4.3.1.1 Theoretical foundation to the phase diagram

We have seen in [Flormann et al., 2017] that at equilibrium (absence of flow) at small adhesion the cell-cell interface is flat while at large enough adhesion energy the interface is deformed as shown in figure 4.1. The passage from the flat to the deformed configuration is a supercritical bifurcation. The shape of the cell-cell interface is characterized by the value of the amplitude of deformation of the contact zone between cells A_s (when the contact interface is flat $A_s = 0$, and when the interface has a sigmoid form $A_s \neq 0$). Figure 4.5 (blue symbols) show the supercritical bifurcation that we have reproduced here. After the bifurcation there are two states (the upper and lower branches) where the two corresponding doublet shapes (called state 1 and state 2 in Fig. 4.6) are mirror-symmetric with respect to a horizontal mirror. In the presence of flow the sigmoid interface confers chirality to the doublet,

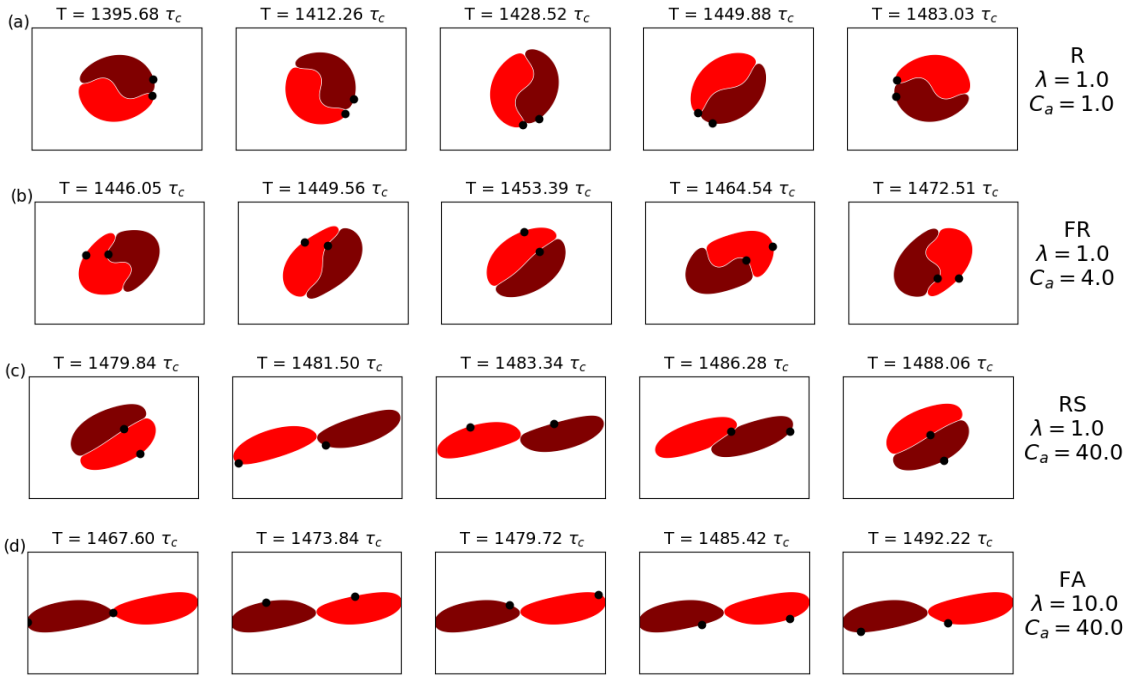

FIGURE 4.4 : Snapshots showing the dynamics of vesicle doublet for different capillary number C_a and viscosity contrast λ . Here $\bar{\varepsilon}_{adh} = 84.00$ and $C_n = 0.4$. The snapshots are taken over one period of the doublet dynamic.

as explained in Fig. 4.6. The order parameter A_s is a measure of the chirality of the doublet. Hence we conclude that the transition from a straight doublet interface at low adhesion to a sigmoid interface at high adhesion, as observed without flow, is a transition from achiral to chiral states. The shear flow is chiral as well : Writing the shear flow as $(\dot{\gamma}y, 0)$, we see that it can be represented as a sum of an elongational flow $(\dot{\gamma}y/2, \dot{\gamma}x/2)$ and a rotational flow $(\dot{\gamma}y/2, -\dot{\gamma}x/2)$. While the elongational flow is achiral, the rotational flow is clearly chiral. It is also easy to check directly that no rotation of coordinates can transform flow $(\dot{\gamma}y, 0)$ into flow $(-\dot{\gamma}y, 0)$. Because the shear flow is chiral, a doublet subject to this flow is chiral regardless of the adhesion energy. Indeed, if the shape of the doublet under shear flow were achiral, the membrane and adhesion forces would also be achiral, while the viscous forces of the chiral flow applied to an achiral shape are chiral. It would thus be impossible for the two to balance each other (and to respect a force-free condition).

A systematic analysis (Fig. 4.5, red symbols) shows a typical diagram of an imperfect bifurcation. When adhesion is small, and starting from state 1 or state 2 (Fig.4.6), the final solution tends always to the same branch (upper red branch ; Fig.4.5). If the adhesion energy is beyond the turning point of the lower branch corresponding to the imperfect bifurcation (where dashed red line starts), we find that an initial doublet

configuration with state 1 leads ultimately to the upper branch while state 2 tends to the lower branch. The imperfect bifurcation allows us thus to distinguish between FR and R. At low energy (before turning point) the solution corresponds to FR solution and after turning point to R solution. The turning point corresponds to a demarcation line between FR and R. Let us provide a qualitative picture of the imperfect

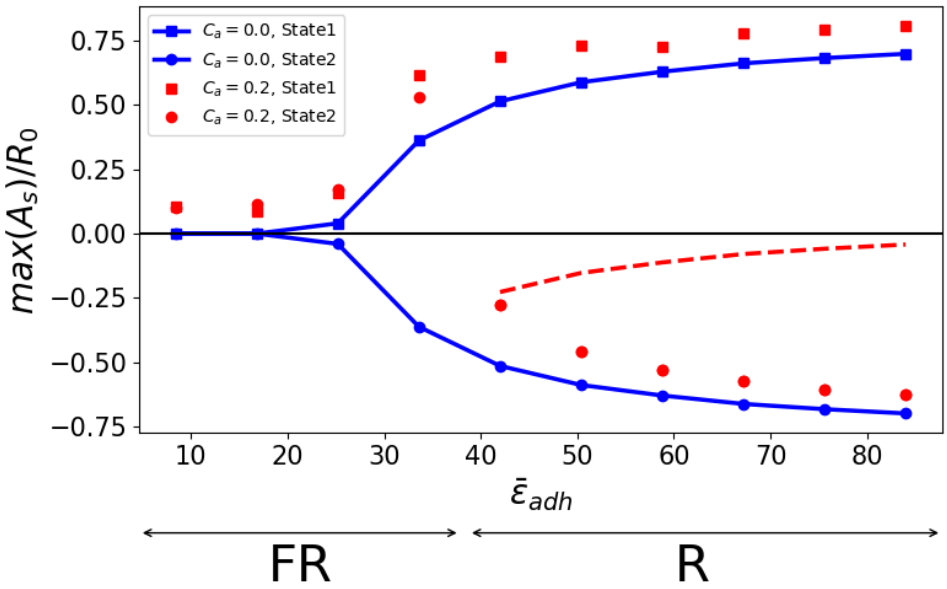

FIGURE 4.5 : Bifurcation diagram in the absence of flow (blue) and in the presence of flow (red) showing maximum deformation amplitude of the contact line. Dashed line is the unstable branch (drawn by hand since the unstable branch can not be captured by dynamics). The red branches are captured by starting from two different initial conditions (state 1 and 2, shown in Fig.4.6. Note that if for state 1 the amplitude of the contact line deformation is counted positive, then it is negative for state 2, and vice versa. Below the turning point we have FR phase and beyond we have R phase.

bifurcation. We have seen in [Flormann et al., 2017] that the energy associated with interface deformation (with amplitude A_s) can be written as $a(\beta - \beta_c)A_s^2 + bA_s^4$, with $\beta \sim \epsilon_{adh}/\kappa$, β_c the critical value for bifurcation, and a and b are positive constants. In the presence of flow the work due to interface deformation is proportional to CaA_s (changing the direction of flow changes sign of deformation, leaving CaA_s invariant). The total energy takes thus (apart from numerical prefactors) the form

$$E = CaA_s + a(\beta_c - \beta)A_s^2 + bA_s^4 \tag{4.5}$$

If $Ca = 0$ the energy is minimal for $A_s = 0$ if $\beta < \beta_c$ (low adhesion), and is minimal for $A_s \neq 0$ when $\beta > \beta_c$. In the presence of flow the energy has a typical form of imperfect bifurcation. Setting derivative of E with respect to A_s to zero yields a cubic

equation for A_s which has either a single (non zero) real solution or three real solutions depending on β (for a given Ca). This is nothing but the bifurcation represented in red in Fig. 4.5 showing a single solution with $A_s \neq 0$ at small adhesion and three solutions at large adhesion.

The transition from FR to RS corresponds to a sudden relative complete sliding of the two cells with respect to each other. By complete we mean that the surfaces slides from one end to the other where the two cells remain pinned by a very small area (Fig. 4.4c) ; the two cells slide back and forth during time. Figure 4.7 shows the minimal area of contact as one crosses the boundary $FR - RS$ showing a sudden jump. Increasing Ca may either lead to FA or S phase. In the FA phase the two cells align steadily with the flow, where each cell exhibits tank-treading (Fig. 4.4d). Finally the S phase corresponds to the situation where the two cells cease to be bound to each other.

4.3.1.2 Effect of viscosity contrast

In the present paragraph we evaluate the effect of the viscosity contrast on the phase diagram discussed above. The results are shown in Fig. 4.3-b for $\lambda = 10$. Several observations are made. First, the rolling region becomes wider if viscosity contrast is increased. Second, the rolling-sliding phase is absent for this viscosity contrast, in favor of a flow-alignment (FA) phase (Fig. 4.4-d)). In this phase the vesicles align with the flow direction, remain attached and they show a tank treading motion of their membrane.

In order to shed some light on the origin of the flow alignment at high viscosity contrast, we performed simulations on a single vesicle at fixed values of the capillary number C_a, the confinement C_n and we varied only the viscosity contrast λ. Figure 4.8 shows that the inclination angle Ω of a single vesicle (the angle between the long axis of the vesicle and the flow direction) decreases with the viscosity contrast, until it aligns with the flow direction at high viscosity contrast. In this configuration (flow alignment) the doublet is in an orientation with a small extensional tension which is not efficient to enforce the two vesicles to slide with respect to each other.

4.3.2 The mechanism of doublet separation

One major question is whether or not doublet formation is reversible *in vivo*, and whether there is any simple criterion (or hint) to answer this question. With this regard, Chien et al [Chien et al., 1990] investigated experimentally the dis-aggregation

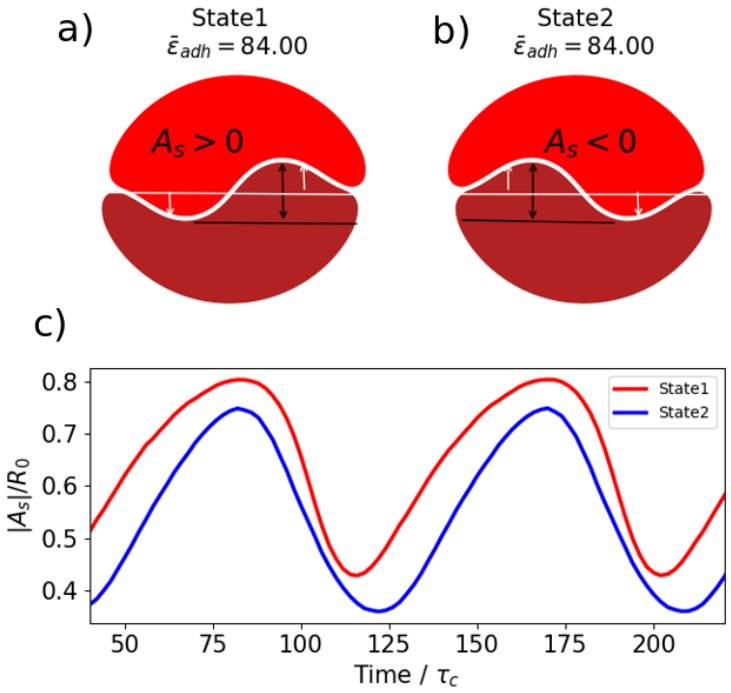

FIGURE 4.6 : (a) The two states 1 and 2 . (b) The time evolution of the amplitudes of the interface between the two cells for a given situation corresponding to the two branches in Fig.4.5 in the regime of R phase. A_s is defined as the algebraic amplitude measuring maximum algebraic values. More precisely, the amplitude is positive if the interface is displaced counterclockwise (see upward and downward white arrows in left panel) from the straight line segment joining the two endpoints of the interface (shown as white horizontal line) and negative if displaced clockwise (right panel). For example it is positive in a) and negative in b). The black arrow shows the value of A_s. c) We see from amplitude evolution an asymmetry between the two branches confirming the imperfect bifurcation in Fig.4.5.

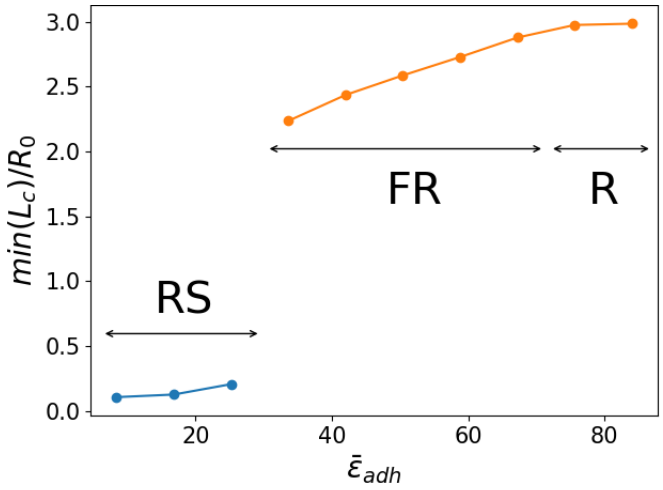

FIGURE 4.7 : Minimal contact length between the two cells as a function of adhesion energy showing its collapse when passing FR to RS.

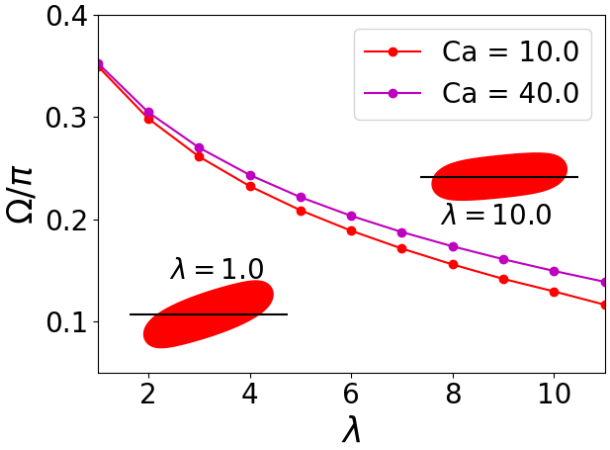

FIGURE 4.8 : Inclination angle of a single vesicle as a function of viscosity contrast λ. The angle decreases with λ. The snapshots show the vesicle under shear flow of $C_a = 10.0$.

of RBC doublets under oscillatory shear flow. They prepared two adhered cells in a flow channel where the bottom cell adheres to a fixed plane and a polystyrene latex particle is used as a marker on the top cell. By applying an oscillatory shear flow they observed that the velocity of the latex bead is twice the velocity of the upper cell. From this it was concluded that the detachment occurs as rolling of the top cell along the bottom one and not as sliding. In other words, the bottom surface of the top cell remained stationary in the lab frame except at the point where the detachment occurred, while the velocity of the top surface of the top cell was twice that of its center of mass. This motion is similar to tank-treading in the reference frame co-moving with the top cell, where its top and bottom surfaces move with opposite velocities, while the overall shape of the cell remains virtually unchanged. Thus the ability of the cell membrane to tank-tread is essential for the doublet separation. We now use our model to see whether preventing the membrane from tank-treading would have an effect on doublet dissociation.

4.3.2.1 Supression of doublet separation

We have seen above that there exists (Fig. 4.3) a region of separation (region S) for a given set of parameters. In both diagrams of Fig. 4.3 the separation phase (S) is preceded either by RS or FA phase. In both of the latter two phases the membrane undergoes tank-treading. The question naturally arises of whether or not the separation phase is associated with the existence of membrane tank-treading. We have thus investigated if the suppression (or a significant reduction) of membrane tank-treading may affect separation. For that purpose we have chosen a wide enough

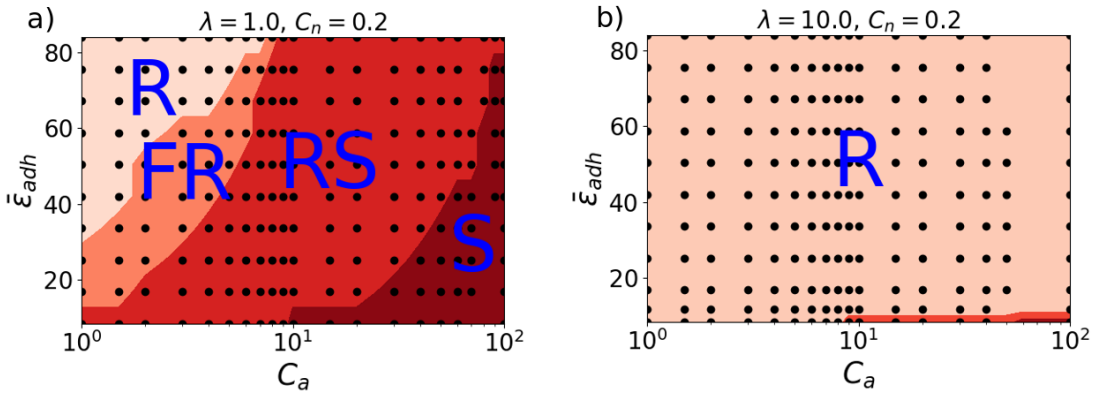

FIGURE 4.9 : Phase diagrams showing the different behaviors of doublets in the parameter space of the capillary number and the dimensionless macroscopic adhesion energy. The simulation data are shown as dots. (a) $\lambda = 1.0$, (b) $\lambda = 10.0$.

channel ($C_n = 0.2$) and only varied the viscosity contrast λ in order to reduce membrane tank-treading. As a guide, we have first analyzed the case of a single vesicle and determined the critical λ for the transition from tank-treading to tumbling, and found $\lambda \simeq 7.0$ (note that when $C_n = 0.4$ this transition takes place at about $\lambda = 12$). This means that for $C_n = 0.2$ a single vesicle shows tank-treading for $\lambda = 1$ and tumbling for $\lambda = 10$. We have analyzed the phase diagram for these two values and the results are shown in Fig. 4.9. For $\lambda = 1$ the same overall picture is found as in Fig. Fig. 4.3a. However, the situation is drastically different when $\lambda = 10.0$ (Fig. 4.9-b). Indeed, we see that RS and S phases are almost absent, and they appear only for extremely weak adhesion, far below physiological ranges. In other words, the doublet seems to be very robust even for a very large capillary number. We have attempted to dig further into this result. The doublet precise shape is a compromise between adhesion, which tends to increase vesicle-vesicle interface (like sigmoid shape) and bending energy, which tends to minimize deformation, favoring a flatter interface. Deformation ability can be measured by C_a, and dimensionless macroscopic adhesion energy by $\bar{\varepsilon}_{adh}$. An enlightening representation of our result Fig. 4.9 is to plot $\bar{\varepsilon}_{adh}$ as a function of $C_a/\bar{\varepsilon}_{adh}$. The results are shown in Fig. 4.10. This clearly shows that the shape adapts itself to shear flow. Indeed, if that were not the case, namely that the doublet conformation were independent of C_a for given adhesion energy, then the R/RS and RS/S phase borders observed for the lowest dimensionless macroscopic adhesion energies would continue vertically to high dimensionless macroscopic adhesion energies (in the representation of Fig. 4.10). In other words, the transition value of $C_a/\bar{\varepsilon}_{adh}$ would be independent of adhesion energy. Indeed, if bending energy saturates, the only remaining two energy scales are shear and adhesion ones, so that

the critical $C_a/\bar{\varepsilon}_{adh}$ would have been a numerical constant. The fact that the phase diagram in the new representation shows the same trend as in Fig. 4.9-b is a clear indication that the doublet adapts its shape in order to escape dissociation. Figure 4.11 shows some doublet shapes highlighting adaptation to shear flow. Our results are consistent with the work of Chien et al. [Chien et al., 1990], in that membrane tank-treading plays an important role in doublet dissociation.

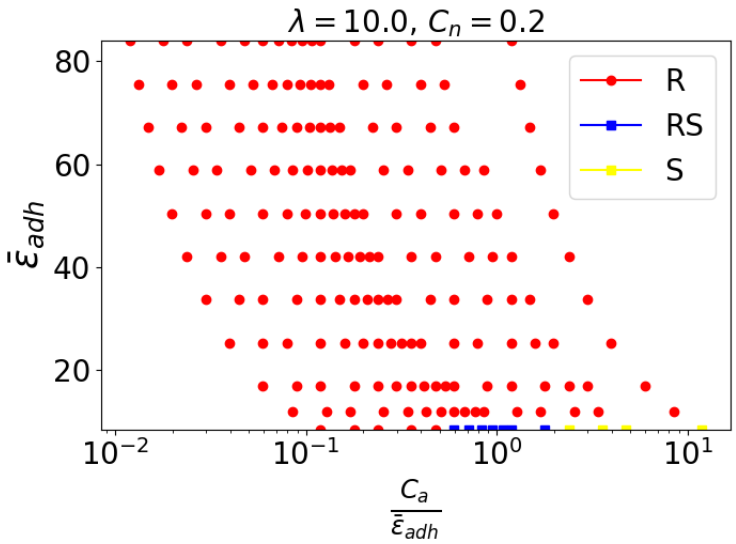

FIGURE 4.10 : Phase diagrams showing the different behaviors of doublets in the parameter space of the dimensionless macroscopic adhesion energy and the ratio of capillary number over dimensionless macroscopic adhesion energy. The simulation data are shown as dots.

In human vascular networks we expect membrane tank-treading to take place in arterioles only (the only vasculature site where shear rate can reach values of about few 10^3 s^{-1}) [Yazdani and Bagchi, 2011, Fischer and Korzeniewski, 2013b]. In some RBCs diseases, such as thalassemia [Advani et al., 1992], sickle-cell disease [Brandao et al., 2003] and malaria [Glenister et al., 2002], the membrane shear modulus as well as cytoplasm viscosity may be significantly higher than healthy ones. The corresponding shear rate beyond which membrane tank-treads may become significantly larger for pathological cells [Yazdani and Bagchi, 2011] so that its occurrence in vivo becomes unlikely. We can speculate that in this case RBC doublets and larger aggregates become irreversible, compromising thus a proper blood perfusion to tissues and organs.

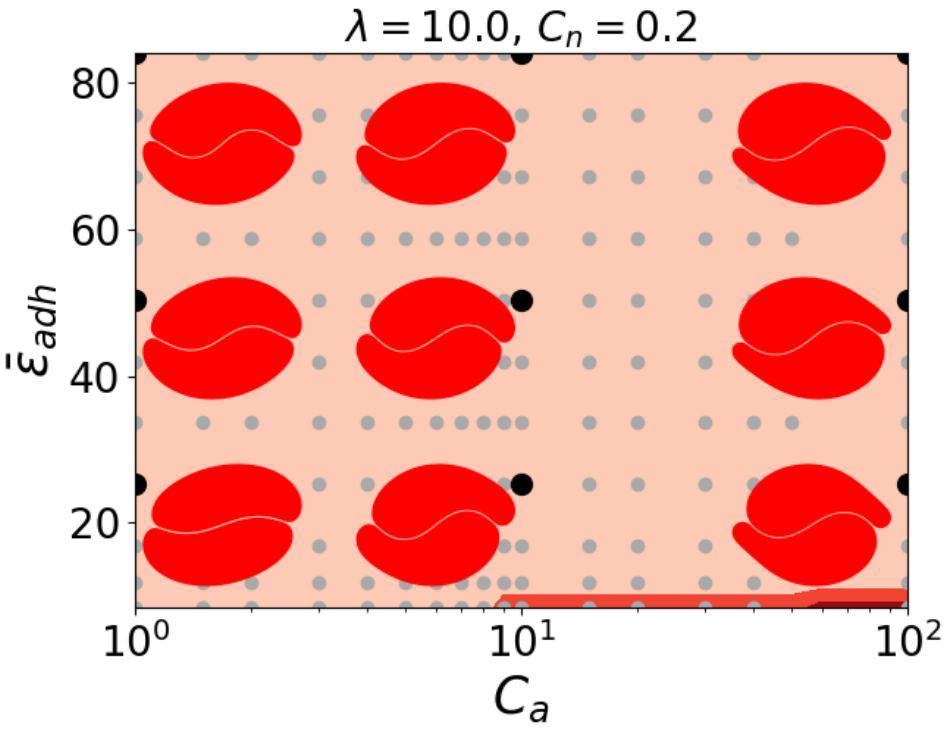

FIGURE 4.11 : Phase diagrams (same as in Fig.4.3) showing few shapes of doublet in the parameter space of the capillary number and the dimensionless macroscopic adhesion energy. The simulation data are shown as dots. The darkest spots indicate the pairs of parameters for which the shape is shown. We clearly see shape adaptation as C_a increases.

4.3.3 The effect of adhesion energy on the rhological properties of doublet.

The goal of the present section is to explore the effect of doublet dynamics discussed above on the rheological behaviors of a doublet suspension. In order to quantify rheology we analyze the normalized viscosity. Here we consider the very dilute regime. We recall that the effective viscosity can be written in the following form :

$$\eta = \eta_0(1 + [\eta]\varphi) \tag{4.6}$$

where φ is the vesicle concentration, and $[\eta]$ is the normalized viscosity (called also the intrinsic viscosity), representing the doublet contribution to the viscosity. The effective viscosity is the ratio of the xy component of stress tensor to the applied shear rate :

$$\eta = \frac{< \sigma_{xy} >}{\dot{\gamma}} \tag{4.7}$$

Where bracket $< ... >$ means a surface average (i.e. average over the simulation area). Following Batchelor [Batchelor, 1970], the normalized viscosity is given by :

$$[\eta] = \frac{\eta - \eta_0}{\eta_0 \varphi} = \frac{1}{\eta_0 A \dot{\gamma}} \sum_i \left[\int_{m_i} y f_x ds + \eta_0(\lambda - 1) \int_{m_i} (n_x v_y + n_y v_x) ds \right] \tag{4.8}$$

The first term of the normalized viscosity describes the dynamical contribution which is due to the membrane force, whereas the second term represents the kinematic contribution of the vesicle (the membrane velocity).

We first analyzed how the normalized viscosity $[\eta]$ changes during time for increasing adhesion energy with a viscosity contrast $\lambda = 1.0$ and low capillary number $C_a = 1.0$. Figures 4.12a-d show that the viscosity of the suspension is periodic with time. At very low adhesion strength the doublet shows RS regime (Fig. 4.12a). This state undergoes a transition towards the R-regime at high adhesion strength ((Fig. 4.12d). This transition is accompanied by an increase of the amplitude of the normalized viscosity. In the R-phase the contact interface of the doublet does not evolve with time. The amplitude as well as the period of the normalized viscosity oscillation decreases with the adhesion strength. This is attributed to the fact that the two vesicles become more and more pinned to each other (Fig. 4.12d) as the adhesion energy increases, so that the overall cross section of the doublet which is exposed to the flow decreases, opposing thus less resistance.

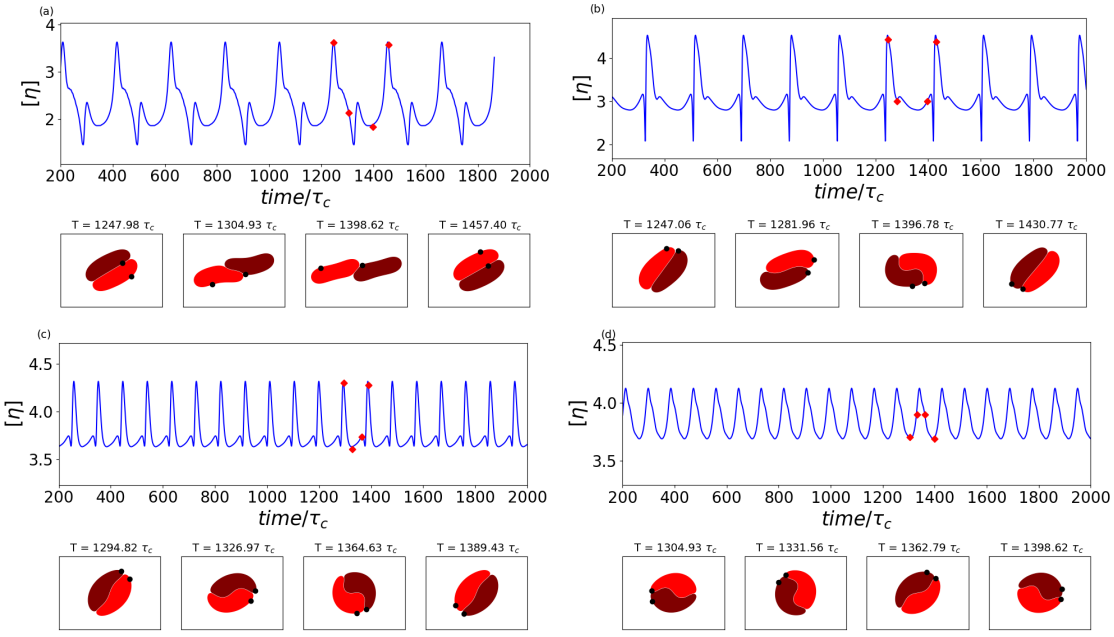

FIGURE 4.12 : Evolution of the normalized viscosity $[\eta]$ as function of time. The snapshots are taken over one time period as shown with the red dots. Here $\lambda = 1.0$, $C_n = 0.4$ and $C_a = 1.0$ (a) $\bar{\varepsilon}_{adh} = 5.30$, (b) $\bar{\varepsilon}_{adh} = 23.40$, (c) $\bar{\varepsilon}_{adh} = 41.80$, (d) $\bar{\varepsilon}_{adh} = 84.00$

4.3.3.1 Time average rheology of doublet suspension

As seen above a single vesicle is known to exhibit both tank-treading motion (at low viscosity contrast) and tumbling motion (at high viscosity contrast). A suspension of vesicles exhibit both shear thinning and shear thickening depending on viscosity contrast [Nait-Ouhra et al., 2018a]. Here we find that the doublet suspension always exhibits shear thinning for the set of parameters explored so far. The results are shown in Fig. 4.13 (note that capillary number axis in Fig. 4.13 is shown in logarithmic scale). In all the three studied cases (Fig. 4.13a,b,c) the viscosity collapses by about 50%. A common feature shown in Fig. 4.13a,b,c is that all curves (obtained for different adhesion energies) collapse on the same curve for high enough capillary number. This collapse corresponds to the situation where all doublets are dissociated.

The persistence of shear thinning here is quite natural. Indeed, as Ca increases we have succession of phases that tend to lower cross section of the doublet against the flow. At low Ca the doublet shows a rigid-like rolling (R). Increasing Ca leads to FR. Because in this case the doublet flattens during time (due to interface flexibility), we expect that the doublet offers less flow resistance. Similarly, in the RS and FA regimes the doublet spends some time (RS) in the aligned direction with the flow,

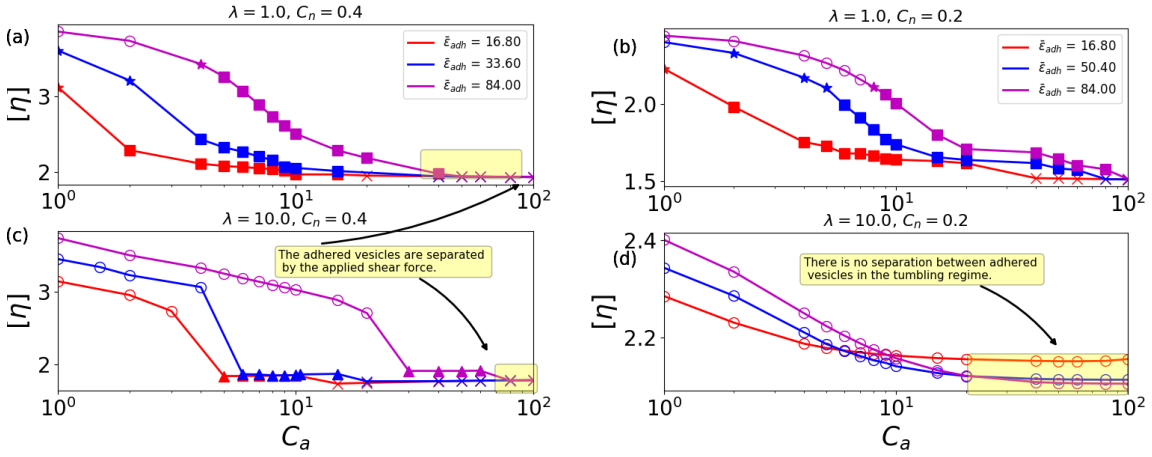

FIGURE 4.13 : The normalized viscosity $[\eta]$ as a function of capillary number C_a for different dimensionless macroscopic adhesion energy $\bar{\varepsilon}_{adh}$. The simulation data are shown as dots. (a) $\lambda = 1.0$ and $C_n = 0.4$, (b) $\lambda = 10.0$ and $C_n = 0.4$, (c) $\lambda = 1.0$ and $C_n = 0.2$, (d) $\lambda = 10.0$ and $C_n = 0.2$. Circle symbol represents the rolling phase, star : flexible rolling, square : rolling + sliding, triangle : flow alignment, cross : separation.

and this should lead to viscosity reduction. In the FA regime the doublet viscosity is constant with shear rate since the FA configuration remains steady during time.

Figure 4.13d shows a peculiar behavior, in that the curves do not collapse at large capillary number, due to the absence of dissociation. This figure shows the following behavior : at low capillary number the suspension with high dimensionless macroscopic adhesion energy has a higher normalized viscosity (which is quite intuitive), but at higher capillary number the opposite is found.

Let us provide an argument for this behavior. For a low dimensionless macroscopic adhesion energy(say the red curve in Fig. 4.13d) and at low capillary number the doublet shows the R motion where the contact length between the two vesicles oscillates in time while keeping sigmoid shape (not to be confused with FR. For a higher adhesion (say the blue curve in Fig. 4.13d), and at low capillary number, the contact surface has a persistent sigmoid shape. In other words, for a high enough adhesion the doublet is quite rigid in its configuration yielding a higher viscosity, as intuitively expected. When the capillary number increases, for the low adhesion case (the red curve in Fig. 4.13d), the shear stress is strong enough to pull on the doublet leading to a peeling off the tail of each vesicle at the poles. The extra tails that stick out of the vesicles increase the cross section of the doublet, leading to a higher viscosity than the case where adhesion is stronger (preventing tails to stick out of the doublet). This explains why, at high capillary number, for weak adhesion the viscosity is higher than for strong adhesion (the blue and red curves intersect).

Finally, let us quantify the effect of the dimensionless macroscopic adhesion energy on the normalized viscosity. Note that the range of the dimensionless macroscopic adhesion energy from 5.0 to 75.0 corresponds to the physiological conditions of fibrinogen level (these values are estimates from [Brust et al., 2014]). Pathological conditions correspond to a value of dimensionless macroscopic adhesion energy greater than 75.0. Figure 4.14 shows that $[\eta]$ increases monotonically with $\bar{\varepsilon}_{adh}$, except for the case of Fig. 4.14d with $\lambda = 10$ which has been discussed in Fig. 4.13d where we have seen an inversion of normalized viscosity behavior as a function of the dimensionless macroscopic adhesion energy. Note also that the range of variation of normalized viscosity can be ample enough (it can attain a factor of two ; see Fig. 4.14a .Figure. 4.14b shows that (for $\lambda = 10$) the normalized viscosity exhibits two jumps, one at about $\bar{\varepsilon}_{adh} = 12$, which is due to a sudden transition from S to FA when the adhesion energy increases, and a second jump at $\bar{\varepsilon}_{adh} = 57$, due to a transition from FA to R. The plateau shown in Figure. 4.14b (triangles) correspond to FA regime where the doublet configuration remains the same upon increasing adhesion energy.

In summary, the present section shows that the rheological behavior of the doublet shows a shear-thinning. We also showed that, in almost all cases the normalized viscosity of doublet increases with the adhesion. The rheological signature of blood may be considered as an alternative reliable diagnosis and adhesion measurement. In the next section we will investigate on the effect of adhesion on the ATP transport.

4.3.4 Effect of adhesion on ATP release

RBCs are not just cargos of oxygen, but they also transport other molecules and nutriments like ATP (Adenosine triphosphate). Here, we focus on the effect of adhesion between RBCs on ATP release by RBCs.

To date, several in-vitro experiments focused on the ATP release pathways. The mechanosensitive channel called Pannexin 1 hemichannel (px1) is believed to be the main candidate of ATP release. It is sensitive to the mechanical stress. In addition of px1, the cystic fibrosis transmembrane conductance regulator (CFTR) behaves like a regulator of ATP release. Based on this two scenarios, aperture of the px1 due to the shear stress and the up-regulating by the CFTR due to the RBCs deformation, Zhang et al [Zhang et al., 2018b] proposed a theoretical model. Their simulations showed a good agreement with in-vitro experiments [Forsyth et al., 2011]. This section is dedicated to very preliminary results about the effect of adhesion between RBCs on ATP release. This work is carried out in collaboration with my colleague Zhe Gou (postdoc). Firstly, we reproduced a phase diagram as shown in Fig. 4.3-a. In addition

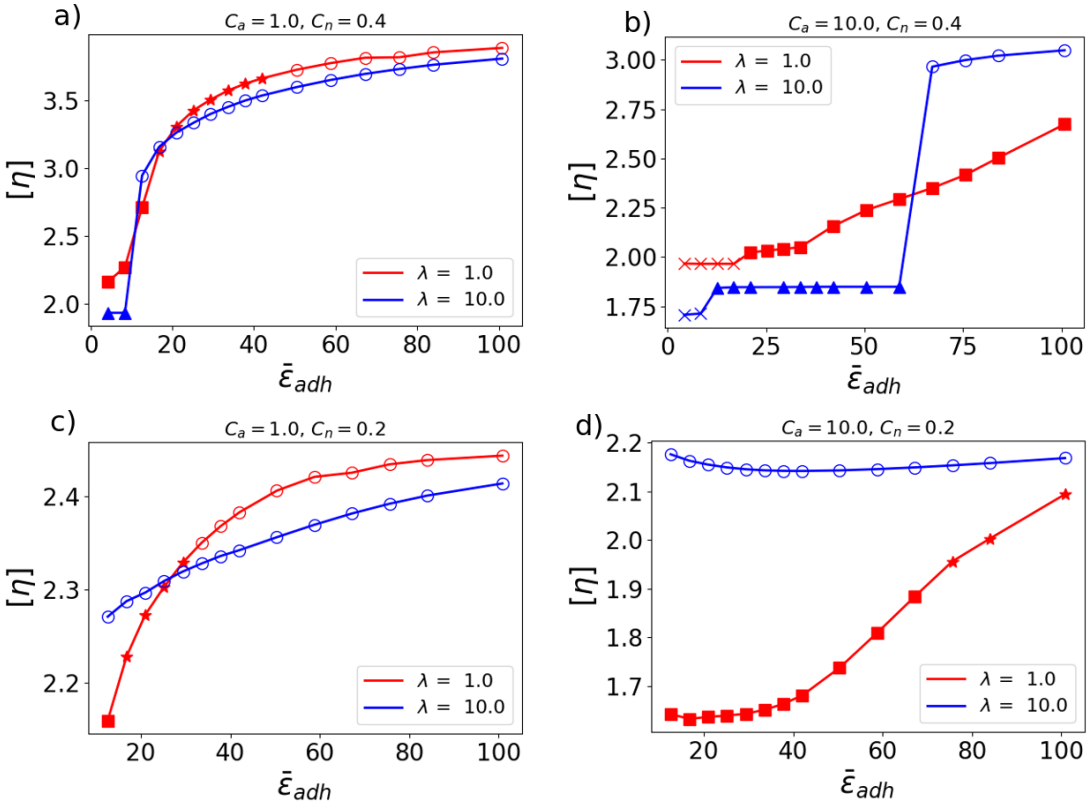

FIGURE 4.14 : The normalized viscosity $[\eta]$ as a function of the dimensionless macroscopic adhesion energy $\bar{\varepsilon}_{adh}$ for different values of viscosity contrast and confinement. The simulation data are shown as dots. (a) $C_a = 1.0$ and $C_n = 0.4$, (b) $C_a = 100.0$ and $C_n = 0.4$, (c) $C_a = 1.0$ and $C_n = 0.2$, (d) $C_a = 100.0$ and $C_n = 0.2$. Circle symbol represents the rolling phase, star : flexible rolling, square : rolling + sliding, triangle : flow alignment, cross : separation.

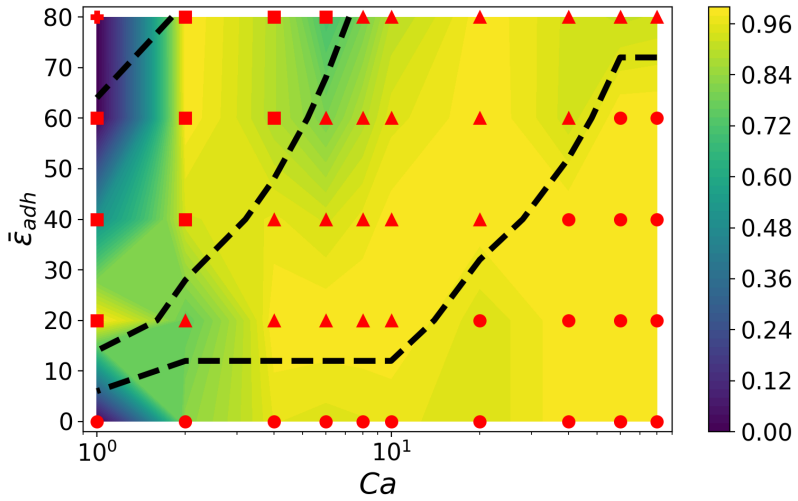

FIGURE 4.15 : Phase diagrams showing the different behaviors of doublet in the parameter space of the capillary number and the dimensionless macroscopic adhesion energy. Plus symbol represents the rolling phase, square : flexible rolling, triangle : rolling + sliding, circle : separation. The map color shows the ATP release by doublet

of the dynamics exhibited by the doublet, we also present the total ATP release level (using a color code) averaged over time and normalized by the maximum ATP release level at the same capillary number C_a. Figure. 4.15 shows that at low capillary number the ATP release level is non-monotonic with dimensionless adhesion energy $\bar{\epsilon}_{adh}$ for a fixed C_a. Indeed, the ATP release level increases and then decreases, the maximum release is found when the doublet exhibit rolling+sliding. The non-monotonic behavior is due to the increase of the shear stress when the cells slid on each other as shown in Fig. 4.16 ($C_a = 6$, $\bar{\epsilon}_{adh} = 80$). At high capillary number $Ca > 40$ the ATP release level decreases with $\bar{\epsilon}_{adh}$ for a fixed C_a. For a fixed C_a, passing from rolling+sliding to flexible rolling, the ATP release level decreases. When the doublet undergo flexible rolling the interface between the membrane of two cells sense a small shear stress (due to a weak relative motion between the two cells). This means that both px1 and CFTR are disactivated in this regime, leading to the decrease of ATP release level. The CFTR activation is more pronounced at high enough capillary number. Figure. 4.16 shows that CFTR is activated when $C_a = 80$.

To sum up this section. Under the physiological condition, the aggregation is reversible. The aggregation and disaggregation between the erythrocytes enhances the ATP release due to the sliding between the cells which increases the shear stress on the membrane. In contrast, when adhesion is strong, the erythrocyte doublet becomes robust, decreasing significantly the shear stress on the membrane, due tp

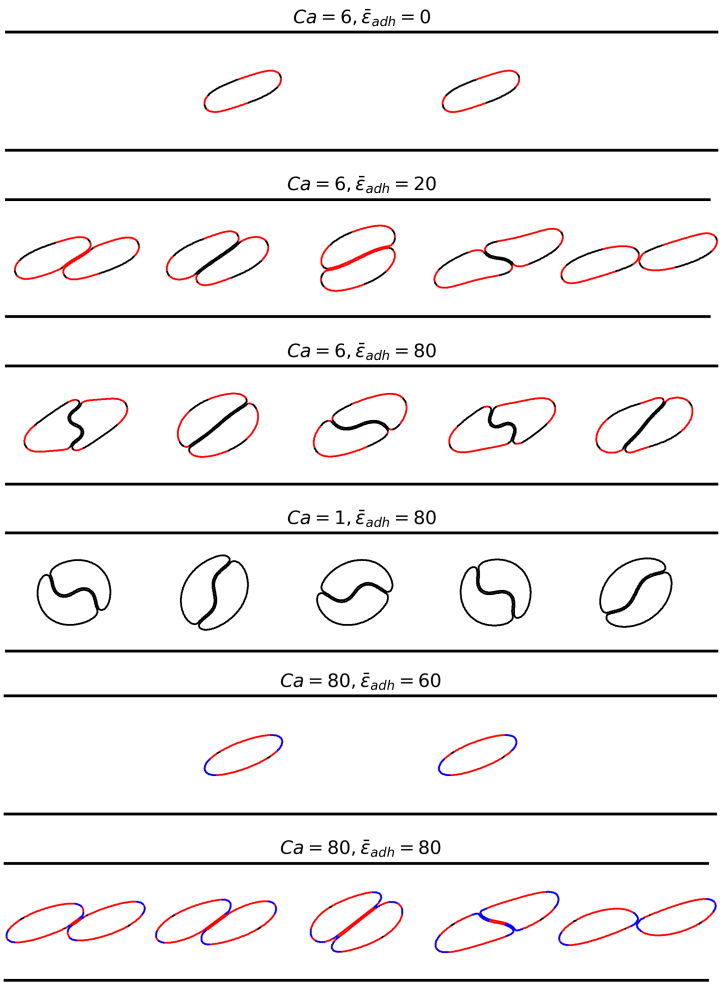

FIGURE 4.16 : Snapshot showing the dynamics of vesicle doublet for different capillary number and adhesion energy. The red color refers to Px1 channel activation. The blue color refers to Px1 and CFTR channels activation. The black color refers to no activation

weak relative motion that disactivate px1 and CFTR. It is therefore interesting to see that aggregation does not only impact (in a negative sense) oxygen delivery but also ATP release.

4.3.5 Effect of spectrin network elasticity on the aggregation and disaggregation of doublet

In the present section, we present 3D simulations result to investigate the cytoskeleton effect on the doublet separation, and to check the robustness of our 2D simulations. Here, we present phase diagrams that show the existence of almost the phases found in 2D. As in 2D, in 3D we will see that membrane tank-treading of RBC enhances the doublet dissociation. For a single RBC the possibility of membrane tank-treading depends on capillary number, defined by $C_s = \eta \dot{R}_0 \gamma / \mu$, where we recall that μ is the cytoskeleton shear modulus (typically $\mu \simeq 4\mu N/m$). For low enough C_s tumbling prevails whereas membrane tank-treading takes over at high C_s [Yazdani and Bagchi, 2011, Fischer and Korzeniewski, 2013b]. Taking for η the value of water viscosity (which is close to the plasma one) and $R_0 \sim 3\ \mu m$, we obtain $C_s \sim 10^{-3}\dot{\gamma}$ (with $\dot{\gamma}$ in unit of s^{-1}). For healthy RBCs the transition between tumbling and tank-treading takes place at about $C_s \sim 0.1$ [Yazdani and Bagchi, 2011, Fischer and Korzeniewski, 2013b].

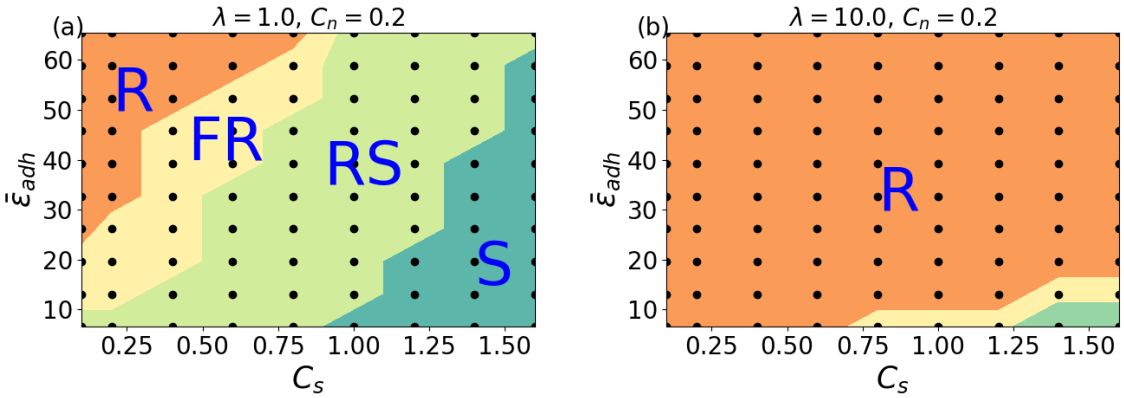

FIGURE 4.17 : Phase diagrams showing the different behaviors of doublet in the parameter space of the capillary number and the dimensionless macroscopic adhesion energy. The simulation data are shown as dots. The confinement is $C_n = 0.2$ (a) $\lambda = 1.0$, (b) $\lambda = 10.0$.

In this section, we evaluate the effect of the single RBC dynamics (TT or TB) on the aggregation and dis-aggregation of RBCs doublet aggregates. For that purpose,

two values of confinement ($C_n = 0.2, 0.4$) and viscosity contrast ($\lambda = 1.0, 10.0$) are explored. The values of confinement and viscosity contrast are chosen in order to have tank-treading (TT) and the tumbling (TB) motions, and to analyze the effect of single cell dynamics on the aggregation and dissociation of RBCs doublet. Table 4.2 shows the dynamics exhibited by a single RBC at different values of confinement, viscosity contrast and capillary number.

		C_s						
		0.1	0.4	0.8	1.0	1.2	1.4	1.6
$C_n = 0.2$	$\lambda = 1.0$	TB	TB	TT	TT	TT	TT	TT
	$\lambda = 10.0$	TB	TB	TB	TB	TB	TB	TB
$C_n = 0.4$	$\lambda = 1.0$	TB	TT	TT	TT	TT	TT	TT
	$\lambda = 10.0$	TB	TB	TB	TB	TB	TB	TB

TABLE 4.2 : Table showing single RBCs dynamics for different values of capillary number, confinement and viscosity contrast. TT : Tank-treading. TB : Tumbling.

Subsequently, we analyze the RBCs doublet configuration in wide range of capillary numbers (applied shear rates) and the adhesion energy which is related to the fibrongen level in blood.

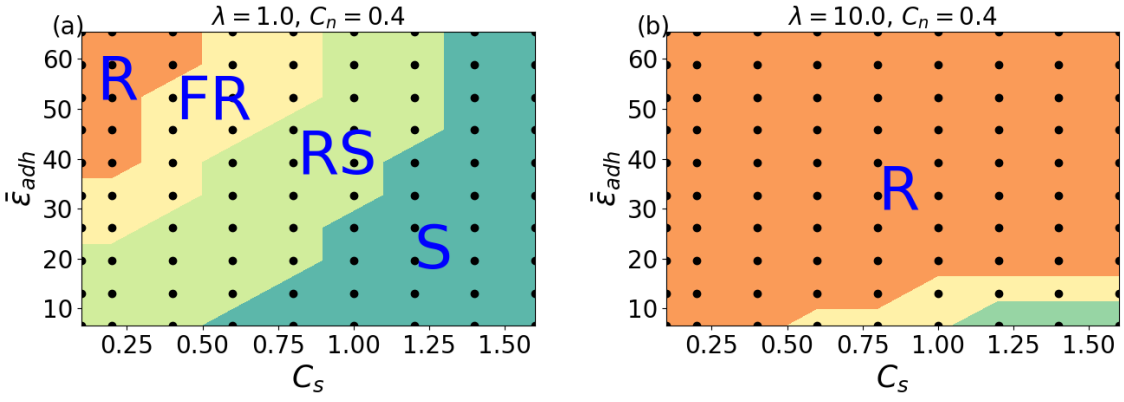

FIGURE 4.18 : Phase diagrams showing the different behaviors of doublet in the parameter space of the capillary number and the dimensionless macroscopic adhesion energy. The simulation data are shown as dots. The confinement is $C_n = 0.4$ (a) $\lambda = 1.0$, (b) $\lambda = 10.0$.

Figure 4.17 (left panel) shows phase diagram at low confinement. Three regimes have been found in the case of $\lambda = 1.0$, i) rolling (R) : the two RBCs remains attached with constant contact area and flip like a coin (as tumbling of single RBCs). The R

regime takes place at low capillary number and at high adhesion energy (the aggregation force is dominant in this regime). ii) flexible rolling (FR) : in this regime the doublet exhibits the same dynamics as rolling, but the contact area transits between flat and sigmoid shape during time. iii) rolling sliding (RS) the doublet tumbles and the cells slide on each other. In this regime there is a competition between the aggregation force and the dis-aggregation force due to the shear stress. At high shear rate, the separation between the RBCs takes place. This indicates that the dis-aggregation force due to the flow is strong enough to overcome the aggregation force. Figure 4.19 shows snapshots of the dynamics discussed in this paragraph.

Let us now study the effect of the lack of tank-treading on the phase diagram. In table 4.2, it is seen that a high enough value of the viscosity contrast ($\lambda = 10.0$) favors tumbling. Mauer et al. [Mauer et al., 2018] showed by means of numerical simulations and in-vitro experiments that the tank-treading regime is suppressed at high enough viscosity contrast value. We have analyzed the phase diagram of doublets in the capillary number and adhesion energy plane. Due to the absence of TT, the doublet phase diagram is quite different , as shown in Figure 4.17 (right panel). We observe a dramatic shrinkage of the separation phase as compared to the case where TT takes place (Figure 4.17, left panel). Thus, as concluded in 2D, the absence of TT strongly enhances the robustness of doublet. Interestingly, the 2D (Figure 4.3) and 3D (Fig 4.18) phase diagrams show a striking similarity. This further supports the idea that 2D simulations are quite precious (due to computational efficiency) in order to explore several major facts before resorting to 3D. simulations.

Figure 4.19 shows the snapshot of doublet dynamics corresponding to $\lambda = 1$ (phase digaram in Figure 4.17, left panel). In this situation TT prevails showing the four configurations (R, FR, RS and S), where at hight shear rate the doublet dissociates. Figure 4.20 shows the snapshot of doublet dynamics corresponding to $\lambda = 10$ (phase digaram in Figure 4.17, right panel). In this case TB prevails and we see that the region of separation has collapsed meaning that even for a moderate adhesion (within physiological values) the doublet is very robust and can. not be dissociated. The more we increase the shear rate the more adaptation of doublet shape is observed. This shape adaptation, already discussed for 2D simulations, is a way for doublet to escape dissociation.

As a final remark, it is important to note that the RBC doublet dynamics are mainly governed by the interplay between the bending energy and the adhesion energy. The membrane shear elasticity due to the cytoskeleton only affect quantitatively the

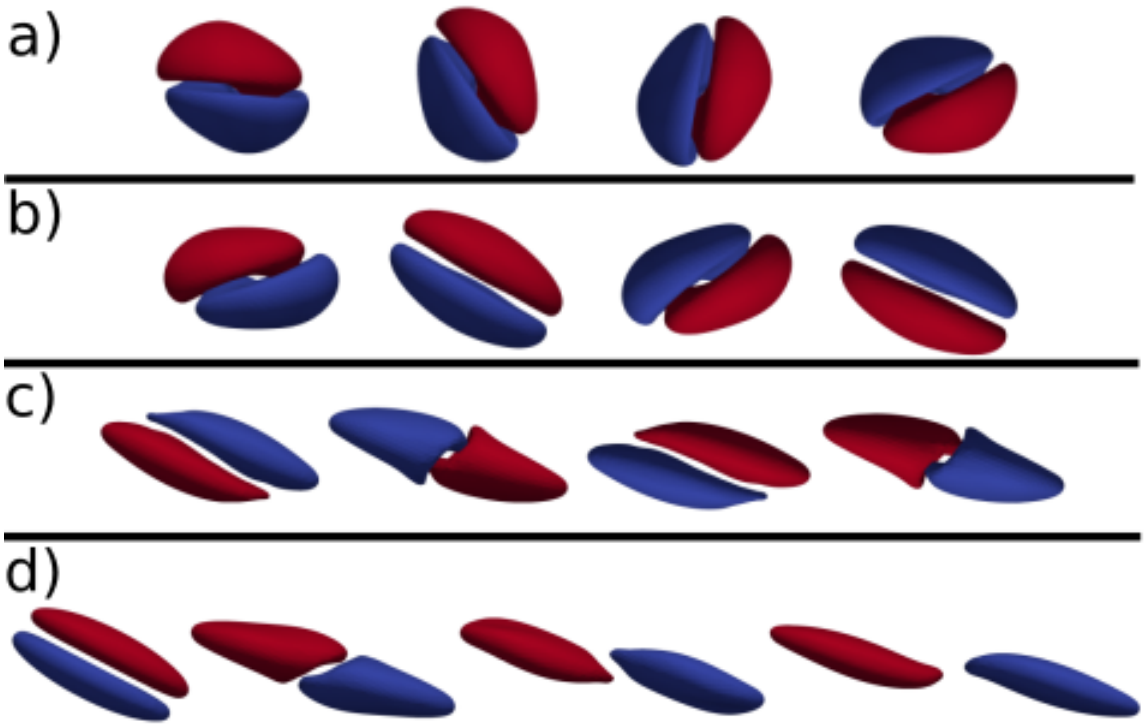

FIGURE 4.19 : Snapshots showing the dynamics of a RBCs doublet for different capillary number C_s and dimensionless macroscopic adhesion energy $\bar{\epsilon}_{adh}$. Here $\lambda = 1.0$ and $C_n = 0.4$. a) $C_s = 0.25$ and $\bar{\epsilon}_{adh} = 60.0$, b) $C_s = 0.50$ and $\bar{\epsilon}_{adh} = 50.0$, c) $C_s = 0.75$ and $\bar{\epsilon}_{adh} = 30.0$, d) $C_s = 1.25$ and $\bar{\epsilon}_{adh} = 20.0$. The snapshots are taken over one period of the doublet dynamic.

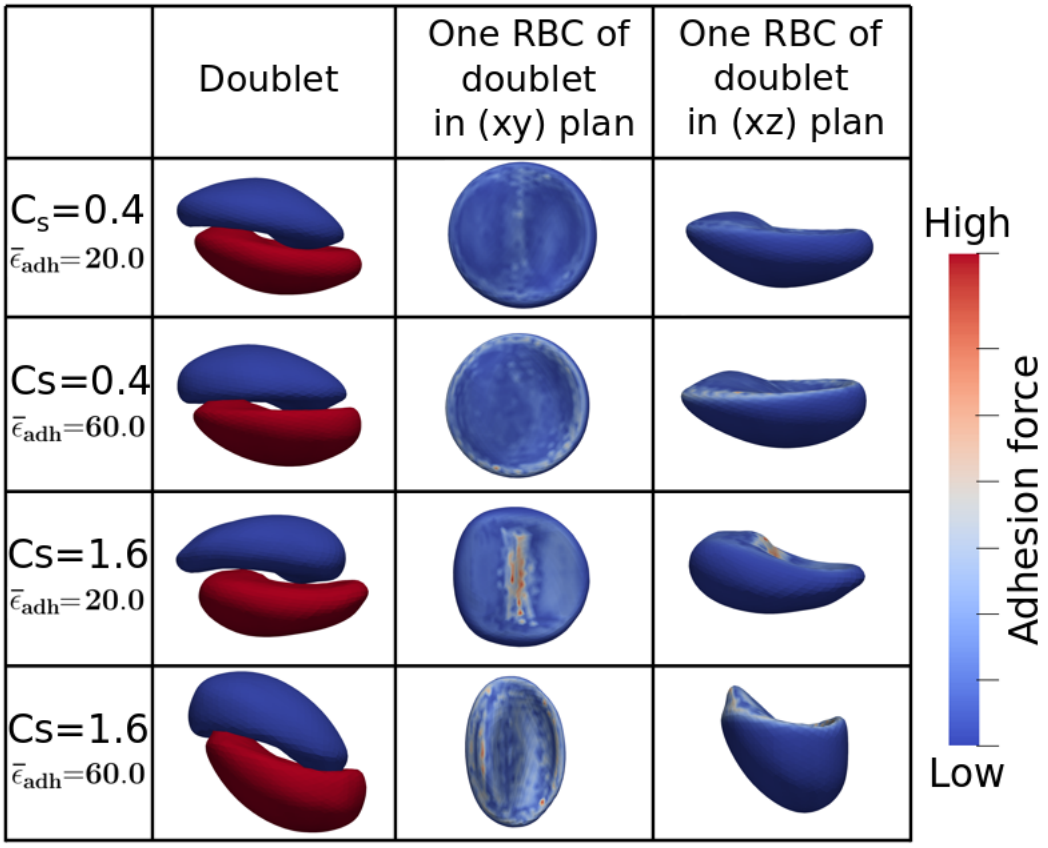

FIGURE 4.20 : Snapshots showing the dynamics of a RBCs doublet for different capillary number C_s and dimensionless macroscopic adhesion energy $\bar{\epsilon}_{adh}$. Here $\lambda = 10.0$ and $C_n = 0.2$. The map color shows the adhesion force. We clearly see shape adaptation and adhesion force distribution on the interface as C_s and $\bar{\epsilon}_{adh}$ increase.

results. Hoore et al. [Hoore et al., 2018] showed that the RBC doublet under static conditions exhibit various phases, namely, the malefemale, sigmoid–biconcave, Yin–Yang, sheath, flat–concave, and flat–biconcave as shown in figure 4.21. The authors [Hoore et al., 2018] claim that those phases are chiefly controlled by the bending energy and adhesion energy. Our finding under flow confirm this idea.

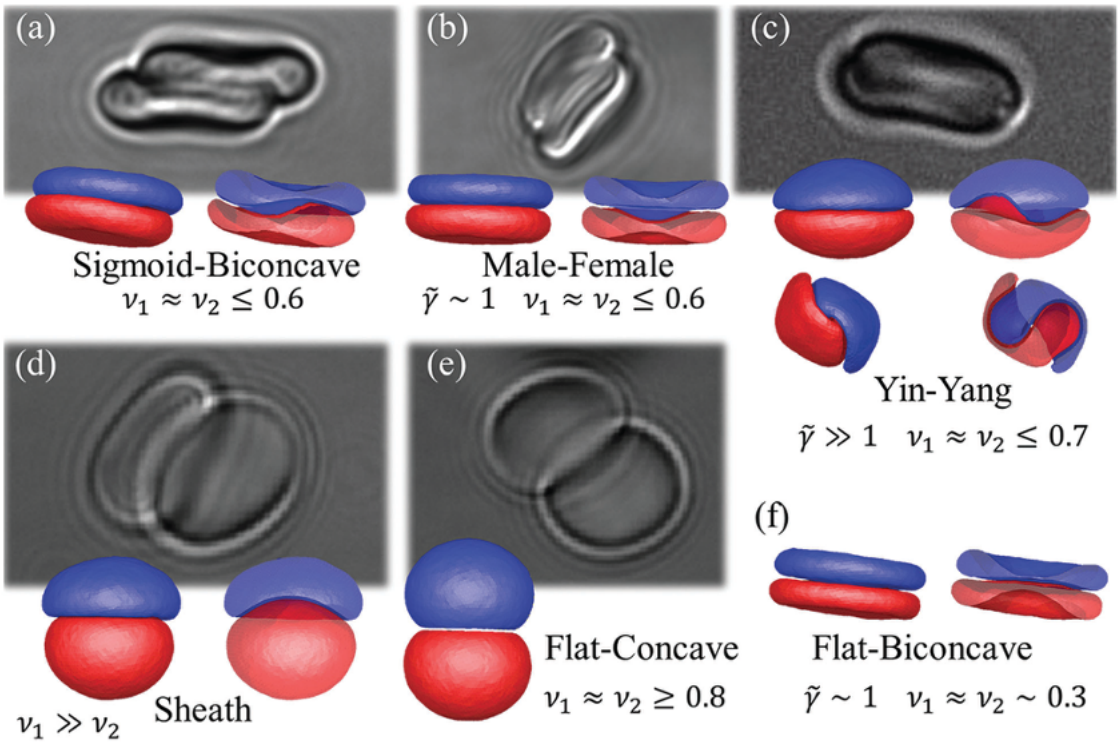

FIGURE 4.21 : Comparison of experimental and simulated RBC doublet shapes determined by the adhesion strength, bending modulus, and the reduced volume of RBCs. For simulations, the side and section views are presented for each case. The phases (a) sigmoid–biconcave, (b) male–female, (c) sigmoid–concave (Yin–Yang), (d) sheath, (e) flat–concave, and (f) flat–biconcave are shown. The sheath, F–C, and F–B phases are not probable for RBC doublets under physiological conditions [Hoore et al., 2018]. $\tilde{\gamma}$ represents the reduced adhesion energy, ν_1 and ν_2 represent the reduced volume of the first and the second RBC of the doublet.

4.4 Summary and concluding remarks

To summarize, in this chapter we employed a boundary integral method and Lattice Boltzmann method to investigate dynamics, rheology and ATP release of doublet under flow. We varied the dimensionless macroscopic adhesion energy in this study

from 5.0 to 105.0, a range which corresponds to physiological and pathological conditions. We found that the doublet can exhibit rolling, flexible rolling, rolling+sliding, flow alignement and separation, depending on several parameters (capillary number, adhesion energy and viscosity contrast). A remarkable feature is that when each single cell exhibits tumbling (for example due to a high enough internal viscosity), the doublet becomes quite stable even for an extremely large shear stress (the separation region is almost absent in the phase diagram, Fig.4.11). Indeed, the doublet adapts its spatial configuration to the applied flow in a way to escape dissociation. In vivo RBC membrane may perform tank-treading in arterioles only. Furthermore, several RBCs pathologies are associated with increased membrane rigidity or cytosol viscosity. This may result in a collapse of the membrane tank-treading ability (even in arterioles) causing a stability of doublets (and probably of larger aggregates), and impairing blood perfusion in microcirculation. Another important observation is that there are two stable configurations of the doublet at high enough adhesion. These two states have quantitatively different dynamical signatures under shear flow. Lowering the adhesion strength results in a loss of one of the configurations. This bifurcation marks the transition from rolling to flexible rolling dynamics, due to the presence of a saddle node point (turning point of the imperfect bifurcation).

The rheological study revealed shear thinning, and a quite significant increase of viscosity with adhesion energy. This increase with energy is *a priori* expected, since the doublet becomes more and more robust, and its higher cross section opposes more flow resistance. Rheology may be an interesting alternative for a systematic blood diagnosis and estimate of adhesion energy. The aggregation and disaggregation process may improve, or preclude, ATP release from RBC doublet. In the flexible-rolling regime, for example, the wak sliding between cells is associated with a decrease of stress, and thus of lower ATP release. In contrast, in the sliding-rolling regime the sliding between the RBC enhances the shear stress on the membrane, leading to a higher ATP release. A systematic numerical study in 3D including cytoskeleton is carried out in order to draw practical conclusions on the role of RBCs components on the aggregation and dissociation of aggregates. Results presented in section 4.3.5 show a good agreement between 2D and 3D simulations. Finally, the doublet dynamics are found to be mainly controlled by the membrane bending and adhesion energy, whereas cytoskeletton plays a secondary role. The fact that phase diagrams in 2D and 3D are quite similar is a further corroboration of this statement, since in 2D the notion of cytoskeletton is absent.

Chapitre 5

Red blood cells aggregates transport for finite concentration

In the last chapter we have seen that robust aggregation between two RBCs can take place, and especially when tank-treading is inhibited. That chapter dealt with doublets dynamics, in order to understand the basic relevant parameters that contribute to aggregation. In real situations hematocrit is large (up to 45 %, or even more like in polycythemia disease). In addition, vascular networks are complex and the impact of geometry is not yet clear. This chapter focuses on aggregation properties (and their impact on flow properties) for different hematocrits. One important fact discovered here, that should be highlighted is the non monotonic character of the blood flow flux as a function of adhesion energy : at low adhesion energy the flux is enhanced in comparisons to the situation without adhesion until a critical adhesion where the flux attains a maximum, before declining at high adhesion.

5.1 Introduction

In addition to oxygen transport, blood has many important vital tasks, such as temperature regulation, removal of waste, immunological functions, coagulation (a response to a broken blood vessel) and supply of nutrients. Several of these functions, are linked directly to RBCs flux and blood viscosity. The flux of rigid or soft particles (droplets, vesicles, capsules...) is a complex function of the particle concentration, depending strongly on the suspension structure induced by interactions with walls and among particles. The optimality in blood flow is an interesting problem in hemorheology. Hematocrite is likely to be optimized due to its effect on nutriments transport. The problem of optimal hematocrit has been the subject of many studies [Lipowsky et al., 1980,Barbee and Cokelet, 1971,Birchard, 1997,Hedrick et al., 1986,Linderkamp et al.,

1992]. Recently, it has been shown that the RBCs transport depends strongly on the RBCs properties, the vessel diameter and the flow strength [Farutin et al., 2018]. Gou et al [Gou et al., 2021] hhave shown that the quantity of the ATP released by RBCs suspensions depends strongly on the hematocrit, the ATP released per cell increases to a maximum which corresponds to an optimal physiological hematocrit. Optimality in living systems is a delicate question that must be approached with care. In [Farutin et al., 2018, Gou et al., 2021], the authors found that the flux of vesicles (a model of RBCs) and ATP release by vesicles both show an optimal value with the RBCs concentration. In this chapter we will analyze the aggregation of RBCs in different regimes. Instead of analyzing the statistics of RBCs clusters, it seemed to us more appropriate to analyze a feature that informs us on the perfusion properties affected by adhesion, which constitutes a more direct indicator. For this reason we will analyze the RBCs flux and viscosity as functions of the adhesion energy $\bar{\epsilon}_{adh}$ and the capillary number C_a. It is found that the RBCs flux increases with the adhesion energy to a maximum and then decreases. We will provide an explanation to the non-monotonic behavior of the RBCs flux with the adhesion energy.

5.2 Method and parameters

5.2.1 Method and numerical procedure

In this chapter, we will employ Lattice Boltzmann method coupled with immersed boundary method, which is a more efficient method (as compared to boundary integral method) for high concentrated suspension and complex geometry. The employed method and the model system (vesicles) have been described in [Shen et al., 2017]. Initially, the cells are distributed randomly inside the channel, and then a parabolic flow (Poisseuille flow) Eq.5.1 is applied to the suspension as shown in Fig 5.4.

$$\left\{ \begin{array}{l} u_x^0 = 4u_m y(W-y)/W^2 \\ u_y^0 = 0 \end{array} \right\} \tag{5.1}$$

where u_m is the maximal velocity, W is the channel width.

The quantities of interest are averaged over time once the simulation reaches the steady state. The RBCs flux is represented by means of the cell flow rate Q_c normalized by the flow rate of the cell-free fluid Q_0 under the same flow strength. The cell flow rate is measured by counting the number of cells passing throw a section in the channel during a fixed time interval. The effective viscosity is defined as :

$$\eta_{eff} P_c = \eta_0 P_0 \tag{5.2}$$

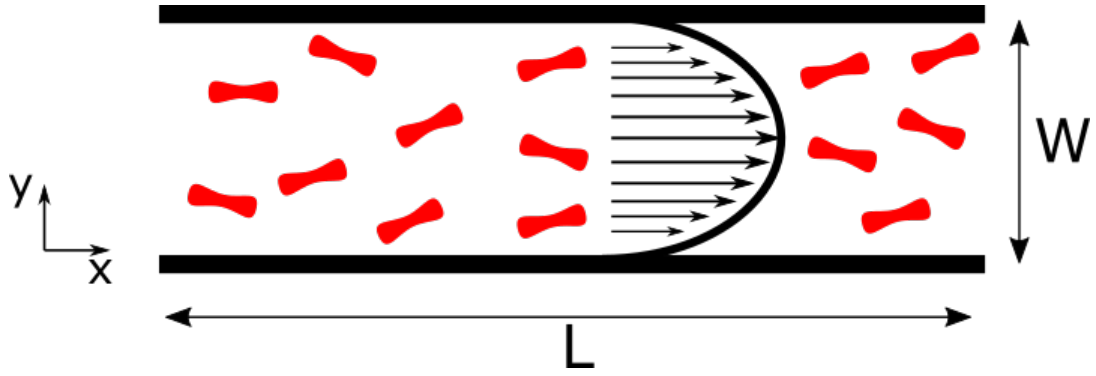

FIGURE 5.1 : Schematic of the simulation.

Where P_c and P_0 are the average flux of the suspension (not to be confused by cells flux, Q_c) and the flux of the pure fluid (with viscosity η_0) respectively. The normalized viscosity can be expressed as follow :

$$[\eta] = \frac{\eta_{eff} - \eta_0}{\eta_0 \phi} \tag{5.3}$$

where $\phi_t = n\pi R_0^2/(LW)$ represents concentration of the cell suspension, n the number of the cells in the suspension. All the quantities calculated in this chapter are averaged over time in the steady state.

5.2.2 Dimensional numbers

Dimensionless numbers are used to describe the vesicle and the flow characteristics :

- The capillary number : allows to quantify the flow strength over bending rigidity of the membrane
$$C_a = \frac{\eta_0 < \dot{\gamma} > R_0^3}{k} \equiv \dot{\gamma}\tau_c \tag{5.4}$$
$< \dot{\gamma} >= 2u_m/W$ is the averaged shear rate along the y direction and k is the bending rigidity modulus.

- The viscosity contrast : the ratio between the viscosities of the internal and external fluids
$$\lambda = \frac{\eta_1}{\eta_0} \tag{5.5}$$

- The reduced area : combining the vesicle perimeter L and its enclosed area A
$$\tau = \frac{(A/\pi)}{(L/2\pi)^2} \tag{5.6}$$

Throughout this chapter, the reduced area value will be set to 0.65 (inspired by that of human RBCs). The viscosity contrast is fixed at 1.0

5.3 Results and discussion

In chapter 4, we showed that at high enough viscosity contrast ($\lambda = 10.0$) the erythrocyte-erythrocyte doublet becomes quite stable even for high enough applied shear stress. In this part we will discuss some features of the aggregation of RBCs for different regimes of viscosity contrast. Then our main goal is to evaluate the effect of aggregation on the RBCs flux, the suspension viscosity and ATP release from RBCs.

5.3.1 Reversible and irreversible aggregation of RBCs

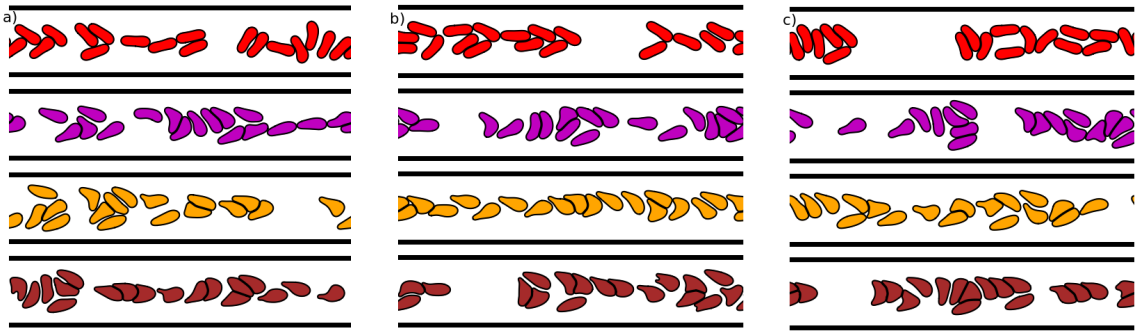

FIGURE 5.2 : Snapshots showing the spatial configurations of the cells at different time steps. a) $1500\tau_c$, b) $1750\tau_c$ and c) $2000\tau_c$. Here the capillary number is set to $C_a = 25.0$, the cells concentration is $\phi = 0.2$ and the viscosity contrast is set to $\lambda = 1.0$. The colors show different macroscopic dimensionless adhesion energy values. Red : 36.81, purple : 73.63, yellow : 147.27 and brown : 220.91

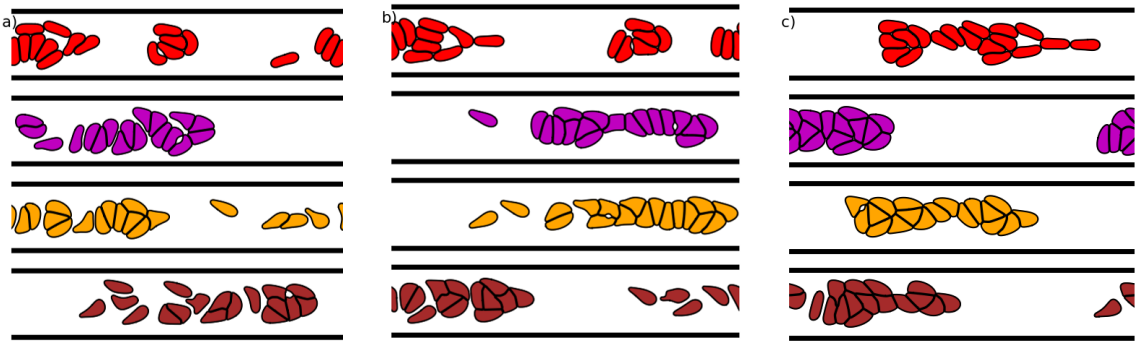

FIGURE 5.3 : Snapshots showing the spatial configurations of the cells at different time steps. a) $1500\tau_c$, b) $1750\tau_c$ and c) $2000\tau_c$. Here the capillary number is set to $C_a = 25.0$, the cells concentration is $\phi = 0.2$ and the viscosity contrast is set to $\lambda = 10.0$. The colors shows different macroscopic adhesion energy values. Red : 36.81, purple : 73.63, yellow : 147.27 and brown : 220.91. The last panel corresponds to a pathological adhesion energy ; see table 4.1.

Under physiological conditions, the aggregation process is believed to be reversible. In contrast, under pathological conditions the aggregation may become irreversible. In chapter 4, we found that the RBCs doublet aggregates are stable even for physiological condition of adhesion energy and even for high enough applied shear stress. The non dissociation is due to the high viscosity contrast of RBCs (as explained in chapter 4), as expected to occur for some diseases (e.g. malaria). Here we show that the non dissociation of cells also occurs for RBCs suspension under Poiseuille flow. In figure 5.4, we see that for low enough viscosity contrast the cells form aggregates in a reversible way as long as the adhesion energy remains within the physiological range : they continuously adhere to each other and they dissociate during time. The snapshots of reversible aggregation are shown in figure 5.4 with red, violet and orange color. When the adhesion energy is high enough (above physiological values) the aggregation becomes irreversible (see figure 5.4, burgundy color). The relation between dimensionless adhesion energy and fibrinogen concentration is given in table 4.1, showing both physiological and pathological adhesion.

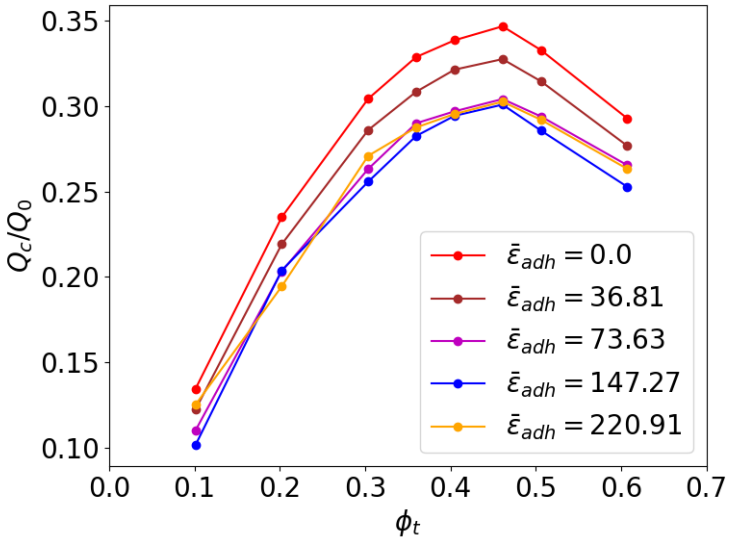

FIGURE 5.4 : Normalized cell flow rate as a function of volume fraction of cell for different dimensionless macroscopic adhesion energy. The simulation data are shown as dots. Here the viscosity contrast is $\lambda = 10.0$ and the capillary number is $C_a = 25.0$

In contrast with the case of low viscosity contrast discussed above, for high viscosity contrast, we observe that once the aggregates form they remain quite stable ; they may never dissociate, as shown in figure 5.3, even for low adhesion energy values (within physiological range). This is due to the robustness of RBC aggregation, due to absence of tank-treading, as analyzed in detail in chapter 4.

In Fig 5.4, we show the normalized cell flow rate as function of volume fraction of cell for different dimensionless adhesion energy. We clearly see that the irreversibility of aggregation due to high value of viscosity contrast ($\lambda = 10.0$) has a dramatic effect on RBCs transport. As we will explain in the next subsection 5.3.2, in the absence of adhesion the cell transport increases to a maximum and then decreases. The formation of robust aggregates affects strongly the RBC transport.

We will first focus on the viscosity value $\lambda = 1.0$, which is the regime where reversible aggregation occurs (if adhesion energy is not too high) and we will investigate the effect of the adhesion energy on the RBCs transport, RBCs suspension viscosity and the ATP released from RBCs. We will briefly discuss the case of large viscosity contrast $\lambda = 10$, where aggregation becomes irreversible.

5.3.2 The effect of adhesion energy on the normalized cell flux

Here, we investigate the effect of the adhesion energy on the RBC flux for different capillary numbers. Figure 5.5 summarizes the results. In the absence of adhesion, where $\bar{\epsilon}_{adh} = 0.0$ (the relation between dimensionless adhesion energy and fibrinogen concentration is given in table 4.1), our results are in a good quantitative agreement with simulation results of Farutin et al. [Farutin et al., 2018]. The normalized cell flux Q_c/Q_0 exhibits a maximum as a function of the cell concentration for different capillary numbers. It is reported [Farutin et al., 2018] that the optimal hematocrit is sensitive to the capillary number, vessel diameter, reduced area. The optimal hematocrit values found [Farutin et al., 2018] for vessel sizes corresponding to macrocirculation and intermediate microcirculation (arterioles) are close enough to the corresponding physiologically values.

Now, we focus on the effect of adhesion between cells (formation of aggregates) on the cell flux and optimal hematocrit. The channel width value is fixed at $22.5\mu m$ (a typical value in microcirculation). The simulations are performed for different values of capillary numbers. In Fig. 5.5, we see that including adhesion in our model does not affect qualitatively the shape of the flux : the existence of an optimal hematocrit for RBC transport is robust even in the presence of adhesion between RBCs. At very low capillary number C_a (where cell deformation is weak) the optimal hematocrit value is shifted towards high concentration values when the adhesion energy $\bar{\epsilon}_{adh}$ is increased. Surprisingly, we found that the maximal value of the normalized cell flux Q_c/Q_0 is not monotonic with the adhesion energy $\bar{\epsilon}_{adh}$. A low enough adhesion boosts RBCs flux. When adhesion energy is large enough the flux attains a maximum ; the

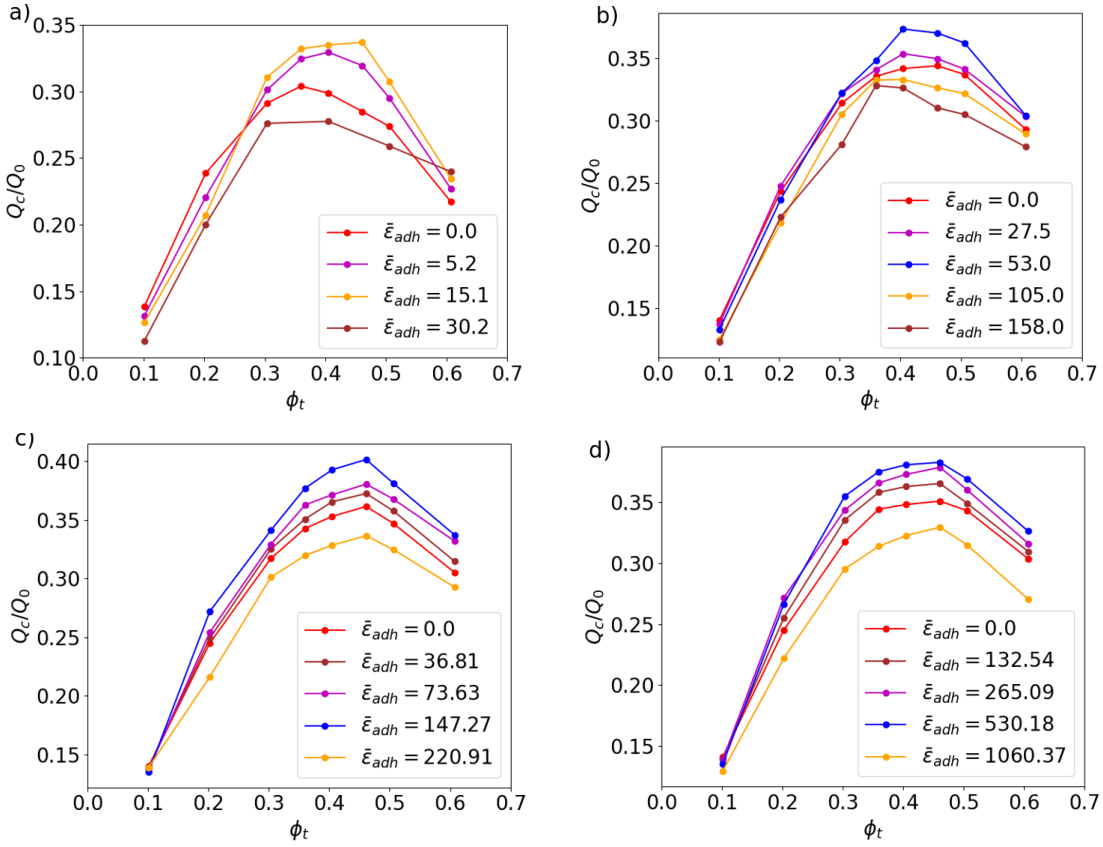

FIGURE 5.5 : Normalized cell flow rate as a function of volume fraction for channels with different dimensionless macroscopic adhesion energy. The simulation data are shown as dots. (a) $C_a = 0.9$, (b) $C_a = 9.0$, (c) $C_a = 25.0$, (d) $C_a = 90.0$.

corresponding adhesion energy is referred to "optimal energy". Beyond this value the maximum RBCs flux declines. The optimal adhesion energy value depends strongly on the capillary number as shown in Fig. 5.6. Under physiological conditions it is known that RBCs aggregates form and dissociate, as found here. The interesting fact obtained here is that adhesion (leading to reversible aggregates), if not too large, enhances the RBCs flux, meaning that this type of aggregates formation would be beneficial for perfusion, a quite counter-intuitive result (see explanation below). Note that the increase in maximum flux may be quite large, as shown in Fig. 5.6. For a zero adhesion, the smallest relative flux is about 0.3, and can attain, in the presence of adhesion, values up to 0.4 (for $\bar{\epsilon}_{adh} \sim 200$ and $Ca = 25$). This corresponds to an increase of the maximum RBCs flux by 30%, which is quite significant.

Let us now provide an intuitive explanation for the non monotonic behavior of of maximum flux with adhesion. At low adhesion some aggregates form, and they become larger and larger as adhesion increases. Figures 5.7 and 5.8 show typical configuration of RBCs for different hematocrits and adhesion energy. Consider for example the configurations in 5.8 on the left. In the absence of adhesion (red) the RBCs form a file. Between cells (see Fig .5.9) we have flow recirculations. Increasing adhesion (purple and blue) the cells start to form aggregates while remaining in the center. The cell-cell adhesion suppresses some recirculations (and thus dissipation), increasing thus efficiency of RBCs transport. When the adhesion energy increases further (yellow and brown) the aggregates become large enough so that they expend laterally to oppose enough resistance against the imposed flow. This leads to a decline in RBCs transport efficiency.

The fact that the optimal adhesion energy depends on capillary number has the following explanation. When Ca increases some aggregates are broken, and since there is a need to maintain some aggregate to destroy recirculation zones (and thus to enhance the flux) the adhesion energy has to be adapted (increased).

5.3.3 Concentration profile

Figure. 5.10 shows the concentration profiles of the suspension for different dimensionless adhesion energy values $\bar{\epsilon}_{adh}$. We see that in the absence of adhesion forces (red line in Figure. 5.10), the concentration profile of the suspension exhibits three pics. This is due to the competition between two antagonist effects : i) cell-cell hydrodynamic interactions, leading to what is known as shear-induced diffusion, pushing cells toward the walls, and ii) the wall-induced lift that pushes the cells towards the channel center. Increasing the adhesion energy in the physiological range (brown line

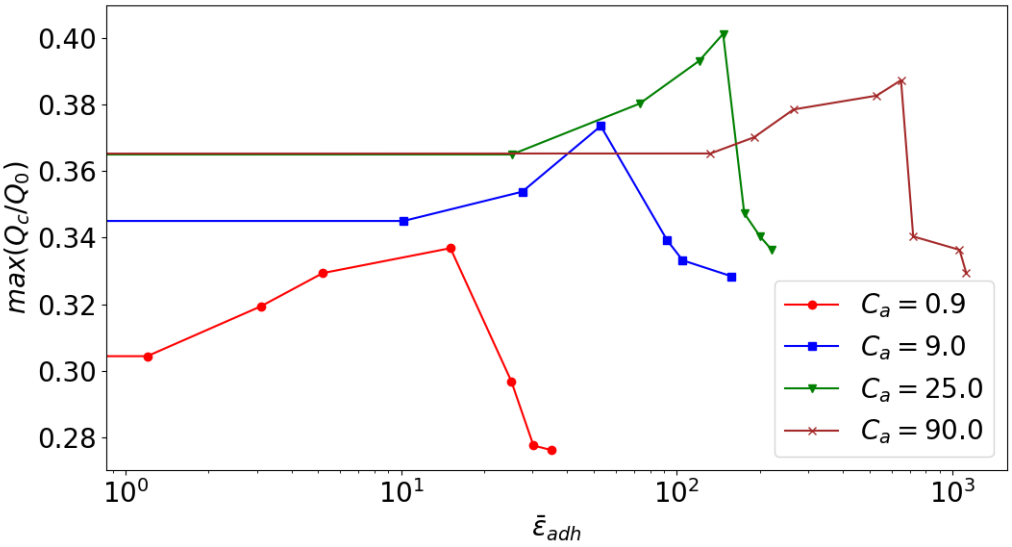

FIGURE 5.6 : The maximal value of the normalized flow rate as function of the dimensionless macroscopic adhesion energy for different values of capillary number. The horizontal axis is in logarithmic scale.

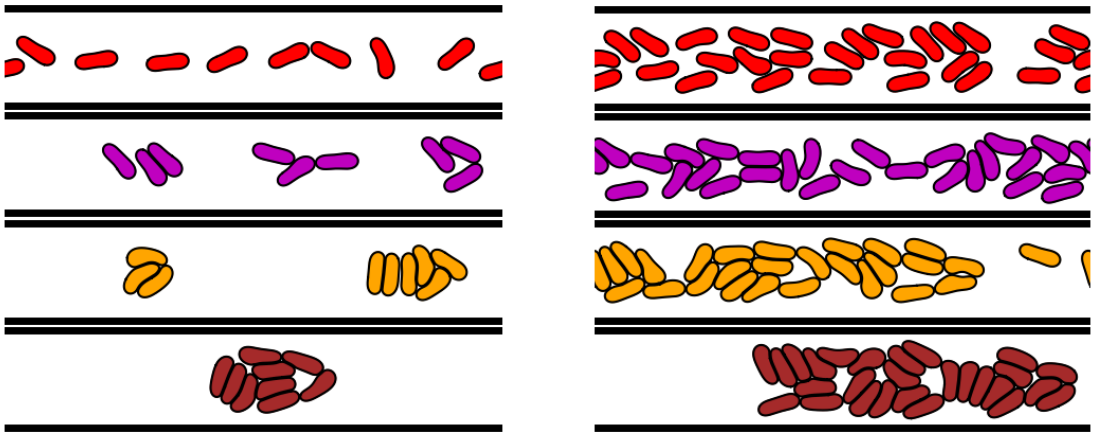

FIGURE 5.7 : Snapshots showing the spatial configurations of the cells for different macroscopic adhesion energy values. The colors show different macroscopic adhesion energy values. Red : 0.0, purple : 5.2, yellow : 15.1 and brown : 220.91. Here the capillary number is set to $C_a = 0.9$ and the viscosity contrast is set to $\lambda = 1.0$. Left : $\phi = 0.1$. Right : $\phi = 0.4$

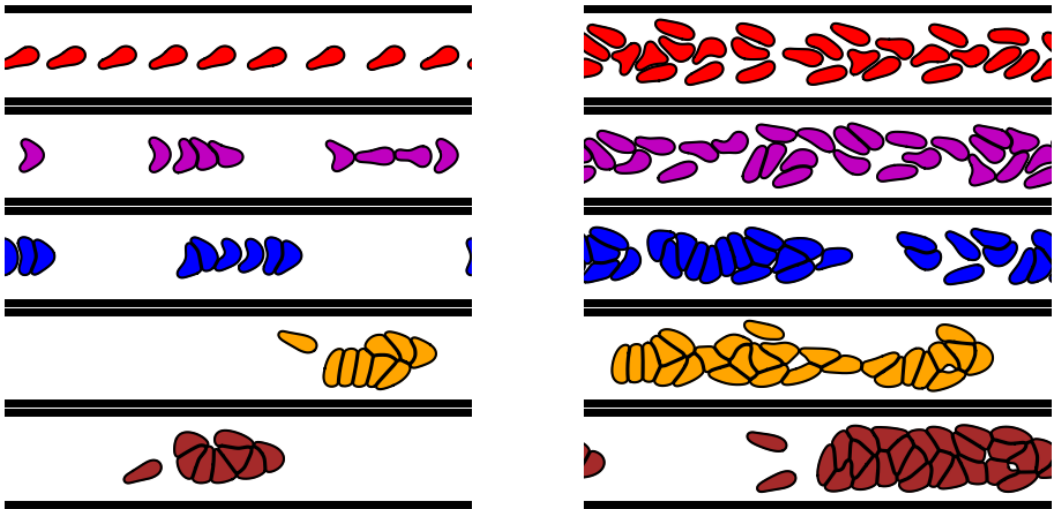

FIGURE 5.8 : Snapshots showing the spatial configurations of the cells for different macroscopic adhesion energy values. The colors show different macroscopic adhesion energy values. Red : 0.0, purple : 27.5, blue : 53.0 ,yellow : 105.0 and brown : 158.0. Here the capillary number is set to $C_a = 9.0$ and the viscosity contrast is set to $\lambda = 1.0$. Left : $\phi = 0.1$. Right : $\phi = 0.4$

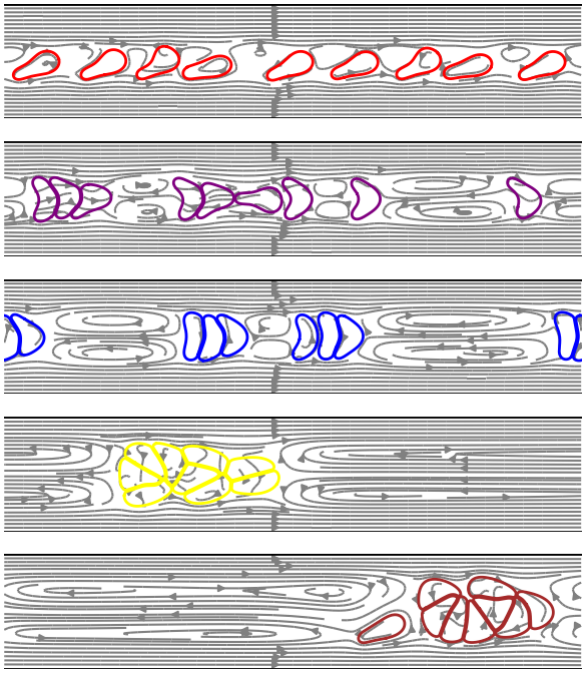

FIGURE 5.9 : Streamlines (grey lines with arrows) in a comoving frame. Snapshots showing the spatial configurations of the cells for different macroscopic adhesion energy values. The colors show different macroscopic adhesion energy values. Red : 0.0, purple : 27.5, blue : 53.0 ,yellow : 105.0 and brown : 158.0. Here the viscosity contrast is set to $\lambda = 1.0$, $\phi = 0.1\%$ and $C_a = 9.0$

in Figure. 5.10), the concentration profile is not affected considerably. In the physiological range of adhesion energy the hydrodynamic interaction between cells prevails since the aggregates form in a reversible way. At high enough adhesion energy (pathological case), large enough aggregates form (though they are still quite reversible, see snapshots in Fig.5.11). In this case the concentration profile is shown on Fig. 5.10 (blue line). Comparing the red line (without adhesion) and the blue one in Fig. 5.10 (with large enough adhesion) one sees that around centerline (say between $y = 5\mu$m and $y = 15\mu$m the integrated concentration is larger for the blue one than for the red one. In addition, from Fig. 5.12c (same parameters as in Fig. 5.10) the average speed in the channel are bigger for the blue line (with large enough adhesion ; this increase of speed is due to dissipation reduction) than for the red line (no adhesion). Together the increase of number of cells in the center and the average speed explain the increase of flux of RBCs. Increasing further and further adhesion leads to formation of large and irreversible aggregates occupying a larger and larger cross section, causing a relative blockage of the flow. The concentration profile (yellow line in Fig. 5.10) has lost peaks where the aggregate accumulate in thee center due to the collapse of hydrodynamics diffusion. At the same time the average speed is reduced (Fig. 5.12c, yellow line), leading to a decline of the RBCs flux.

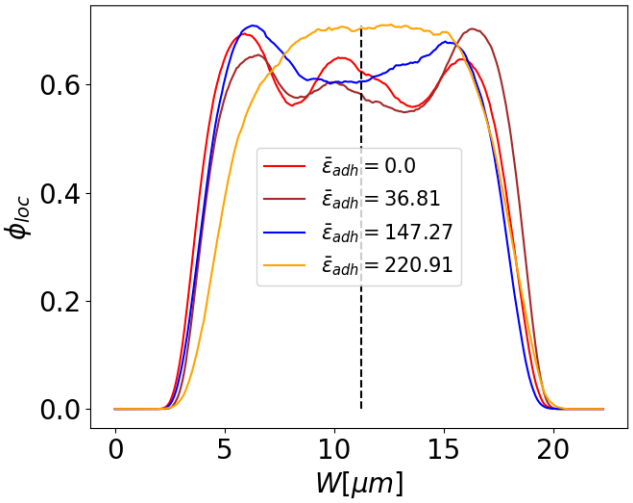

FIGURE 5.10 : Concentration profiles of suspension for different dimensionless adhesion energy values $\bar{\epsilon}_{adh}$. The black dashed line represents the channel center. Here $C_a = 25.0$ and $\phi_t = 46.0\%$

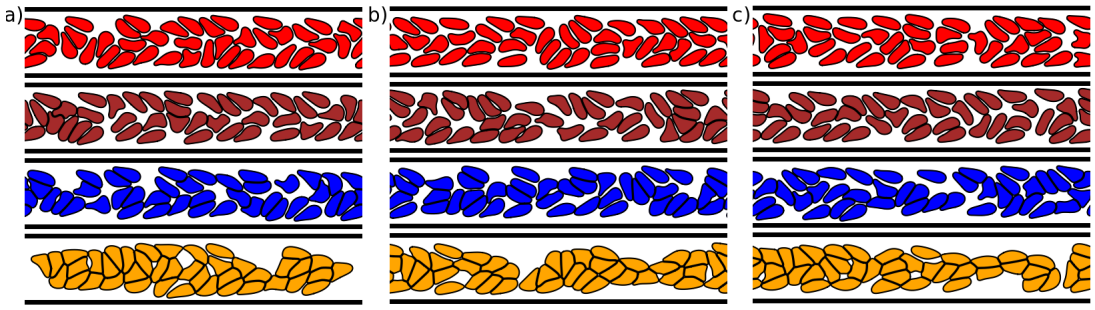

FIGURE 5.11 : Snapshots showing the spatial configurations of the cells at different time steps. a) $1500\tau_c$, b) $1750\tau_c$ and c) $2000\tau_c$. Here the capillary number is set to $C_a = 25.0$, the cells concentration is $\phi_t = 46.0\%$ and the viscosity contrast is set to $\lambda = 1.0$. The colors show different macroscopic adhesion energy values. Red : 0.0, brown : 36.81, blue : 147.27 and orange : 220.91

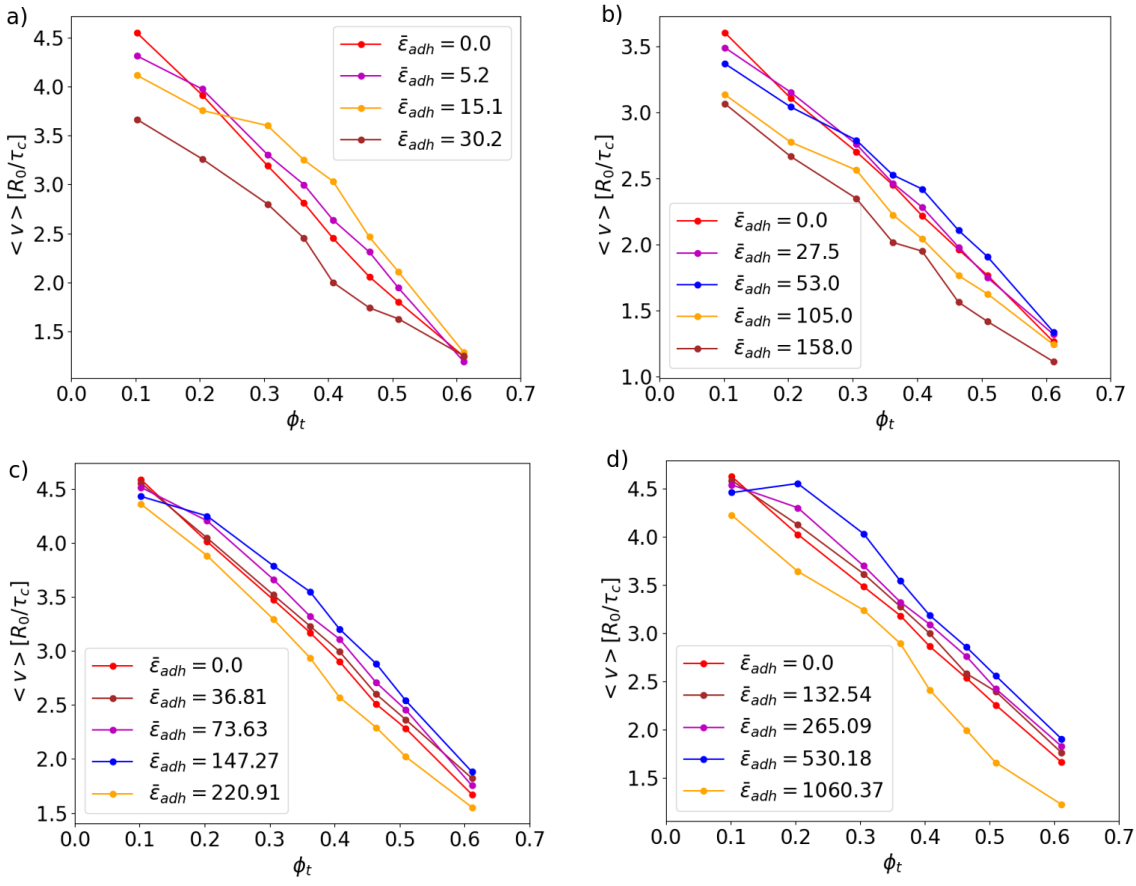

FIGURE 5.12 : The average velocity of vesicle mass center over cells and time as a function of volume fraction for channels with different dimensionless macroscopic adhesion energy. The simulation data are shown as dots. (a) $C_a = 0.9$, (b) $C_a = 9.0$, (c) $C_a = 25.0$, (d) $C_a = 90.0$.

5.3.4 The rheology of RBC aggregate suspension

In this section we examine briefly the behavior of the effective viscosity as a function of adhesion. The rheology of human blood has been studied since decades [Fåhraeus, 1929, Merrill et al., 1963, Chien, 1975, Menu et al., 2000, Armstrong et al., 2004, Brust et al., 2014]. The most prominent feature is the shear-thinning behavior, associated with destruction of RBCs rouleaux under shear flow. We will see below some novel features associated to microcirculation of blood rheology, and especially the behavior of viscosity as a function of shear rate and hematocrit.

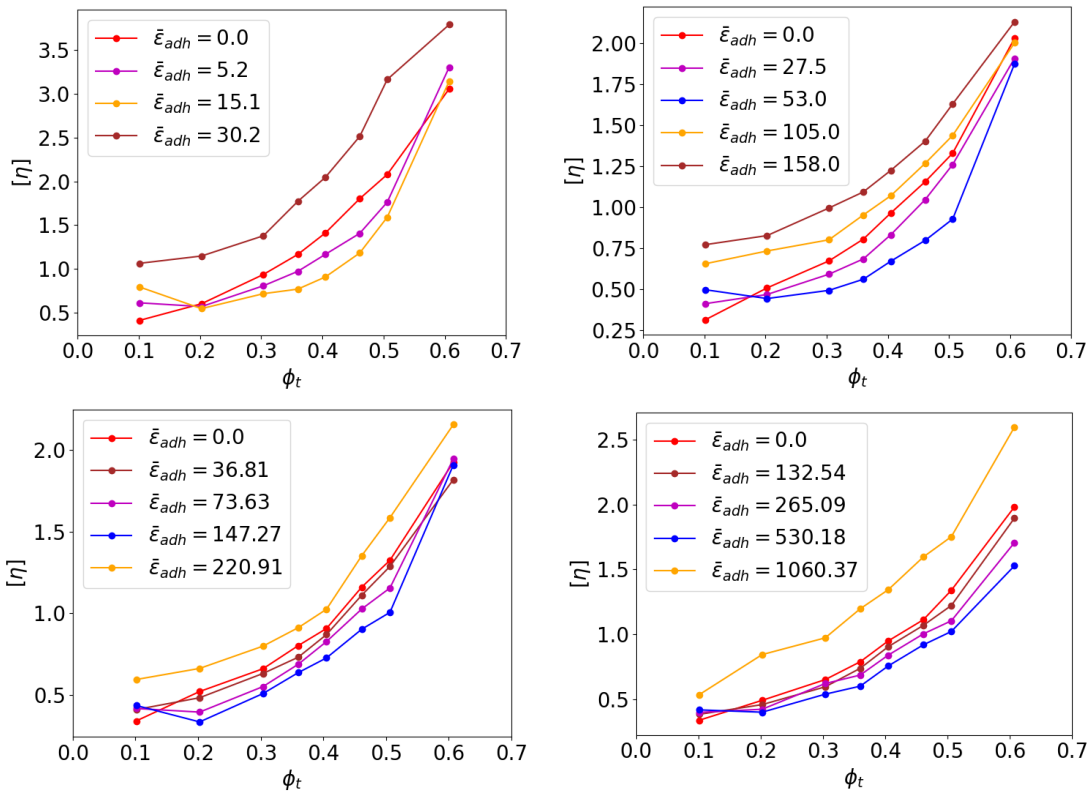

FIGURE 5.13 : The normalized viscosity as a function of volume fraction for channels with different dimensionless macroscopic adhesion energy. The simulation data are shown as dots. (a) $C_a = 0.9$, (b) $C_a = 9.0$, (c) $C_a = 25.0$, (d) $C_a = 90.0$.

Let us first examine the behavior of the normalized viscosity (defined in 5.3) as a function of hematocrit, for different adhesion energies.Figure. 5.13 shows the results. We see clearly that that in a quite wide range of hematocrit the normalized viscosity decreases by increasing adhesion energy, before it increases again. This is in agreement regarding the analysis of RBCs flux. The difference between the minimal viscosity (the lower curves in Figure. 5.13) and the viscosity without adhesion (red lines in Figure. 5.13) may attain about 50%. We believe that the origin of this behavior is similar to

that given for the non monotonic behavior of RBCs flux with the adhesion energy. In Fig. 5.14 we show (for a given hematocrit) the behavior of the normalized viscosity as a function of the adhesion energy. This figure exhibits the existence of a specific value of adhesion for which the viscosity is minimal. This specific adhesion depends on the capillary number.

Blood is a shear-thinning fluid, meaning that the blood viscosity decreases with shear rate. This is due to dissociation of RBCs upon increasing shear rate. In the presence of adhesion between cells the shear-thinning is observed (see in Fig .5.15). When $\lambda = 1.0$, the aggregates dissociate at high shear rate. This implies (see in Fig .5.15 (a)), all the curves, corresponding to different adhesion energies, collapse on each other at high shear rate. Contrary to the case $\lambda = 1.0$, at high enough viscosity contrast value $\lambda = 10.0$, the aggregates are quite robust. For this reason the curves in Fig .5.15 (b) do not collapse on each other at high shear rate.

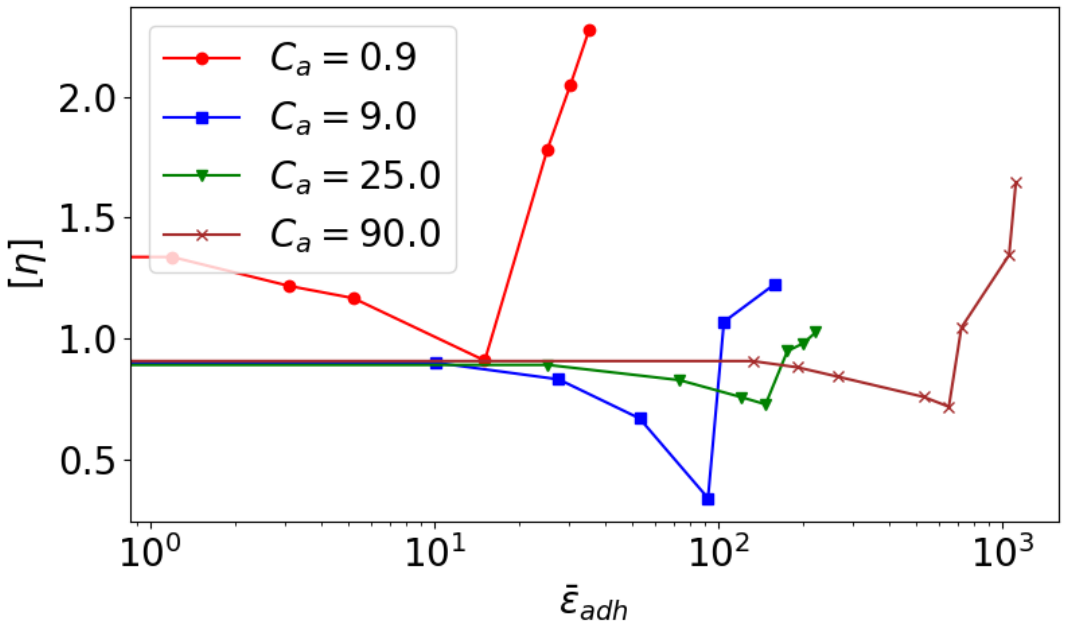

FIGURE 5.14 : The normalized viscosity as function of the dimensionless macroscopic adhesion energy for different values of capillary number. The horizontal axis is in logarithmic scale. here the cell concentration is $\phi_t = 46.0\%$.

5.4 Conclusion

A major finding of this chapter is the existence of an optimal adhesion energy corresponding to a maximum flux of cells. We have provided a qualitative argument to

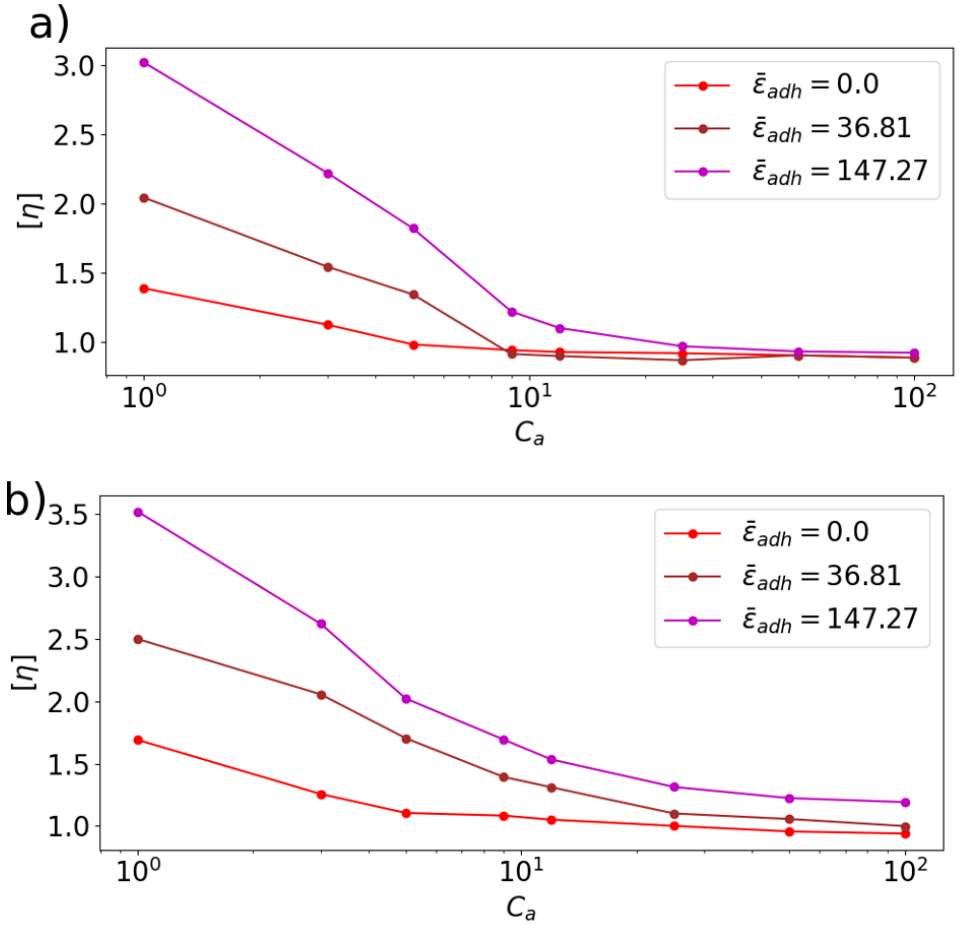

FIGURE 5.15 : The normalized viscosity as a function of capillary number with different dimensionless macroscopic adhesion energy. The simulation data are shown as dots. The cell concentration is $\phi_t = 40\%$. (a) $\lambda = 1.0$, (b) $\lambda = 10.0$

explain this counter-intuitive behavior. It is a combination of recirculation zones (see Fig. 5.9) that are suppressed due to aggregate formation (this lowers dissipation) and the fact that large aggregates (due to a high enough adhesion) tend to block the channel, and cause an obstacle for cell flow. The interplay between these two effects leads to an optimal adhesion energy. The non monotonic behavior is also exhibited by the effective viscosity of the suspension. We have also seen that adhesion can boost transport of RBCs to a level attaining up to about 30 % in comparison to the case without adhesion. In vivo, it is known that aggregates can form and can be broken by hydrodynamic stress, except in pathological situations where aggregates become robust and may tend to cause vessel occlusion. We have learnt from this study that an adhesion, which is not too strong, may be beneficial for perfusion.

This work has several limitations. Firstly, it was performed for a 2D study where some real physics of RBC is absent, such as cytoskeletton. This study could be viewed as a guide for a systematic 3D exploration. The fact that the phase diagram obtained in chapter 4 (regarding doublet dynamics) for 3D is strikingly similar to that obtained in 2D lends confidence that the 2D study analyzed in this chapter could, at least, have a qualitative value. Secondly, the study focused on a straight geometry, which is far away from real vascular networks. It will be imperative to analyze the various spatio-temporal properties, as well as transport phenomena occurring in real vascular networks. It is hoped that what we have learnt so far on a simplistic geometry and in 2D, will serve to identify relevant features to be studied in complex geometries.

Chapitre 6

The effect of pancreatic amylase activity on erythrocyte aggregation stability.

In the previous chapters we have shown several simulation results, and especially the occurrence of aggregation. This chapter deals with an experimental study of RBCs aggregation. The aggregation of RBCs due to fibrinogen, or dextran, has been undertaken by several authors. However, the role of glycocalyx in RBCs aggregation remains an open issue. Glycolcalyx is a brush of glycoproteins covering the membrane of RBCs (and mammalian cells in general). Glycocalyx is known to be altered in several diseases, such as diabetes. The role of how cleavage of glycocalyx affects RBCs aggregation is the main goal of this chapter. We have found that glycocalyx cleavage by enzymatic digestion dramatically enhances RBCs aggregation.

6.1 Introduction

Red blood cells (RBCs) are known to aggregate and disagregagate in a reversible manner under physiological conditions. In several cardiovascular diseases, such as hypercholesterolemia and diabetes, a high and abnormal RBCs aggregation have been reported [Groeneveld et al., 1999, Prasad and Kalra, 1993]. The main cause of the normal RBCs aggregation is a plasma protein, the fibrinogen [Brust et al., 2014]. Under physiological conditions the human fibrinogen level range is approximately (1.8 - 4 mg/ml), in this range, the aggregation process is believed to be reversible. In contrast, under some pathological conditions like diabetes, stable aggregates are known to form and may lead to vessel occlusions. Rogers et al [Rogers et al., 1992] reported that the aggregability of diabetic RBCs is more pronounced (from viscosity

measurements). They reported a correlation between this enhanced aggregation and the degradation of the glyco-protein layer (glycocalyx) of the RBCs membrane (which is charged negatively and prohibits a higher adhesion between RBCs). It has also been shown that the degradation of the RBCs glycogalyx due to enzyme activity enhances RBC-RBC adhesion under static conditions [Pot et al., 2011], by using rat blood. However a direct analysis of the role of glycocalyx layer in the aggregation process under flow is still lacking. This is a main goal of this chapter, where wee will use amylase as enzyme for glycocalyx degradation, and human blood samples.

Alteration of amylase activity is known in pancreatitis disease [Frossard et al., 2000, Popper and Necheles, 1940] (an inflammation of pancreas). In pancreatitis the levels of amylase may become four to six times higher than the upper limit of the normal range (40-200 U/l). In another context, that of space missions, it has been reported by Markin et al [Markin et al., 1998] that during space flights the pancreatic amylase enzyme of cosmonauts significantly increases (at least by 2 fold).

In the present chapter, we analyze experimentally the effect of amylase enzyme on erythrocytes aggregation. The erythrocytes glycocalyx is altered by means of α-amylase, present in vivo and released from pancreas. The size of RBCs clusters under flow, in a microfluidic device, as a function of amylase concentration is characterized in details. This study is supplemented with confocal microscopy in order to quantify the evolution of glycocalyx brush density as a function of amylase concentration.

6.2 Experimental method and image processing

The micro-channels mold were fabricated using SU-8-negative tone photo-epoxy GM 1060 (Gersteltec Sarl, Pully, Switzerland) and laser lithography printing machine Dilase 250 (KLOE, France). The mold was used to build the PDMS-based microfluidic device. The microfluidic device contains 20 micro-channels, each set of 5 micro-channel have the same width. The micro-channel widths considered are : $(15.0 \pm 0.2\mu)$, $(25.0 \pm 0.2\mu)$, $(35.0 \pm 0.2\mu)$ and $(45.0 \pm 0.2\mu)$. All the micro-channels have the same height and length which are respectively $(10.0 \pm 0.2\mu)$ and $(\simeq 3.0cm)$.

6.3 Results and discussion

6.3.1 The effect of α-amylase on the glycocalyx layer of red blood cells

The protocol of RBC treatment by amylase was presented in section 2.3.1.2. Fluorescence Microscopy (CFM) was used to characterize the effect of the α-amylase concentration on the glycocalyx layer of RBCs. The RBCs samples are prepared on glass coverslip which is coated with BSA to avoid crenation of RBCs. Solutions of 0.5% of RBCs diluted in PBS was prepared with different α-amylase solution concentrations. The glass coverslip was placed on the stage of a confocal microscope and image acquisition was performed. The measurements were carried out on the blood from five different healthy donors. The physiological range of blood amylase level is $70 - 235U/L$ [Frossard et al., 2000, Popper and Necheles, 1940]. Three values of α-amylase concentration were analyzed, namely 200 U/L (physiological range) and 500 U/L and 2000 U/L (pathological cases, such as in pancreatitis disease) [Frossard et al., 2000, Popper and Necheles, 1940]. Figure (6.1) shows healthy RBCs stained with Alexa488-conjugated WGA (a specific marker of glycocalyx). It is seen that the glycocalyx of non-treated RBCs presents a significantly higher fluorescence than the glycocalyx of RBCs treated with α-amylase, as as shown on Figure (6.1-b,c). Figure (6.1-a) shows the intensity of pixel color for different α-amylase concentration. The intensity of each pixel was averaged over all the images taken from RBCs samples of different five healthy donors. We see clearly in Fig (6.1-a) that the glycocalyx of the RBCs is not damaged when the RBCs were incubated in α-amylase with concentration within the physiological range. Under physiological conditions the α-amylase enzyme has no significant effect on the glycoprotein layer of RBCs. Beyond the physiological range of α-amylase level the intensity of the pixels related to the green color starts to decrease, a signature that the glycoproteins on the glycocalyx layer of RBCs are partially digested.

6.3.2 The effect of the glycocalyx degradation on aggregation morphology in absence of flow

The RBC aggregability in the absence of flow has been the subject of many classic studies [Chen et al., 1995, Foresto et al., 2000, Flormann et al., 2017, Hoore et al., 2018, Sheremet'ev et al., 2019]. The morphology of RBCs aggregates may be considered as an interesting characterization of the state of blood (healthy or unhealthy).

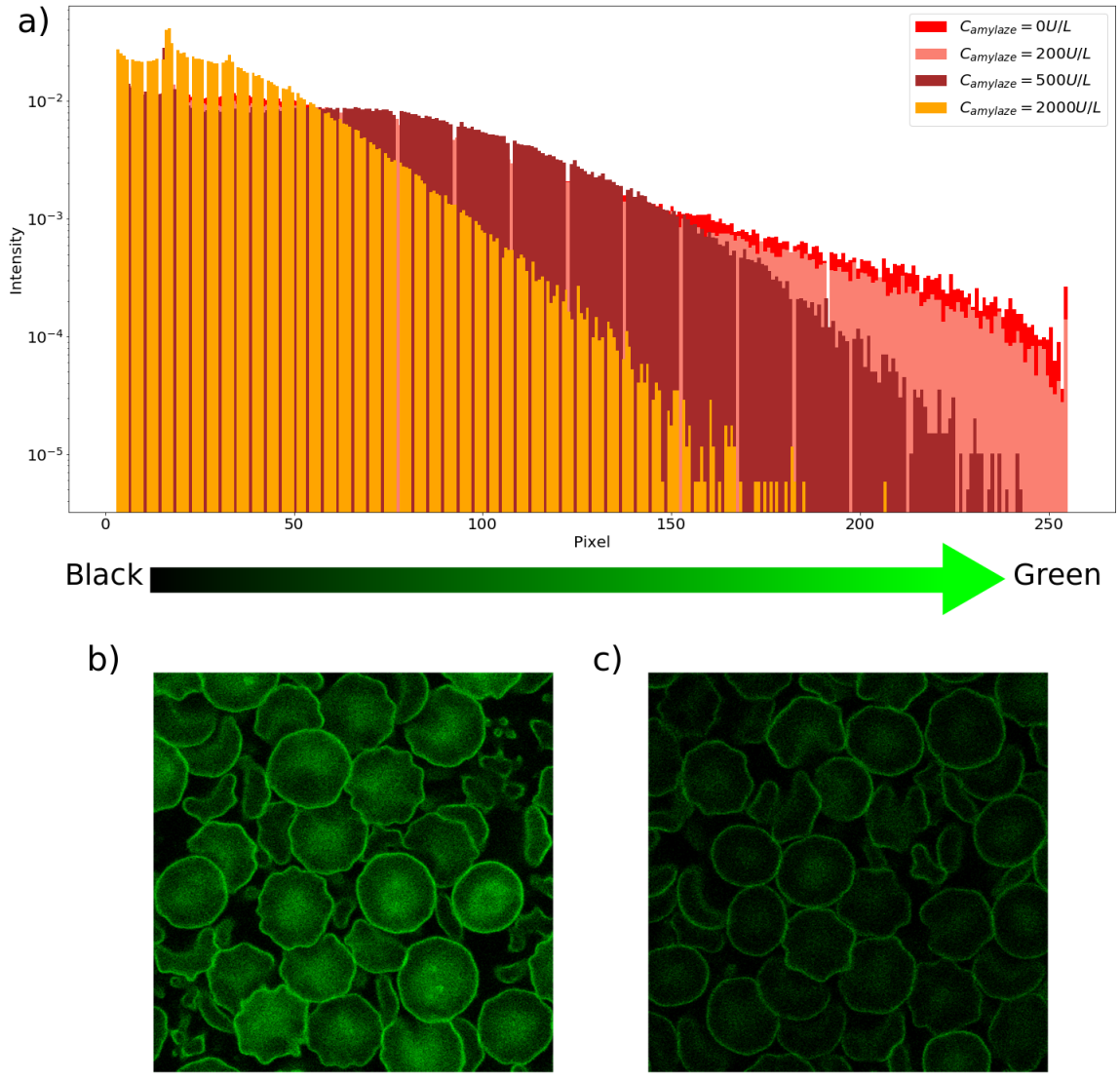

FIGURE 6.1 : Confocal images of the RBCs glycocalyx stained with Alexa488-conjugated wheat germ agglutinin. a) Intensity as a function of pixel color, b) and c) brute images ; b) No amylase - and c) pathological concentration –2000 U/L.

The (negative) electric surface charge is believed to play a major role in the erythrocytes aggregation. The magnitude of the electric surface charge should affect the interaction between erythrocytes. High RBCs aggregation is observed in various pathological cases. At low flow states or stasis, the aggregates show a rouleau shape (like coin stacking on each other), while abnormal RBC aggregation may lead to irregular aggregate structure like branched clusters [Chien and Jan, 1973]. After the degradation of the RBCs glycocalyx due to amylase, we induced the aggregation by dextran 150 ($15mg/ml$). The dextran 150 was chosen as it has been extensively used in aggregation studies [Maeda and Shiga, 1985, Clavería et al., 2016, Steffen et al., 2013]. Throughout this chapter the dextran 150 concentration is fixed at $15mg/ml$. This concentration is known to induce aggregation tantamount to to physiological case [Clavería et al., 2016]. By referring to aggreegation morphologies obtained in untreated RBCs, we can evaluate the effect of α-amylase on the aggregability of erythrocytes. The RBCs aggregation is characterized by the number of RBC per aggregates and the RBCs aggregate shape parameter which is defined as follows :

$$ASP = \frac{4\pi A}{P^2} \tag{6.1}$$

where A is the projected area of the aggregate and P is its perimeter.

Figure 6.2 shows the average number of RBC per aggregates as function of the concentration of α-amylase used to degrade the glycocalyx layer. The average is calculated over all the captured images (20 images from each sample of blood taken from different donors). We observe in Fig 6.2 that the average number of RBC per aggregates shows a stabilization from 0 to $200U/L$ of α-amylase, this range of α-amylase concentration is physiological range of blood α-amylase [Frossard et al., 2000, Popper and Necheles, 1940]. At $500U/L$ of α-amylase the average number of RBC per aggregate shows a slight increase. At higher concentrations of amylase beyond of $1000U/L$, which may be attributed to patients suffering from pancreatitis disease, the RBC per aggregate is significantly higher than the control case.

Not only the number of RBC per aggregates is affected by the degradation of glycocalyx. The aggregate morphology is also affected. We use here the parameter described in equation 6.1 to characterize the morphology of aggregates. An elongated linear shape corresponds to ASP value significantly smaller than 1, whereas a rounded shape has a value of ASP close to unity. We clearly see in Fig 6.3 that the ASP is very sensitive to the degradation of RBC glycocalyx. At low amylase concentration (amylase level less than $500U/L$) the ASP is smaller than 0.3, corresponding to aggregates in the form of in rouleaux. Increasing the amylase concentration leads

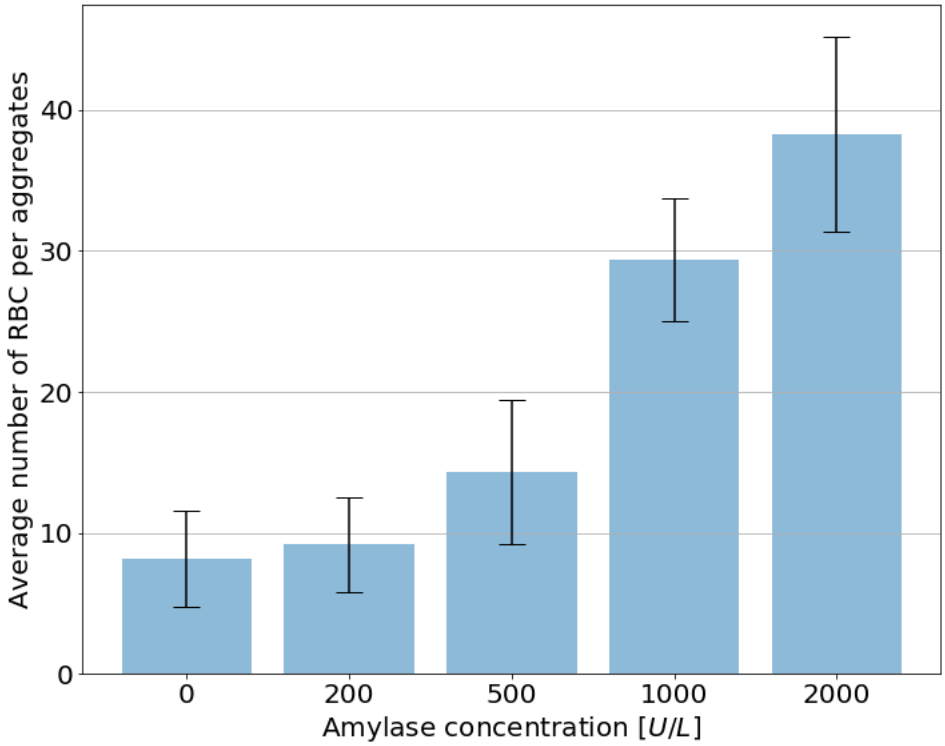

FIGURE 6.2 : The the average number of RBCs per aggregate for each group of amylase concentration.

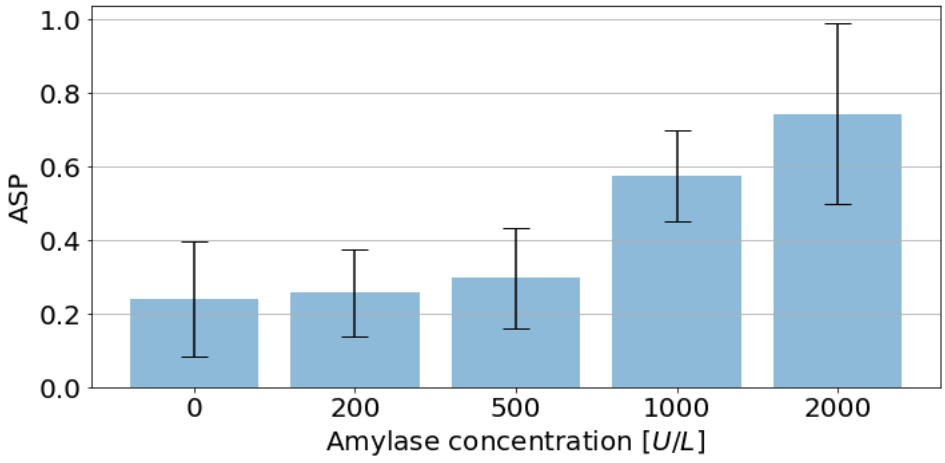

FIGURE 6.3 : Average values of RBC aggregate shape parameter for each group of amylase concentration.

to higher values of ASP. The associated morphology of the aggregates significantly deviate from classical rouleaux ; they exhibit a complex morphology, as shown in Fig 6.4 and 6.4.

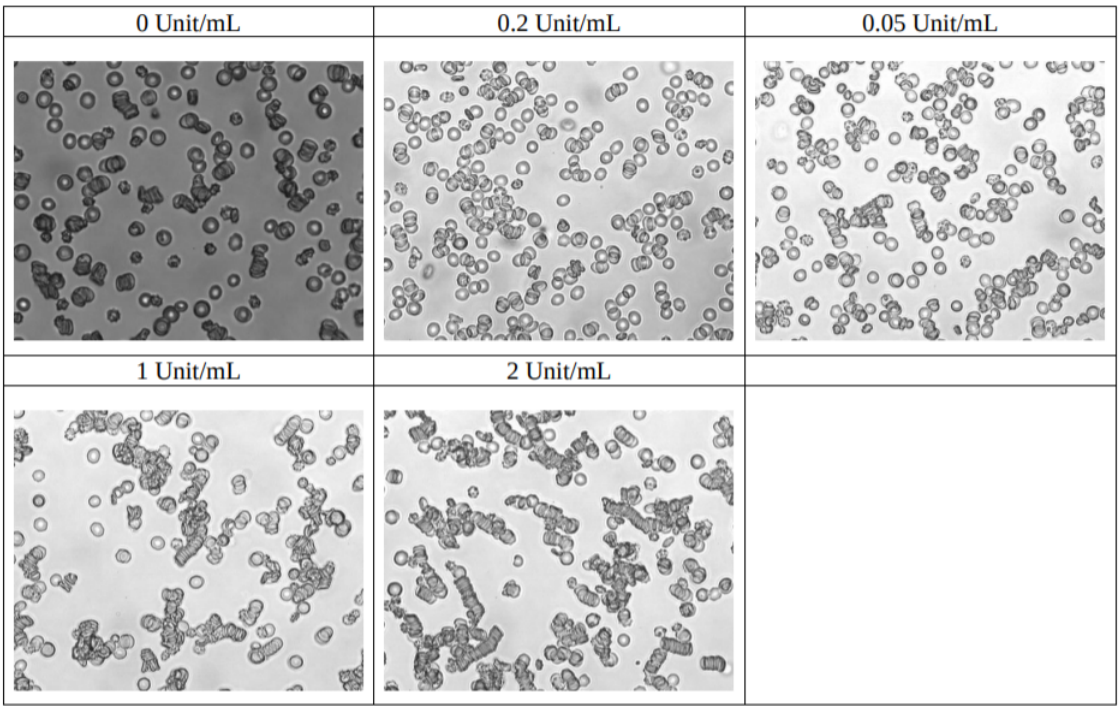

FIGURE 6.4 : Images of RBCs aggregates.

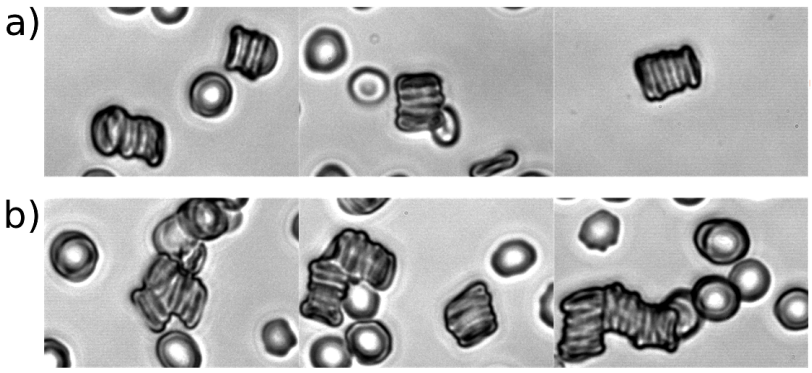

FIGURE 6.5 : Images of single RBCs aggregates. a) shows normal RBCs, b) shows amylase treated RBCs (the amylase level is $2000U/L$)

6.3.3 The stability of aggregates under flow

In order to evaluate the effect of the RBC glycocalyx degradation on the stability of aggregates, we performed microfluidic experiments as described in chapter 2. We pre-

pared the same samples used in subsection 6.3.2 as described in subsubsection 2.3.1.2. The microfluidic chip contains 25 straight parallel channels. Each sample is pumped through the channels. As an example, figure 6.8 shows imagees of two channels of different widths ($15\mu m$ and $45\mu m$). These images are recorded with a magnification of 60 to focus only on one channel and the resolution is chosen depending on the channel width. Each image was processed separately where we calculated the number of RBC per aggregates. Figure 6.7 summarizes our funding. We quantified the probability density of occurrence of a cluster of a given size for different applied pressures and different concentrations of amylase.

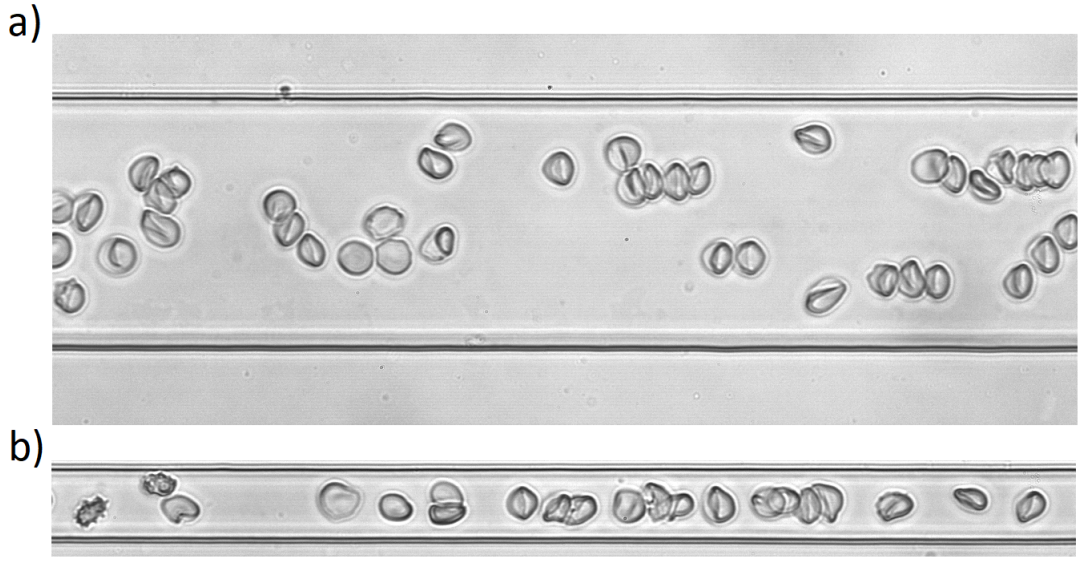

FIGURE 6.6 : Pictures of red blood cells flowing through microfluidic channel. Flow is from left to right. a) channel of width $45\mu m$. b) channel of width $15\mu m$.

At low pressure difference we see that the probability density of occurrence of each cluster type is approximately the same for the aggregates that contains about 11 RBCs or less. This is due to the low value of pressure difference. At low pressure difference the aggregation force is stronger than the disaggregation force induced by the flow stress, so that the distribution of size is not too much sensitive to the flow. However, and as seen in Fig. 6.7, at high enough pressure difference the aggregates contains higher numbers of RBCs when the amylase concentration is 2000U/L. This due to the degradation of the RBCs glycocalyx and the fact that the hematocrite in channels increases with the pressure difference. The cleavage of the RBC glycocalyx does not only lead to an increase of the number of RBC per aggregates but also affects the morphology ; we see in Fig. 6.9 that at high value of amylase concentration some

aggregates show complex morphology in contrast to the case where the RBCs glycocalyx is not degraded. We compared the stability of RBCs aggregates by observing the aggregates at different pressure differences for different values of amylase concentration. We found that in the case of normal RBCs, the aggregates dissociate at high enough pressure difference, in contrast to RBCs treated with high concentration of amylase (2000U/L), the RBCs aggregates remain quite stable even at high pressure difference, as shown in Fig. 6.10 and Fig. 6.11. To verify the stability of RBCs aggregates under flow, we calculate the average of aggregate shape parameter as a function of the number of RBCs per aggregate, and we analyze this quantity for different applied pressure difference for two cases (0 U/L and 2000U/L of amylase). We clearly see in Fig .6.8 (left panel) that the applied pressure has an effect on the aggregate shape parameter, the aggregates tend to align with flow and show cylindrical shape. In contrast to normal RBCs, the RBCs treated with amylase form stable aggregates, the applied flow has roughly no noticeable effect on the aggregate shape parameter (Fig .6.8 right) and the aggregate morphology is more complex compared to the case of normal RBCs.

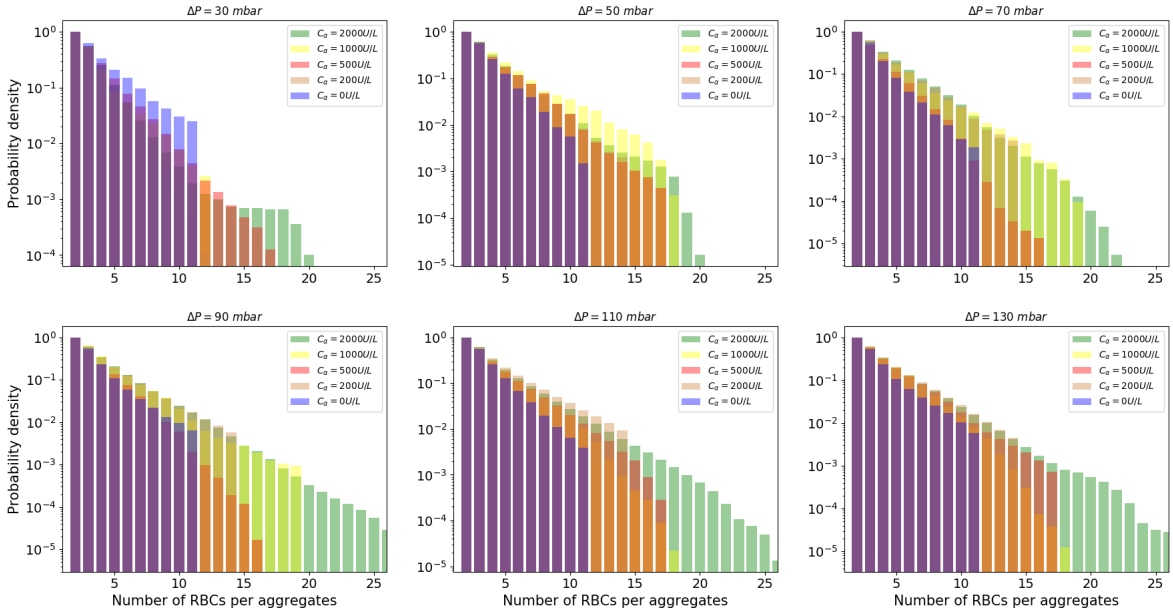

FIGURE 6.7 : The probability density of the size of RBCs aggregates for each group of amylase concentration and for different pressure difference values. The channel width here is $45\mu m$

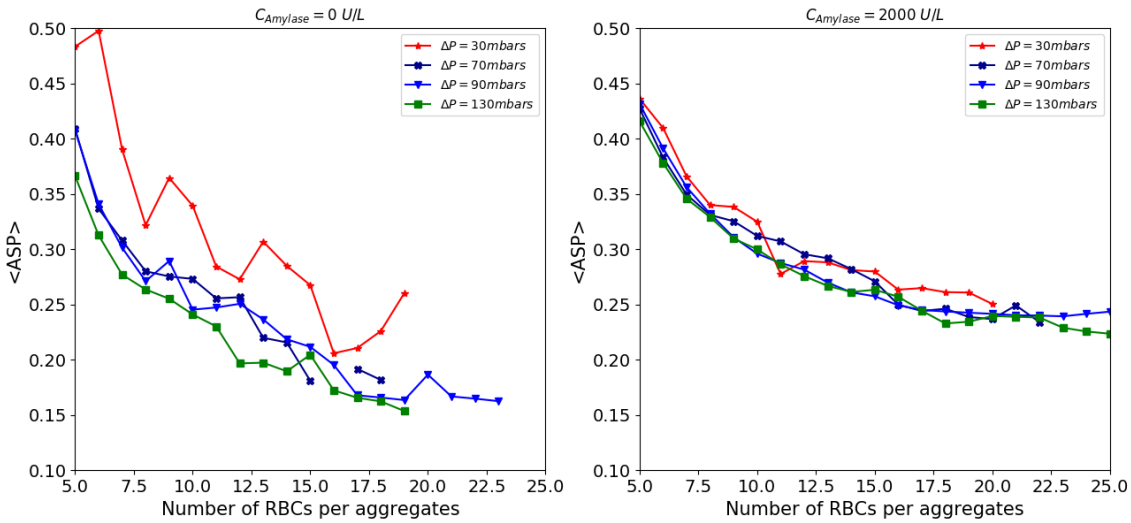

FIGURE 6.8 : Average values of RBC aggregate shape parameter as a function of the number of RBCs per aggregate for each group of amylase concentration and for different applied pressure difference. The channel width here is $45\mu m$

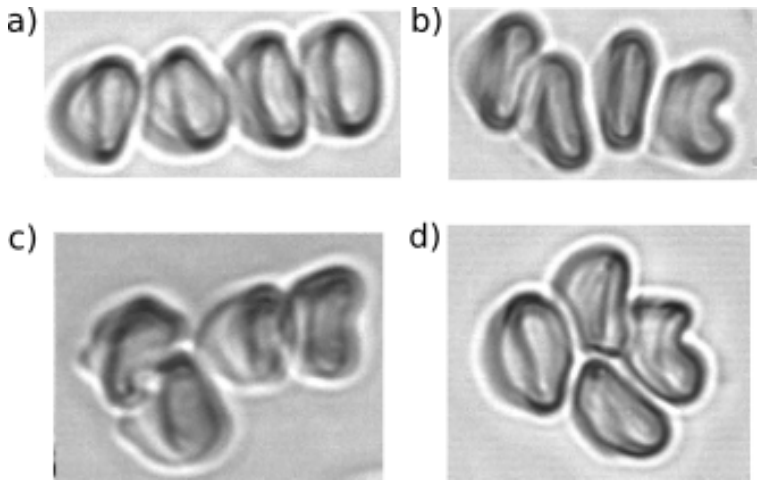

FIGURE 6.9 : Images of RBCs aggregates under in straight channel for different concentration of $\alpha-$amylase. a) $0U/L$, b) $500U/L$, c) $1000U/L$, d) $2000U/L$

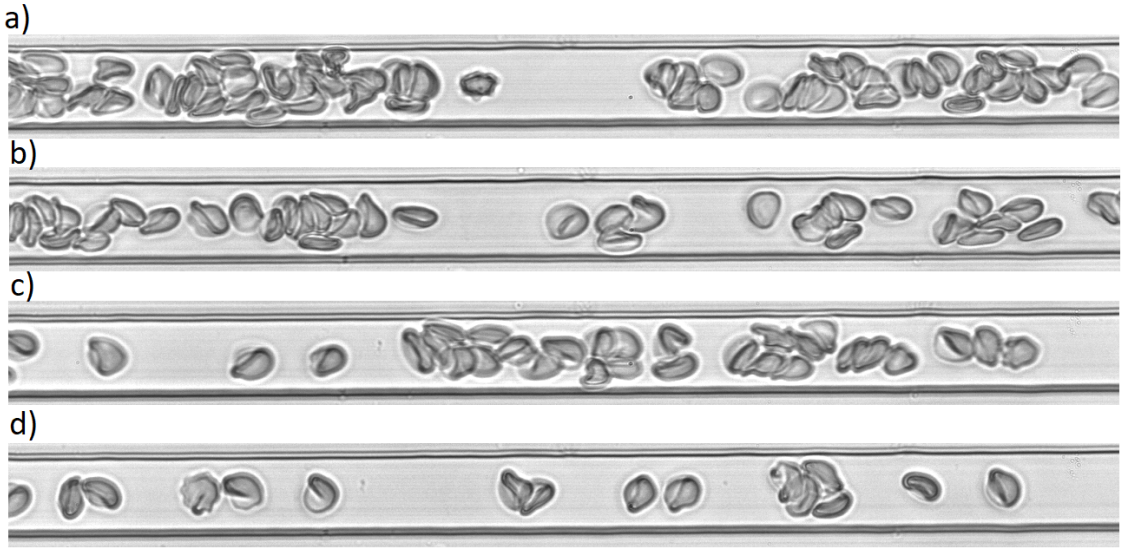

FIGURE 6.10 : Images from experiments for different applied pressure difference values. a) $30mbars$, b) $50mbars$, c) $70mbars$, d) $120mbars$. The channel width here is $15\mu m$ and the concentration of $\alpha-$amylase is $2000U/L$

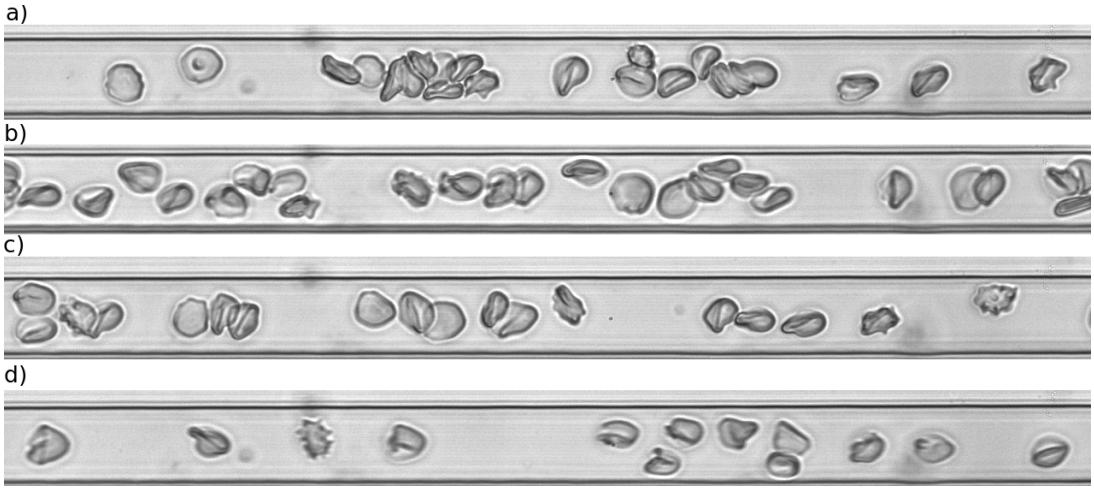

FIGURE 6.11 : Images from experiments for different applied pressure difference values. a) $30mbars$, b) $50mbars$, c) $70mbars$, d) $120mbars$. The channel width here is $15\mu m$ and the concentration of $\alpha-$amylase is $0U/L$

6.4 Conclusion

This first step study has highlighted the role of glycocalyx cleavage caused by amylase enzyme in the process of RBCs aggregation. We have examined the aggregate morphology and stability as functions of pressure difference and amylase concentration. Cleavage of glycocalyx significantly affects size, morphologies and stability of RBCs clusters. This may lead to vascular complications for patients having a high level of amylase activity. It has been reported that some patients suffering from pancreatitis disease present vascular complications [Barge and Lopera, 2012,Kirby et al., 2008,Balachandra and Siriwardena, 2005], such as vessel injury, like blood wall erosion. We are not aware of any study using directly patients blood, and this will constitute an interesting perspective. Note also that amylase affects not only the RBCs glycocalyx, but also the endothelial cells glycocalyx. This may lead to endothelial dysfunction, that can favor undesirable adhesion of blood elements on the endothelium. A promising line of research, which will be studied in the team, is to to analyze RBCs flow in a microvasculature on a chip. Indeed, our team was able (few years ago) to produce microfluidic circuits which are coated with a confluent monolayer of human endothelial cells (EC). A systematic study should then be undertaken where both RBCs and ECs can be incubated with amylase (or other more specific enzymes), and the flow properties analyzed. It is also known that several other diseases are associated with endothelium impairing [Rajendran et al.,], such as diabetes, heart failure, and so on. This type of experiments should provide a new angle of attack to identify key elements associated with the role of glycocalyx cleavage in cardiovascular complications.

Chapitre 7

Conclusions and perspectives

In this chapter we briefly recall the main results and and outlooks, which may constitute an interesting task for future investigations. The main topic of this thesis has focused on the erythrocyte aggregates dynamics and rheology. The main findings and some perspectives are summarized below :

7.1 Summary of Chapter 3 and related perspectives

In Chapter 3, we showed by means of two dimensional simulations that the spectrin network of RBCs membrane (called cytoskeleton) is not essential for the the occurrence of multilobe shapes of RBCs, which were reported a long time ago [Fischer et al., 1978a], and analyzed in some details more recently [Mauer et al., 2018, Lanotte et al., 2016]. In these studies [Mauer et al., 2018, Lanotte et al., 2016], the authors attributed the multilobe manifestation to the RBC cytoskeleton. Multilobes are caused only by membrane tension due to hydrodynamic stress. We analyzed the multilobe shape lateral position and have linked it to the normal stress difference. The present finding provides further evidence that a 2D vesicle model already captures many important features of real RBCs. The 2D model can be (due to its rapid handling from computational point of view) very useful in exploring new phenomena, especially for dense suspensions, before resorting to the computationally more expensive RBC model. An interesting line of future investigation is the analytical analysis of MB shapes, following the methods exposed in [Misbah, 2006b, Lebedev et al., 2007, Danker et al., 2007, Farutin et al., 2010]. In those studies either second spherical harmonic [Misbah, 2006b, Lebedev et al., 2007, Danker et al., 2007] (this is the first excited mode in a linear shear flow), or the fourth order harmonic [Farutin et al., 2010] have been

included ; including fourth order harmonic turned out to be decisive to account for full numerical simulations. In that study centrosymmetry was imposed, an assumption which is clearly not valid for a multilobe shape. It will be essential to relax this assumption if we wish to account for this new phase. It is hoped to investigate this matter in the future.

7.2 Summary of Chapter 4 and related perspectives

In Chapter 4, we studied the dynamics and rheology of erythrocyte-erythrocyte aggregate (RBC doublet) by two dimensional and three dimensional simulations. We found that the doublet under shear flow undergoes several dynamics. The new phases found are : Rolling (R), flexible rolling (FR), rolling and sliding (RS), flow alignment(FA) and separation (S). In particular, we showed that RBCs doublet may be robust even for very high shear stress. We provided some explanation regarding the RBCs doublet dissociation. The membrane trank-treading enhances significantly the separation between two adhered RBCs.

7.3 Summary of Chapter 5 and related perspectives

The purpose of the Chapter 5 was to analyze numerically the effect of adhesion energy on the transport of RBCs in straight channels. The most interesting finding from this analysis is the existence of an optimal adhesion energy corresponding to a maximum flux of cells. It has been found that a physiological adhesion boosts RBCs flux. In this study, we provided an explanation for this counter-intuitive behavior. The formation of large and stable aggregates leads to the suppression of some flow recirculations (and thus dissipation). The large aggregates block the channel laterally. This leads to a drop down of the RBCs flux. We highlighted the fact that the RBCs flux is strongly related to the spatio-temporal configuration of RBCs. In vivo, under the physiological conditions, the aggregates are forming in reversible way (we showed this behavior in subsection 5.3.1), RBCs form aggregates and then they dissociate due to hydrodynamic stress. In contrast, under pathological conditions (diabetes, sickle cell anemia and so on) once the RBCs form aggregates they do not dissociate eeasily. This may lead to vessel occlusion. Further investigations of RBCs aggregates flux flowing

through vascular network (Fig. 7.1) are needed in order to reach a clear conclusion regarding the vessel occlusion due to the formation of robust aggregates.

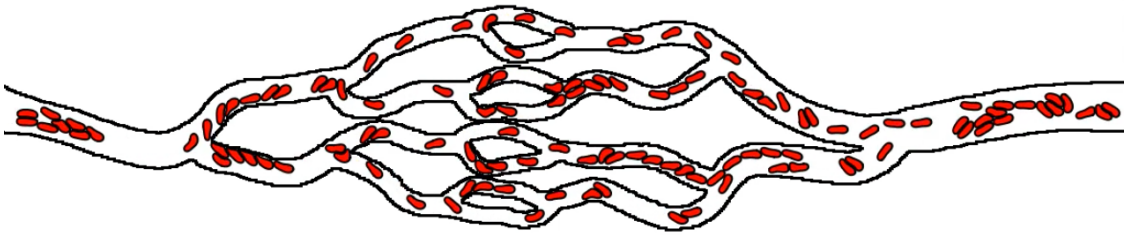

FIGURE 7.1 : Snapshot of two dimensional simulations showing the spatial configuration of RBCs aggregates flowing in vascular network (the geometry used in this simulation is taken from [Balogh and Bagchi, 2017])

7.4 Summary of Chapter 6 and related perspectives

In Chapter 6, we presented our experimental works. We investigated the role of glycocalyx cleavage on the RBCs aggregation and aggregates stability. Using confocal microscopy we showed that at high concentration of amylase enzyme the RBC glycocalyx undergoes a degradation. We subsequently showed that the glycocalyx cleavage has a dramatic effect on the RBCs aggregation, in that the aggregates contains high number of RBCs and exhibit a complex morphology.. The stability of aggregates may lead to vascular complications for patient suffering from RBCs glycocalyx degradation. For a further study, we propose to analyze the stability of aggregates flowing through bifurcation as shown in Fig. .7.2. In real vasculatures RBCs interact with endothelial cells (a monolayer of cell covering the inner wall of vessels). The enzymes affects also the endothelial cells glycocalyx. A systematic study about the interaction between RBCs and endothelial cells (with degraded glycocalyx) is needed to draw a complete conclusion on the vessel occlusion.

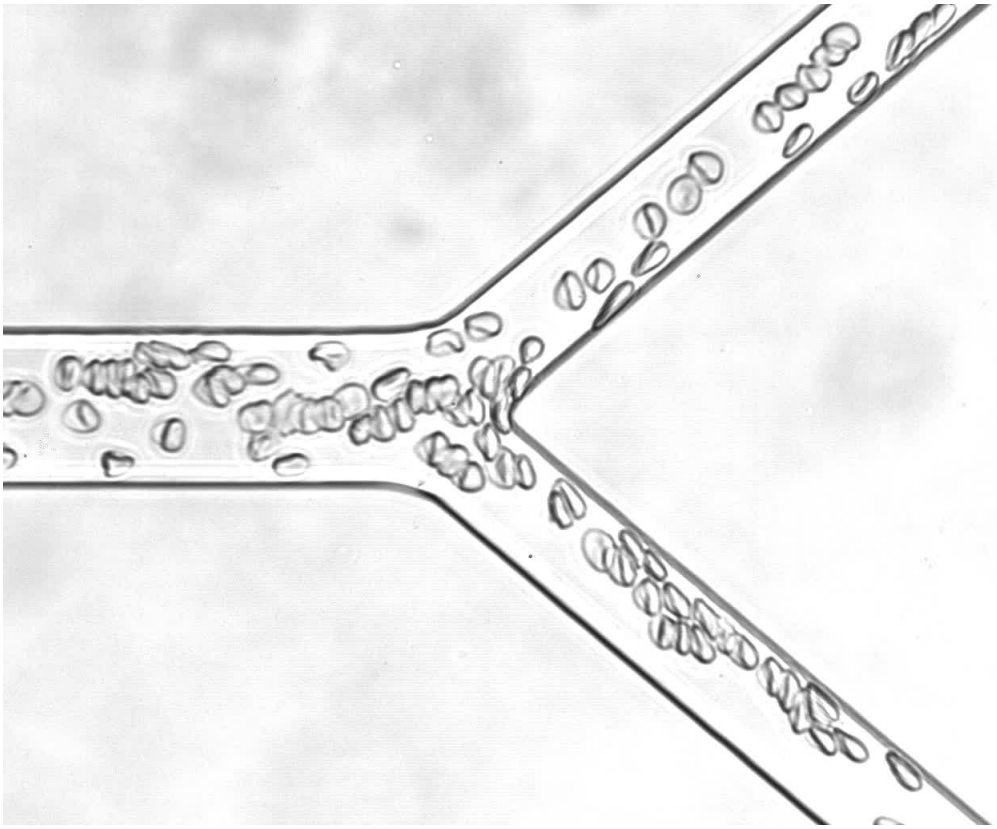

FIGURE 7.2 : Picture of RBCs flowing through microfluidic network channel

List of publications

Mehdi Abbasi, Alexander Farutin, Hamid Ez-Zahraouy, Abdelilah Benyoussef, and Chaouqi Misbah . Erythrocyte-erythrocyte aggregation dynamics under shear flow. 2021. Phys. Rev. Fluids, 2021 , Volume 6, pages 023602.

https://link.aps.org/doi/10.1103/PhysRevFluids.6.023602

Zhe Gou, Hengdi Zhang, **Mehdi Abbasi**, Chaouqi Misbah. Red Blood Cells Under Flow Show Maximal ATP Release for Specific Hematocrit. Biophysical Journal, 2021, vol. 120, no 21, p. 4819-4831.

https://doi.org/10.1016/j.bpj.2021.09.025

Sofia Biagi, Lorenzo Rovigatti, **Mehdi Abbasi**, Lionel Bureau, Francesco Sciortino, Chaouqi Misbah. Hydrodynamic instability and flow reduction in polymer brush coated channels. Soft Matter, 2021 , 17, pp.9235-9245.

https://hal.archives-ouvertes.fr/hal-03450373/document

Mehdi Abbasi, Alexander Farutin, Abdessamad Nait-Ouhra, Hamid Ez-Zahraouy, Abdelilah Benyoussef, and Chaouqi Misbah. Dynamics and rheology of a single two-dimensional multilobe vesicle in a confined geometry. Phys. Rev. Fluids, 2022, 7, 093603.

https://journals.aps.org/prfluids/abstract/10.1103/PhysRevFluids.7.093603

Shen Zaiyi, Plouraboué Franck, Lintuvuori Juho S, Zhang Hengdi, **Mehdi Abbasi** and Chaouqi Misbah. Anomalous Diffusion of Deformable Particles in a Honeycomb Network. Phys. Rev. Letters. 2023. 130. 014001.

https://journals.aps.org/prl/abstract/10.1103/PhysRevLett.130.014001

Zhe Gou, Hengdi Zhang, Abdessamad Nait-Ouhra, **Mehdi Abbasi**, Alexander Farutin and Chaouqi Misbah. Dynamics and rheology of vesicles under confined Poiseuille flow. *Submitted*

Mehdi Abbasi and Chaouqi Misbah. Red blood cells aggregates transport for finite concentration. *In preparation*

Mehdi Abbasi, et al. The effect of pancreatic amylase activity on erythrocyte aggregation stability. *In preparation*

Appendix A

Details of the numerical simulation method (SBIM)

Due to the linearity of Stokes equations we can transform the set of fluid equations into an integral equation which is non-local. This is based on the use of Green's function techniques [Pozrikidis, 1992]. This method enjoys quite a good precision. We used the Green's functions that satisfy directly the no-slip boundary condition at the channel walls in our previous works. Those Green's functions do not have an explicit representation in elementary functions. Instead, the Green's function values were calculated numerically on a fixed grid and stored in a table. The values for arbitrary positions were obtained by interpolation. Here we use a different approach which we have found to result in lower computational cost of the simulation, in particular for a dense suspension. We take the Green's functions that satisfy the periodic boundary conditions along the x direction and use an explicit discretization of the wall. The wall force and residual velocity at the wall are parametrized by a Fourier series thanks to the periodicity in x direction, as explained below. The advantage of this method is that a relatively small number of Fourier harmonics is sufficient to reduce the residual velocity at the wall to machine precision, unless there are membrane points very close to the wall. This is because the self-interactions of the walls are calculated exactly in Fourier space using analytical expressions.

The velocity at any point $\mathbf{r}$ in the simulation domain satisfies the following equation

$$\Lambda(\mathbf{r})\mathbf{v}(\mathbf{r}) = \mathbf{v}^{\infty}(\mathbf{r}) + \mathbf{v}^{ves}(\mathbf{r}) + \mathbf{v}^{wall}(\mathbf{r}), \tag{A.1}$$

where $\mathbf{v}^{\infty}(\mathbf{r})$ is the imposed velocity field, $\mathbf{v}^{ves}$ is the velocity field produced by the vesicles, and $\mathbf{v}^{wall}$ is the velocity field produced by the wall. The coefficient Λ is

defined as

$$\Lambda(\mathbf{r}) = \begin{cases} \lambda & \text{if } \mathbf{r} \text{ is inside a vesicle.} \\ (1+\lambda)/2 & \text{if } \mathbf{r} \text{ is on a vesicle membrane.} \\ 1 & \text{if } \mathbf{r} \text{ is outside all vesicles or is on a wall.} \end{cases} \tag{A.2}$$

Here λ is the viscosity contrast defined as $\lambda = \dfrac{\eta_1}{\eta_0}$. The vesicle contribution is defined as

$$\mathbf{v}^{ves}(\mathbf{r}) = \frac{1}{\eta_0} \oint_m \underline{\underline{G}}(\mathbf{r}_0, \mathbf{r}) \cdot \mathbf{f}(\mathbf{r}_0) ds(\mathbf{r}_0) + (1-\lambda) \oint_m \mathbf{v}(\mathbf{r}_0) \cdot \underline{\underline{T}}(\mathbf{r}_0, \mathbf{r}) \cdot \mathbf{n}(\mathbf{r}_0) ds(\mathbf{r}_0), \tag{A.3}$$

where $\underline{\underline{G}}(\mathbf{r}_0, \mathbf{r})$ and $\underline{\underline{T}}$ are the Green's functions (G_{ij} refers to the so-called single-layer contribution, while T_{ijk} accounts for the double-layer contribution). Here we take the Green's functions satisfying periodic boundary conditions in x direction, which have a known expression in terms of elementary functions [Pozrikidis, 1992]. These functions reduce the integration over an infinite array of image vesicles arranged periodically in the x direction to an integral over a single vesicle inside the computational domain. The integration in Eq. (A.3) is thus taken along the membranes of all vesicles in the computational domain.

Note that the above Green's functions do not satisfy the no-slip boundary condition at the walls (in contrast to one of our previous studies [Thiébaud and Misbah, 2013]), therefore the contribution of the walls to the velocity field has to be taken explicitly. This contribution should precisely guarantee the no-slip condition at the walls. The wall contribution is written as

$$\mathbf{v}^{wall}(\mathbf{r}) = \frac{1}{\eta_0} \oint_{walls} \underline{\underline{G}}(\mathbf{r}_w, \mathbf{r}) \cdot \mathbf{f}^w(\mathbf{r}_w) dx, \tag{A.4}$$

where $\mathbf{r}_w$ is wall position and $\mathbf{f}^w(\mathbf{r}_w)$ is the density of forces applied by the wall on the fluid at a position $\mathbf{r}_w$. The wall force is not known *a priori* and needs to be solved for to satisfy the no-slip condition at the wall, as described below. The contour integral along the walls is simplified to the integral with respect to the x coordinate in Eq. (A.4). Note that the above contribution is similar in form to the first contribution in (A.3), because in applying the Green's theorem one has to integrate over all boundaries (vesicle and bounding walls).

The no-slip boundary conditions at the walls are implemented in the following way: Because the velocity of the walls is defined by the imposed shear flow ($\boldsymbol{v}^\infty$ in Eq. (A.1)), the no-slip condition reduces to

$$\boldsymbol{v}^{ves}(\boldsymbol{r}^w) + \boldsymbol{v}^{wall}(\boldsymbol{r}^w) = 0 \tag{A.5}$$

for all $\boldsymbol{r}^w$ at the wall. The first term in Eq. (A.5) is given explicitly by Eq. (A.3), while the second term is related by a linear operator to the wall forces. We thus need to solve Eq. (A.5) for the wall forces. The next step is to use the obtained wall forces to calculate the flow $\boldsymbol{v}^{wall}$ on the vesicle membranes, using Eq. (A.4). The wall forces and the velocity fields measured at the wall remain invariant after translation by L_x in x direction thanks to the periodic boundary conditions. We thus represent these three fields by Fourier series in x:

$$\begin{aligned}
v_x^{ves}(x, L_y/2 \pm L_y/2) + i v_y^{ves}(x, L_y/2 \pm L_y/2) &= \sum_{k=(1-N_w)/2}^{(N_w-1)/2} v_{k,u/l}^{ves} e^{2\pi i k x/L_x}, \\
v_x^{wall}(x, L_y/2 \pm L_y/2) + i v_y^{wall}(x, L_y/2 \pm L_y/2) &= \sum_{k=(1-N_w)/2}^{(N_w-1)/2} v_{k,u/l}^{wall} e^{2\pi i k x/L_x}, \\
f_x^{wall}(x, L_y/2 \pm L_y/2) + i f_y^{wall}(x, L_y/2 \pm L_y/2) &= \sum_{k=(1-N_w)/2}^{(N_w-1)/2} f_{k,u/l}^{wall} e^{2\pi i k x/L_x},
\end{aligned} \tag{A.6}$$

where $v_{k,u/l}^{ves}$, $v_{k,u/l}^{wall}$, and $f_{k,u/l}^{wall}$ are the corresponding Fourier components. The second index u in $v_{k,u/l}^{ves}$ refers to the upper wall ($y = L_y$ in the left hand side of Eq. (A.6)), while l refers to the lower wall ($y = 0$ in the left hand side of Eq. (A.6)). N_w sets the number of Fourier harmonics used for wall discretization.

The coefficients $v_{k,u/l}^{ves}$ can be calculated directly without calculating the velocity at the wall in the coordinate space:

$$v_{k,u/l}^{ves} = \frac{1}{\eta_0} \oint_m \mathbf{G}_{k,u/l}(\mathbf{r}_0) \cdot \mathbf{f}(\mathbf{r}_0) ds(\mathbf{r}_0) + (1-\lambda) \oint_m \mathbf{v}(\mathbf{r}_0) \cdot \underline{\underline{T}}_{k,u/l}(\mathbf{r}_0) \cdot \mathbf{n}(\mathbf{r}_0) ds(\mathbf{r}_0), \tag{A.7}$$

where the kernels $\mathbf{G}_{k,u/l}(\mathbf{r}_0)$ and $\underline{\underline{T}}_{k,u/l}(\mathbf{r}_0)$ depend only on the wall position and L_x. These kernels can be expressed in elementary functions as shown in [Pozrikidis, 1992].

The amplitudes $v_{\pm k,u/l}^{wall}$ and $f_{\pm k,u/l}^{wall}$ can be related to each other as

$$(v_{\pm k,u/l}^{wall}) = \frac{1}{\eta_0} G^{wall}(k) (f_{\pm k,u/l}^{wall}), \tag{A.8}$$

where $(v_{\pm k,u/l}^{wall})$ and $(f_{\pm k,u/l}^{wall})$ are 4D complex vectors composed of the corresponding components and $G^{wall}(k)$ is a 4x4 complex matrix, which depends only on L_x and L_y and whose explicit expression is given in [Pozrikidis, 1992].

The wall force amplitudes are thus obtained by solving

$$(v_{k,u/l}^{ves}) + \frac{1}{\eta_0} G^{wall}(k) (f_{\pm k,u/l}^{wall}) = 0, \ k \geq 0 \tag{A.9}$$

for the 4D complex vector $(v^{ves}_{k,u/l})$ computed from Eq. (A.7). Note that Eq. (A.9) is degenerate for $k = 0$, since normal forces with constant amplitude produce no flow.

Finally, the wall contribution to the velocity field in the fluid domain can be obtained from known $(f^{wall}_{\pm k,u/l})$ as

$$\mathbf{v}^{wall}(\mathbf{r}) = \frac{1}{\eta_0} \sum_{j\in\{u,l\}} \sum_{k=(1-N_w)/2}^{(N_w-1)/2} G_{k,j}(\mathbf{r}) f^{wall}_{k,j}. \tag{A.10}$$

The periodic boundary conditions respect the translational invariance of the Green's kernels, which depend only on the relative positions of the source and target points, as in the free-space case: $\underline{\underline{G}}(\boldsymbol{r}_0, \boldsymbol{r}) = \underline{\underline{G}}(\boldsymbol{r}_0 - \boldsymbol{r})$, $\underline{\underline{\underline{T}}}(\boldsymbol{r}_0, \boldsymbol{r}) = \underline{\underline{\underline{T}}}(\boldsymbol{r}_0 - \boldsymbol{r})$. The explicit expressions and their presentation are copied from [Pozrikidis, 1992]. We have made a small correction, as explained below.

Following [Pozrikidis, 1992], we assume the periodicity direction of the system to be oriented along the x axis and the period of the system is given by L_x. This defines the wave number $q = 2\pi/L_x$. Following [Pozrikidis, 1992], we introduce a function A, defined as

$$A(\boldsymbol{r}) = \frac{1}{2} \ln[\cosh(qr_y) - \cos(qr_x)] - \frac{1}{2} \ln 2. \tag{A.11}$$

The function A represents a solution of the Poisson's equation for a periodic array of point charges. Using this function, the Green's kernels for the Stokes equation can be written as [Pozrikidis, 1992]

$$\underline{\underline{G}}(\boldsymbol{r}) = \frac{1}{4\pi} \begin{pmatrix} 1 - A - r_y \partial_{r_y} A & r_y \partial_{r_x} A \\ r_y \partial_{r_x} A & -A + r_y \partial_{r_y} A \end{pmatrix} \tag{A.12}$$

$$\begin{aligned} T_{xxx}(\boldsymbol{r}) &= \frac{1}{2\pi} \boldsymbol{\nabla} \cdot [-A, -r_y \partial_{r_x} A], \\ T_{xxy}(\boldsymbol{r}) = T_{xyx}(\boldsymbol{r}) = T_{yxx}(\boldsymbol{r}) &= \frac{1}{2\pi} \boldsymbol{\nabla} \cdot [r_y \partial_{r_x} A, -A], \\ T_{xyy}(\boldsymbol{r}) = T_{yxy}(\boldsymbol{r}) = T_{yyx}(\boldsymbol{r}) &= \frac{1}{2\pi} \boldsymbol{\nabla} \cdot [-A, r_y \partial_{r_x} A], \\ T_{yyy}(\boldsymbol{r}) &= \frac{1}{2\pi} \boldsymbol{\nabla} \cdot [-r_y \partial_{r_x} A, -A]. \end{aligned} \tag{A.13}$$

Note that we have changed the T_{xxx} expression compared to [Pozrikidis, 1992] (written as $\boldsymbol{\nabla} \cdot [-A, -r_y \partial_{r_y} A]$ there). We have verified that $\boldsymbol{\nabla} \cdot [-A, -r_y \partial_{r_x} A]$ is the correct expression by taking the limit of small q, in which the free-space kernel is recovered, as $T_{xxx}(\boldsymbol{r}) = -r_x^3/(\pi r^4) + O(q^2)$.

Numerical integration of Eq. (A.3) requires particular care due to the singular nature of the kernels $\underline{\underline{G}}$ and $\underline{\underline{\underline{T}}}$, which diverge when the distance between $\boldsymbol{r}$ and $\boldsymbol{r}_0$ tends to 0. We overcome this challenge by a combination of several techniques:

- The kernel $\underline{\underline{G}}$ is regularized for $\boldsymbol{r} = \boldsymbol{r}_0$ by singularity subtraction technique, in which we subtract an exact identity from the integral in Eq. (A.3) to make the first integral in Eq. (A.3) go to zero at $\boldsymbol{r} = \boldsymbol{r}_0$ [Farutin et al., 2014].

- While the kernel $\underline{\underline{\underline{T}}}$ diverges at $\boldsymbol{r}_0 = \boldsymbol{r}$, the product $\underline{\underline{\underline{T}}}(\boldsymbol{r}_0, \boldsymbol{r}).\boldsymbol{n}(\boldsymbol{r}_0)$ has a finite limit when $\boldsymbol{r}_0$ approaches $\boldsymbol{r}$ along the particle contour. It is thus sufficient to replace the undefined value of the second integral of Eq. (A.3) for $\boldsymbol{r}_0 = \boldsymbol{r}$ with this limit to regularize the second integral [Quaife and Biros, 2014].

- We further improve the precision of computing the integrals in Eq. (A.3) by using refined meshes to compute the contributions of near-singular points, for which the distance $|\boldsymbol{r}_0 - \boldsymbol{r}|$ is comparable to the spacing between the discretization points for the original coarse mesh. This technique is based on decomposing the Green's kernels into a sum of their smoothly varying long-range part and several short-range parts with finite support [Farutin and Misbah, 2014]. The long-range part is then integrated using the most coarse mesh, while the short-range parts are integrated using more refined meshes, where the mesh refinement is consistent with the characteristic length-scale of the given short-range contribution to the Green's kernel, which is defined by its support. This method provides a good balance between the computational cost, since the number of kernel evaluations is of the same order for each mesh, and the precision of the method, since the discretization errors due to the singular behavior of the kernels are also of the same order for each mesh.

Appendix B

Membrane discretization quality and benchmarking

The vesicle is described at time t by a closed curve $\mathbf{r}(\alpha, t)$ in (x, y) plane. The membrane is discretized into N_{mem} points. To study the effect of the membrane discretization on the shape of the vesicle, we examine the effect of the variation of the N_{mem} on the vesicle shape as shown in the (Fig.B.1). We see clearly in the (Fig.**??**) that all the vesicle configurations are very close. We set $N_{mem} = 1024$ in all the simulations presented in this article.

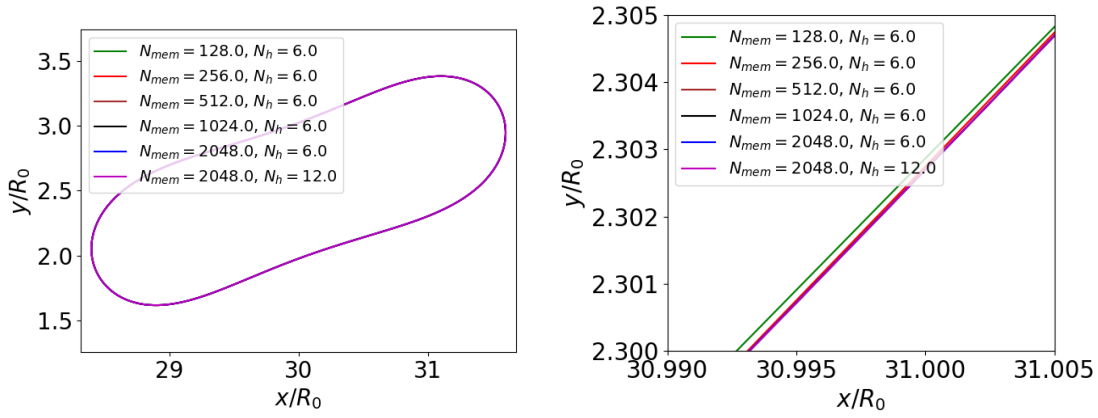

Figure B.1: The configure of the shape while showing a tank-treading. Here we set $C_{0.2}$, $C_a = 1.0$ and $\lambda = 1.0$. Left figure is a zoom of the right figure.

We also investigated the effect of the time step dt on the simulation precision. To do this, We calculated the normalized effective viscosity as described in the Eq. (3.5) for different values of capillary number C_a and the viscosity contrast λ. We see clearly in the (Fig.B.2) that the time step value $dt = 10^{-5}$ is the typical value which is independent on the capillary number C_a and the viscosity contrast λ. For

calculation speed and accuracy purposes, the time step value is fixed to $dt = 10^{-5}$ in all our simulations in this article.

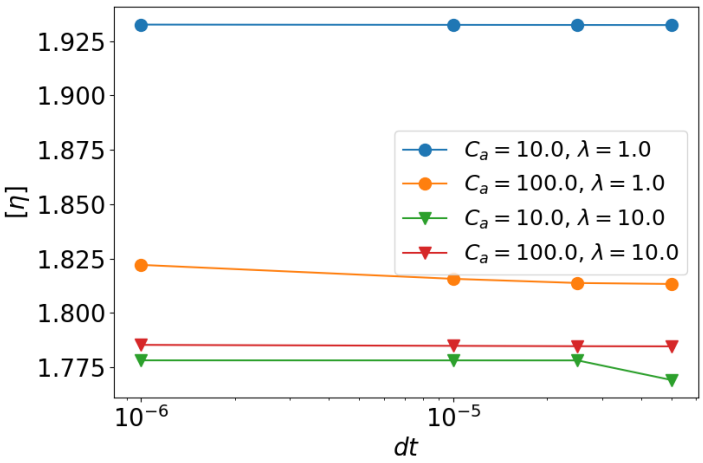

Figure B.2: The normalized effective viscosity as function of the time step for different values of capillary number C_a and viscosity contrast λ. We set here $\tau = 0.65$ and $C_n = 0.2$

Finally, we present here a qualitative and quantitative comparison of our simulations with other method. The selected method is lattice Boltzmann method (LBM). For comparison purposes and code validation we show in the (Fig.B.3) the steady inclination angle of the vesicle as function of the confinement C_n, our simulation result is in a good qualitative and quantitative agreement with LBM [Kaoui et al., 2011].

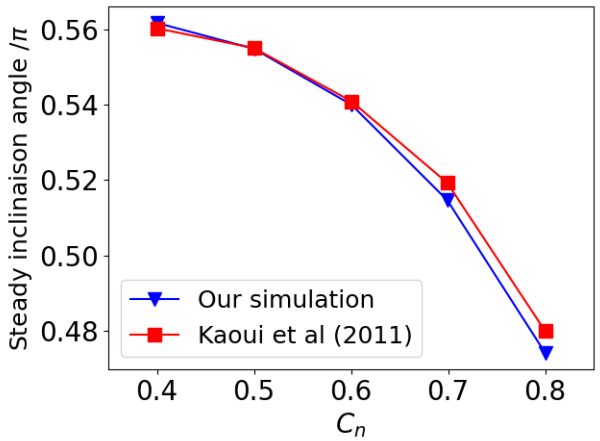

Figure B.3: The variation of the steady inclination angle associated to a vesicle performing tank-treading motion in confined geometries as function of the confinement C_n. We set here $\tau = 0.9$ and $C_a = 1.0$ and $\lambda = 1.0$. The data was extracted from Kaoui et al [Kaoui et al., 2011].

References

[Abbasi et al., 2021] Abbasi, M., Farutin, A., Ez-Zahraouy, H., Benyoussef, A., and Misbah, C. (2021). Erythrocyte-erythrocyte aggregation dynamics under shear flow. *Physical Review Fluids*, 6(2):023602. 41, 42

[Abkarian et al., 2008] Abkarian, M., Faivre, M., Horton, R., Smistrup, K., Best-Popescu, C. A., and Stone, H. A. (2008). Cellular-scale hydrodynamics. *Biomedical materials*, 3(3):034011. 10

[Abkarian et al., 2007] Abkarian, M., Faivre, M., and Viallat, A. (2007). Swinging of red blood cells under shear flow. *Physical review letters*, 98(18):188302. 10, 28

[Advani et al., 1992] Advani, R., Rubin, E., Mohandas, N. a., and Schrier, S. (1992). Oxidative red blood cell membrane injury in the pathophysiology of severe mouse beta-thalassemia. *Blood*, 79(4):1064–1067. 52

[Agarwal and Biros, 2020] Agarwal, D. and Biros, G. (2020). Stable shapes of three-dimensional vesicles in unconfined and confined poiseuille flow. *Physical Review Fluids*, 5(1):013603. 10

[Aidun and Clausen, 2010] Aidun, C. K. and Clausen, J. R. (2010). Lattice-boltzmann method for complex flows. *Annual review of fluid mechanics*, 42:439–472. 18

[Aouane et al., 2021] Aouane, O., Scagliarini, A., and Harting, J. (2021). Structure and rheology of suspensions of spherical strain-hardening capsules. *Journal of Fluid Mechanics*, 911. 19

[Aouane et al., 2014] Aouane, O., Thiébaud, M., Benyoussef, A., Wagner, C., and Misbah, C. (2014). Vesicle dynamics in a confined poiseuille flow: from steady state to chaos. *Physical Review E*, 90(3):033011. 27

[Armstrong et al., 2004] Armstrong, J. K., Wenby, R. B., Meiselman, H. J., and Fisher, T. C. (2004). The hydrodynamic radii of macromolecules and their effect on red blood cell aggregation. *Biophysical journal*, 87(6):4259–4270. 80

[Bagchi et al., 2005] Bagchi, P., Johnson, P. C., and Popel, A. S. (2005). Computational fluid dynamic simulation of aggregation of deformable cells in a shear flow. *Journal of biomechanical engineering*, 127(7):1070–1080. 41

[Balachandra and Siriwardena, 2005] Balachandra, S. and Siriwardena, A. K. (2005). Systematic appraisal of the management of the major vascular complications of pancreatitis. *The American journal of surgery*, 190(3):489–495. 95

[Balogh and Bagchi, 2017] Balogh, P. and Bagchi, P. (2017). A computational approach to modeling cellular-scale blood flow in complex geometry. *Journal of Computational Physics*, 334:280–307. xii, 98

[Barbee and Cokelet, 1971] Barbee, J. H. and Cokelet, G. R. (1971). Prediction of blood flow in tubes with diameters as small as 29 μ. *Microvascular Research*, 3(1):17–21. 68

[Barge and Lopera, 2012] Barge, J. U. and Lopera, J. E. (2012). Vascular complications of pancreatitis: role of interventional therapy. *Korean journal of radiology*, 13(Suppl 1):S45–S55. 95

[Barthes-Biesel, 2016] Barthes-Biesel, D. (2016). Motion and deformation of elastic capsules and vesicles in flow. *Annual Review of fluid mechanics*, 48:25–52. 40

[Baskurt et al., 2011] Baskurt, O., Neu, B., and Meiselman, H. J. (2011). Red blood cell aggregation. iv, 5

[Batchelor, 1970] Batchelor, G. (1970). The stress system in a suspension of force-free particles. *Journal of fluid mechanics*, 41(3):545–570. 34, 54

[Beaucourt et al., 2004] Beaucourt, J., Rioual, F., Séon, T., Biben, T., and Misbah, C. (2004). Steady to unsteady dynamics of a vesicle in a flow. *Physical Review E*, 69(1):011906. 30

[Bertoluzzo et al., 1999] Bertoluzzo, S., Bollini, A., Rasia, M., and Raynal, A. (1999). Kinetic model for erythrocyte aggregation. *Blood cells, molecules, and diseases*, 25(6):339–349. 5, 41

[Betts et al., 2013] Betts, J. G., Young, K. A., Wise, J. A., Johnson, E., Poe, B., Kruse, D. H., Korol, O., Johnson, J. E., Womble, M., and DeSaix, P. (2013). *Anatomy and physiology*. 2

[Bhatnagar et al., 1954] Bhatnagar, P. L., Gross, E. P., and Krook, M. (1954). A model for collision processes in gases. i. small amplitude processes in charged and neutral one-component systems. *Physical review*, 94(3):511. 18

[Biben et al., 2011a] Biben, T., Farutin, A., and Misbah, C. (2011a). Three-dimensional vesicles under shear flow: Numerical study of dynamics and phase diagram. *Physical Review E*, 83(3):031921. 10, 11

[Biben et al., 2011b] Biben, T., Farutin, A., and Misbah, C. (2011b). Three-dimensional vesicles under shear flow: Numerical study of dynamics and phase diagram. *Phys. Rev. E*, 83:031921. 28

[Birchard, 1997] Birchard, G. F. (1997). Optimal hematocrit: theory, regulation and implications. *American Zoologist*, 37(1):65–72. 68

[Brandao et al., 2003] Brandao, M., Fontes, A., Barjas-Castro, M., Barbosa, L., Costa, F., Cesar, C., and Saad, S. (2003). Optical tweezers for measuring red blood cell elasticity: application to the study of drug response in sickle cell disease. *European journal of haematology*, 70(4):207–211. 52

[Bronkhorst et al., 1997] Bronkhorst, P., Grimbergen, J., Brakenhoff, G., Heethaar, R., and Sixma, J. (1997). The mechanism of red cell (dis) aggregation investigated by means of direct cell manipulation using multiple optical trapping. *British Journal of Haematology*, 96(2):256–258. 6

[Brooks, 1988] Brooks, D. (1988). Mechanism of red cell aggregation. In *Blood Cells, Rheology, and Aging*, pages 158–162. Springer. 4

[Brust et al., 2014] Brust, M., Aouane, O., Thiébaud, M., Flormann, D., Verdier, C., Kaestner, L., Laschke, M., Selmi, H., Benyoussef, A., Podgorski, T., et al. (2014). The plasma protein fibrinogen stabilizes clusters of red blood cells in microcapillary flows. *Scientific reports*, 4(1):1–6. xiii, 3, 6, 11, 42, 43, 57, 80, 84

[Chen and Liu, 2012] Chen, C.-K. and Liu, T.-M. (2012). Imaging morphodynamics of human blood cells in vivo with video-rate third harmonic generation microscopy. *Biomedical optics express*, 3(11):2860–2865. 27

[Chen et al., 1995] Chen, S., Gavish, B., Zhang, S., Mahler, Y., and Yedgar, S. (1995). Monitoring of erythrocyte aggregate morphology under flow by computerized image analysis. *Biorheology*, 32(4):487–496. 86

[Chien, 1975] Chien, S. (1975). Biophysical behavior of red cells in suspensions. *The red blood cell*, 2:1031–1133. 80

[Chien et al., 1990] Chien, S., Feng, S.-s., Vayo, M., Sung, L. A., Usami, S., and Skalak, R. (1990). The dynamics of shear disaggregation of red blood cells in a flow channel. *Biorheology*, 27(2):135–147. 48, 52

[Chien and Jan, 1973] Chien, S. and Jan, K.-m. (1973). Ultrastructural basis of the mechanism of rouleaux formation. *Microvascular research*, 5(2):155–166. 4, 88

[Chien et al., 1967] Chien, S., Usami, S., Dellenback, R. J., Gregersen, M. I., Nanninga, L. B., and Guest, M. M. (1967). Blood viscosity: influence of erythrocyte aggregation. *Science*, 157(3790):829–831. 6

[Clavería et al., 2016] Clavería, V., Aouane, O., Thiébaud, M., Abkarian, M., Coupier, G., Misbah, C., John, T., and Wagner, C. (2016). Clusters of red blood cells in microcapillary flow: hydrodynamic versus macromolecule induced interaction. *Soft Matter*, 12(39):8235–8245. 11, 88

[Comeglio et al., 1996] Comeglio, P., Fedi, S., Liotta, A. A., Cellai, A. P., Chiarantini, E., Prisco, D., Mecacci, F., Parretti, E., Mello, G., and Abbate, R. (1996). Blood clotting activation during normal pregnancy. *Thrombosis research*, 84(3):199–202. 3

[Cordasco et al., 2014] Cordasco, D., Yazdani, A., and Bagchi, P. (2014). Comparison of erythrocyte dynamics in shear flow under different stress-free configurations. *Physics of Fluids*, 26(4):041902. 28

[Coupier et al., 2012] Coupier, G., Farutin, A., Minetti, C., Podgorski, T., and Misbah, C. (2012). Shape diagram of vesicles in poiseuille flow. *Physical review letters*, 108(17):178106. 10

[Crowdy and Or, 2010] Crowdy, D. G. and Or, Y. (2010). Two-dimensional point singularity model of a low-reynolds-number swimmer near a wall. *Phys. Rev. E*, 81:036313. 38

[Dalal et al., 2020] Dalal, S., Farutin, A., and Misbah, C. (2020). Amoeboid swimming in a compliant channel. *Soft Matter*, 16(6):1599–1613. 16

[Danker et al., 2007] Danker, G., Biben, T., Podgorski, T., Verdier, C., and Misbah, C. (2007). Dynamics and rheology of a dilute suspension of vesicles: Higher-order theory. *Phys. Rev. E*, 76:041905. 96

[Danker and Misbah, 2007] Danker, G. and Misbah, C. (2007). Rheology of a dilute suspension of vesicles. *Phys. Rev. Lett.*, 98:088104. 37

[Deschamps et al., 2009] Deschamps, J., Kantsler, V., and Steinberg, V. (2009). Phase diagram of single vesicle dynamical states in shear flow. *Physical review letters*, 102(11):118105. 28

[Di Liberto and Bartolucci, 2016] Di Liberto, G., K. L. M. M. B. L. P. F. C. M. R. M. H. A. K. S. V. B. M. B. G. F. P. F. and Bartolucci, P. (2016). Dense red blood cell and oxygen desaturation in sickle-cell disease. *American journal of hematology*, 91(10):1008–1013. 3

[Dunn and Ariëns, 2004] Dunn, E. J. and Ariëns, R. A. (2004). Fibrinogen and fibrin clot structure in diabetes. *Herz*, 29(5):470–479. 3, 4

[Dupire et al., 2012] Dupire, J., Socol, M., and Viallat, A. (2012). Full dynamics of a red blood cell in shear flow. *Proceedings of the National Academy of Sciences*, 109(51):20808–20813. 10, 28

[Fåhraeus, 1929] Fåhraeus, R. (1929). The suspension stability of the blood. *Physiological reviews*, 9(2):241–274. 4, 80

[FÅHRAEUS, 1958] FÅHRAEUS, R. (1958). The influence of the rouleau formation of the erythrocytes on the rheology of the blood. *Acta Medica Scandinavica*, 161(2):151–165. 4

[Fahraeus and Lindqvist, 1931] Fahraeus, R. and Lindqvist, T. (1931). The viscosity of the blood in narrow capillary tubes. *American Journal of Physiology-Legacy Content*, 96(3):562–568. 4, 6

[Farutin et al., 2010] Farutin, A., Biben, T., and Misbah, C. (2010). Analytical progress in the theory of vesicles under linear flow. *Phys. Rev. E*, 81:061904. 96

[Farutin et al., 2014] Farutin, A., Biben, T., and Misbah, C. (2014). 3d numerical simulations of vesicle and inextensible capsule dynamics. *Journal of Computational Physics*, 275:539–568. 28, 105

[Farutin and Misbah, 2012] Farutin, A. and Misbah, C. (2012). Squaring, parity breaking, and s tumbling of vesicles under shear flow. *Phys. Rev. Lett.*, 109:248106. 10

[Farutin and Misbah, 2014] Farutin, A. and Misbah, C. (2014). Symmetry breaking and cross-streamline migration of three-dimensional vesicles in an axial poiseuille flow. *Physical review E*, 89(4):042709. 105

[Farutin et al., 2018] Farutin, A., Shen, Z., Prado, G., Audemar, V., Ez-Zahraouy, H., Benyoussef, A., Polack, B., Harting, J., Vlahovska, P. M., Podgorski, T., et al. (2018). Optimal cell transport in straight channels and networks. *Physical review fluids*, 3(10):103603. 69, 73

[Fedosov et al., 2014] Fedosov, D. A., Peltomäki, M., and Gompper, G. (2014). Deformation and dynamics of red blood cells in flow through cylindrical microchannels. *Soft matter*, 10(24):4258–4267. 10

[Fischer and Schmid-Schönbein, 1978] Fischer, T. and Schmid-Schönbein, H. (1978). Tank tread motion of red cell membranes in viscometric flow: behavior of intracellular and extracellular markers (with film). In *Red Cell Rheology*, pages 347–361. Springer. 28

[Fischer et al., 1978a] Fischer, T., Stohr-Lissen, M., and Schmid-Schonbein, H. (1978a). The red cell as a fluid droplet: tank tread-like motion of the human erythrocyte membrane in shear flow. *Science*, 202(4370):894–896. 96

[Fischer and Korzeniewski, 2013a] Fischer, T. M. and Korzeniewski, R. (2013a). Threshold shear stress for the transition between tumbling and tank-treading of red blood cells in shear flow: dependence on the viscosity of the suspending medium. *Journal of fluid mechanics*, 736:351. 10

[Fischer and Korzeniewski, 2013b] Fischer, T. M. and Korzeniewski, R. (2013b). Threshold shear stress for the transition between tumbling and tank-treading of red blood cells in shear flow: dependence on the viscosity of the suspending medium. *Journal of Fluid Mechanics*, 736:351–365. 52, 61

[Fischer et al., 1978b] Fischer, T. M., Stohr-Lissen, M., and Schmid-Schonbein, H. (1978b). The red cell as a fluid droplet: tank tread-like motion of the human erythrocyte membrane in shear flow. *Science*, 202(4370):894–896. 10

[Flormann et al., 2017] Flormann, D., Aouane, O., Kaestner, L., Ruloff, C., Misbah, C., Podgorski, T., and Wagner, C. (2017). The buckling instability of aggregating red blood cells. *Scientific reports*, 7(1):1–10. vi, 5, 6, 11, 41, 42, 43, 45, 47, 86

[Fontes et al., 2008] Fontes, A., Fernandes, H. P., de Thomaz, A. A., Barbosa, L. C., Barjas-Castro, M. L., and Cesar, C. L. (2008). Measuring electrical and mechanical properties of red blood cells with double optical tweezers. *Journal of Biomedical Optics*, 13(1):014001. 6

[Foresto et al., 2000] Foresto, P., D Arrigo, M., Carreras, L., Cuezzo, R. E., Valverde, J., and Rasia, R. (2000). Evaluation of red blood cell aggregation in diabetes by computarized image analysis. *MEDICINA-BUENOS AIRES-*, 60(5; PART 1):570–572. 3, 86

[Forsyth et al., 2011] Forsyth, A. M., Wan, J., Owrutsky, P. D., Abkarian, M., and Stone, H. A. (2011). Multiscale approach to link red blood cell dynamics, shear viscosity, and atp release. *Proceedings of the National Academy of Sciences*, 108(27):10986–10991. 57

[Franke et al., 2011] Franke, T., Hoppe, R. H., Linsenmann, C., Schmid, L., Willbold, C., and Wixforth, A. (2011). Numerical simulation of the motion of red blood cells and vesicles in microfluidic flows. *Computing and visualization in science*, 14(4):167–180. 40

[Frossard et al., 2000] Frossard, J. L., Robert, J., Soravia, C., Mensi, N., Magnin, A., Hadengue, A., Rohner, A., and Morel, P. (2000). Early prediction in acute pancreatitis: the contribution of amylase and lipase levels in peritoneal fluid. *JOP. Journal of the Pancreas*, 1(2):36–45. 85, 86, 88

[Fusman et al., 2002] Fusman, G., Mardi, T., Justo, D., Rozenblat, M., Rotstein, R., Zeltser, D., Rubinstein, A., Koffler, M., Shabtai, E., Berliner, S., et al. (2002). Red blood cell adhesiveness/aggregation, c-reactive protein, fibrinogen, and erythrocyte sedimentation rate in healthy adults and in those with atherosclerotic risk factors. *American Journal of Cardiology*, 90(5):561–563. 3

[Glenister et al., 2002] Glenister, F. K., Coppel, R. L., Cowman, A. F., Mohandas, N., and Cooke, B. M. (2002). Contribution of parasite proteins to altered mechanical properties of malaria-infected red blood cells. *Blood*, 99(3):1060–1063. 52

[Goldsmith et al., 1972] Goldsmith, H., Marlow, J., and MacIntosh, F. C. (1972). Flow behaviour of erythrocytes-i. rotation and deformation in dilute suspensions. *Proceedings of the Royal Society of London. Series B. Biological Sciences*, 182(1068):351–384. 28

[Gou et al., 2021] Gou, Z., Zhang, H., Abbasi, M., and Misbah, C. (2021). Red blood cells under flow show maximal atp release for specific hematocrit. *Biophysical Journal*, 120(21):4819–4831. 69

[Groeneveld et al., 1999] Groeneveld, Y., Petri, H., Hermans, J., and Springer, M. (1999). Relationship between blood glucose level and mortality in type 2 diabetes mellitus: a systematic review. *Diabetic medicine*, 16(1):2–13. 3, 84

[Guckenberger et al., 2018] Guckenberger, A., Kihm, A., John, T., Wagner, C., and Gekle, S. (2018). Numerical–experimental observation of shape bistability of red blood cells flowing in a microchannel. *Soft Matter*, 14(11):2032–2043. 11, 28

[Hedrick et al., 1986] Hedrick, M. S., Duffield, D. A., and Cornell, L. H. (1986). Blood viscosity and optimal hematocrit in a deep-diving mammal, the northern elephant seal (mirounga angustirostris). *Canadian Journal of Zoology*, 64(10):2081–2085. 68

[Helfrich, 1973] Helfrich, W. (1973). Elastic properties of lipid bilayers: theory and possible experiments. *Zeitschrift für Naturforschung c*, 28(11-12):693–703. 13

[Hodgkin and Lister, 1827] Hodgkin, D. and Lister, J. J. (1827). Xxvi. notice of some miscroscopic observations of the blood and animal tissues. *The Philosophical Magazine*, 2(8):130–138. 4

[Hoore et al., 2018] Hoore, M., Yaya, F., Podgorski, T., Wagner, C., Gompper, G., and Fedosov, D. A. (2018). Effect of spectrin network elasticity on the shapes of erythrocyte doublets. *Soft matter*, 14(30):6278–6289. ix, 5, 42, 43, 66, 86

[Huisman et al., 1988] Huisman, A., Aarnoudse, J., Krans, M., Huisjes, H., Fidler, V., and Zijlstra, W. (1988). Red cell aggregation during normal pregnancy. *British journal of haematology*, 68(1):121–124. 4

[Jiang et al., 2021] Jiang, X. Z., Goligorsky, M. S., and Luo, K. H. (2021). Cross talk between endothelial and red blood cell glycocalyces via near-field flow. *Biophysical Journal*, 120(15):3180–3191. 2

[Ju et al., 2013] Ju, M., Ye, S. S., Low, H. T., Zhang, J., Cabrales, P., Leo, H. L., and Kim, S. (2013). Effect of deformability difference between two erythrocytes on their aggregation. *Physical biology*, 10(3):036001. 5, 41

[Kantsler et al., 2008] Kantsler, V., Segre, E., and Steinberg, V. (2008). Dynamics of interacting vesicles and rheology of vesicle suspension in shear flow. *EPL (Europhysics Letters)*, 82(5):58005. 10

[Kaoui et al., 2009a] Kaoui, B., Biros, G., and Misbah, C. (2009a). Why do red blood cells have asymmetric shapes even in a symmetric flow? *Physical review letters*, 103(18):188101. 10, 11, 27

[Kaoui et al., 2009b] Kaoui, B., Farutin, A., and Misbah, C. (2009b). Vesicles under simple shear flow: elucidating the role of relevant control parameters. *Physical review. E*, 80 6 Pt 1:061905. 11, 30

[Kaoui and Harting, 2016] Kaoui, B. and Harting, J. (2016). Two-dimensional lattice boltzmann simulations of vesicles with viscosity contrast. *Rheologica Acta*, 55(6):465–475. 30

[Kaoui et al., 2011] Kaoui, B., Harting, J., and Misbah, C. (2011). Two-dimensional vesicle dynamics under shear flow: Effect of confinement. *Physical Review E*, 83(6):066319. xii, 30, 107

[Kaoui et al., 2012] Kaoui, B., Krüger, T., and Harting, J. (2012). How does confinement affect the dynamics of viscous vesicles and red blood cells? *Soft Matter*, 8(35):9246–9252. 28

[Kaoui et al., 2008] Kaoui, B., Ristow, G., Cantat, I., Misbah, C., and Zimmermann, W. (2008). Lateral migration of a two-dimensional vesicle in unbounded poiseuille flow. *Physical Review E*, 77(2):021903. 11

[Kaul, 2008] Kaul, D. (2008). Sickle red cell adhesion: Many issues and some answers. *Transfusion clinique et biologique*, 15(1-2):51–55. 3

[Keller and Skalak, 1982] Keller, S. R. and Skalak, R. (1982). Motion of a tank-treading ellipsoidal particle in a shear flow. *Journal of Fluid Mechanics*, 120:27–47. 10

[Kessler et al., 2009] Kessler, S., Finken, R., and Seifert, U. (2009). Elastic capsules in shear flow: Analytical solutions for constant and time-dependent shear rates. *The European Physical Journal E*, 29(4):399–413. 10

[Kihm et al., 2018] Kihm, A., Kaestner, L., Wagner, C., and Quint, S. (2018). Classification of red blood cell shapes in flow using outlier tolerant machine learning. *PLoS computational biology*, 14(6):e1006278. 27

[Kim and Lai, 2012] Kim, Y. and Lai, M.-C. (2012). Numerical study of viscosity and inertial effects on tank-treading and tumbling motions of vesicles under shear flow. *Physical Review E*, 86(6):066321. 30

[Kirby et al., 2008] Kirby, J. M., Vora, P., Midia, M., and Rawlinson, J. (2008). Vascular complications of pancreatitis: imaging and intervention. *Cardiovascular and interventional radiology*, 31(5):957–970. 95

[Krüger et al., 2017] Krüger, T., Kusumaatmaja, H., Kuzmin, A., Shardt, O., Silva, G., and Viggen, E. M. (2017). The lattice boltzmann method. *Springer International Publishing*, 10(978-3):4–15. 18

[Krüger et al., 2011] Krüger, T., Varnik, F., and Raabe, D. (2011). Efficient and accurate simulations of deformable particles immersed in a fluid using a combined immersed boundary lattice boltzmann finite element method. *Computers & Mathematics with Applications*, 61(12):3485–3505. 14

[Laadhari et al., 2010] Laadhari, A., Misbah, C., and Saramito, P. (2010). On the equilibrium equation for a generalized biological membrane energy by using a shape optimization approach. *Physica D: Nonlinear Phenomena*, 239(16):1567–1572. 14

[Lanotte et al., 2016] Lanotte, L., Mauer, J., Mendez, S., Fedosov, D. A., Fromental, J.-M., Claveria, V., Nicoud, F., Gompper, G., and Abkarian, M. (2016). Red cells' dynamic morphologies govern blood shear thinning under microcirculatory flow conditions. *Proc. Natl. Acad. Sci. U.S.A*, 113(47):13289–13294. 27, 28, 32, 35, 96

[Lebedev et al., 2007] Lebedev, V. V., Turitsyn, K. S., and Vergeles, S. S. (2007). Dynamics of nearly spherical vesicles in an external flow. *Phys. Rev. Lett.*, 99:218101. 96

[Lee et al., 2016] Lee, K., Kinnunen, M., Khokhlova, M. D., Lyubin, E. V., Priezzhev, A. V., Meglinski, I., and Fedyanin, A. A. (2016). Optical tweezers study of red blood cell aggregation and disaggregation in plasma and protein solutions. *Journal of biomedical optics*, 21(3):035001. 6

[Lemonne and Etienne-Julan, 2012] Lemonne, N., C. P. R. M. V. J. B. V. L. Y. and Etienne-Julan, M. (2012). Increased blood viscosity and red blood cell aggregation in a patient with sickle cell anemia and smoldering myeloma. *American journal of hematology*, 87(11):E129–E129. 3

[Linderkamp et al., 1992] Linderkamp, O., Stadler, A. A., and Zilow, E. P. (1992). Blood viscosity and optimal hematocrit in preterm and full-term neonates in 50–to 500–μm tubes. *Pediatric research*, 32(1):97–102. 68

[Lipowsky et al., 1980] Lipowsky, H. H., Usami, S., and Chien, S. (1980). In vivo measurements of "apparent viscosity" and microvessel hematocrit in the mesentery of the cat. *Microvascular research*, 19(3):297–319. 68

[Lugovtsov et al., 2019] Lugovtsov, A. E., Gurfinkel, Y. I., Ermolinskiy, P. B., Maslyanitsina, A. I., Dyachuk, L. I., and Priezzhev, A. V. (2019). Optical assessment of alterations of microrheologic and microcirculation parameters in cardiovascular diseases. *Biomed. Opt. Express*, 10(8):3974–3986. 3

[Maeda and Shiga, 1985] Maeda, N. and Shiga, T. (1985). Inhibition and acceleration of erythrocyte aggregation induced by small macromolecules. *Biochimica et Biophysica Acta (BBA)-General Subjects*, 843(1-2):128–136. 88

[Maklygin et al., 2012] Maklygin, A. Y., Priezzhev, A. V., Karmenian, A., Nikitin, S. Y., Obolenskii, I., Lugovtsov, A. E., and Li, K. (2012). Measurement of interaction forces between red blood cells in aggregates by optical tweezers. *Quantum Electronics*, 42(6):500. 6

[Markin et al., 1998] Markin, A., Strogonova, L., Balashov, O., Polyakov, V., and Tigner, T. (1998). The dynamics of blood biochemical parameters in cosmonauts during long-term space flights. *Acta astronautica*, 42(1-8):247–253. 85

[Mauer et al., 2018] Mauer, J., Mendez, S., Lanotte, L., Nicoud, F., Abkarian, M., Gompper, G., and Fedosov, D. A. (2018). Flow-induced transitions of red blood cell shapes under shear. *Phys. Rev. Lett.*, 121:118103. 27, 28, 29, 30, 32, 63, 96

[Mazzanti et al., 1997] Mazzanti, L., Rabini, R. A., Salvolini, E., Tesei, M., Martarelli, D., Venerando, B., and Curatola, G. (1997). Sialic acid, diabetes, and aging: a study on the erythrocyte membrane. *Metabolism*, 46(1):59–61. 3

[Menu et al., 2000] Menu, P., Bleeker, W., Longrois, D., Caron, A., Faivre-Fiorina, B., Muller, S., Labrude, P., and Stoltz, J.-F. (2000). In vivo effects of hb solutions on blood viscosity and rheologic behavior of rbcs: comparison with clinically used volume expanders. *Transfusion*, 40(9):1095–1103. 80

[Merrill et al., 1963] Merrill, E., Gilliland, E., Cokelet, G., Shin, H., Britten, A., and Wells Jr, R. (1963). Rheology of blood and flow in the microcirculation. *Journal of applied physiology*, 18(2):255–260. 80

[Minetti et al., 2019] Minetti, C., Audemar, V., Podgorski, T., and Coupier, G. (2019). Dynamics of a large population of red blood cells under shear flow. *Journal of Fluid Mechanics*, 864:408–448. 10

[Misbah, 2006a] Misbah, C. (2006a). Vacillating breathing and tumbling of vesicles under shear flow. *Phys. Rev. Lett.*, 96:028104. 10, 28

[Misbah, 2006b] Misbah, C. (2006b). Vacillating breathing and tumbling of vesicles under shear flow. *Phys. Rev. Lett.*, 96:028104. 96

[Misbah, 2012] Misbah, C. (2012). Vesicles, capsules and red blood cells under flow. *Journal of Physics: Conference Series*, 392(1):012005. 40

[Nader et al., 2019] Nader, E., Skinner, S., Romana, M., Fort, R., Lemonne, N., Guillot, N., Gauthier, A., Antoine-Jonville, S., Renoux, C., Hardy-Dessources, M.-D., et al. (2019). Blood rheology: key parameters, impact on blood flow, role in sickle cell disease and effects of exercise. *Frontiers in physiology*, 10:1329. 6

[Nait-Ouhra et al., 2018a] Nait-Ouhra, A., Farutin, A., Aouane, O., Ez-Zahraouy, H., Benyoussef, A., and Misbah, C. (2018a). Shear thinning and shear thickening of a confined suspension of vesicles. *Physical Review E*, 97(1):012404. 34, 55

[Nait-Ouhra et al., 2018b] Nait-Ouhra, A., Guckenberger, A., Farutin, A., Ez-Zahraouy, H., Benyoussef, A., Gekle, S., and Misbah, C. (2018b). Lateral vesicle migration in a bounded shear flow: Viscosity contrast leads to off-centered solutions. *Physical Review Fluids*, 3(12):123601. 11

[Noguchi and Gompper, 2007] Noguchi, H. and Gompper, G. (2007). Swinging and tumbling of fluid vesicles in shear flow. *Physical review letters*, 98(12):128103. 28

[Oshima et al., 2017] Oshima, K., Haeger, S. M., Hippensteel, J. A., Herson, P. S., and Schmidt, E. P. (2017). More than a biomarker: the systemic consequences of heparan sulfate fragments released during endothelial surface layer degradation (2017 grover conference series). *Pulmonary circulation*, 8(1):2045893217745786. iv, 3

[Peskin, 1977] Peskin, C. S. (1977). Numerical analysis of blood flow in the heart. *Journal of computational physics*, 25(3):220–252. 19

[Peskin, 2002] Peskin, C. S. (2002). The immersed boundary method. *Acta numerica*, 11:479–517. 19

[Popel and Johnson, 2005] Popel, A. S. and Johnson, P. C. (2005). Microcirculation and hemorheology. *Annual review of fluid mechanics*, 37:43. xiii, 2

[Popper and Necheles, 1940] Popper, H. and Necheles, H. (1940). Pathways of enzymes into the blood in acute damage of the pancreas. *Proceedings of the Society for Experimental Biology and Medicine*, 43(1):220–222. 85, 86, 88

[Pot et al., 2011] Pot, C., Chen, A. Y., Ha, J. N., and Schmid-Schönbein, G. W. (2011). Proteolytic cleavage of the red blood cell glycocalyx in a genetic form of hypertension. *Cellular and molecular bioengineering*, 4(4):678–692. 85

[Potron et al., 1994] Potron, G., Nguyen, P., and Pignon, B. (1994). Fibrinogen, arterial risk factor, in clinical practice. *Clinical Hemorheology and Microcirculation*, 14(6):739–767. 3, 4

[Pozrikidis, 1992] Pozrikidis, C. (1992). *Boundary integral and singularity methods for linearized viscous flow*. Cambridge University Press. 16, 101, 102, 103, 104

[Pozrikidis, 2005] Pozrikidis, C. (2005). Numerical simulation of cell motion in tube flow. *Annals of Biomedical Engineering*, 33(2):165–178. 10

[Prasad and Kalra, 1993] Prasad, K. and Kalra, J. (1993). Oxygen free radicals and hypercholesterolemic atherosclerosis: effect of vitamin e. *American heart journal*, 125(4):958–973. 3, 84

[Quaife and Biros, 2014] Quaife, B. and Biros, G. (2014). High-volume fraction simulations of two-dimensional vesicle suspensions. *Journal of Computational Physics*, 274:245–267. 105

[Quaife et al., 2019] Quaife, B., Veerapaneni, S., and Young, Y.-N. (2019). Hydrodynamics and rheology of a vesicle doublet suspension. *Phys. Rev. Fluids*, 4:103601. 5, 42

[Quéguiner and Barthès-Biesel, 1997] Quéguiner, C. and Barthès-Biesel, D. (1997). Axisymmetric motion of capsules through cylindrical channels. *Journal of fluid mechanics*, 348:349–376. 10

[Quint et al., 2017] Quint, S., Christ, A., Guckenberger, A., Himbert, S., Kaestner, L., Gekle, S., and Wagner, C. (2017). 3d tomography of cells in micro-channels. *Applied Physics Letters*, 111(10):103701. 28

[Rajendran et al.,] Rajendran, P., Rengarajan, T., Thangavel, J., Nishigaki, Y., and Sakthisekaran, D. Sethi g et al.(2013 nov 9) the vascular endothelium and human diseases. *Int J Biol Sci*, 9:1057–1069. 2, 95

[Razavian et al., 1994] Razavian, S., Atger, V., Giral, P., Cambillau, M., Del-Pino, M., Simon, A., Moatti, N., and Levenson, J. (1994). Influence of hdl subfractions on erythrocyte aggregation in hypercholesterolemic men. pcvmetra group. *Arteriosclerosis, Thrombosis, and Vascular Biology*, 14(3):361–366. 3

[Razavian et al., 1992] Razavian, S. M., Del Pino, M., Simon, A., and Levenson, J. (1992). Increase in erythrocyte disaggregation shear stress in hypertension. *Hypertension*, 20(2):247–252. 3, 4

[Richards and Nwose, 2010] Richards, R. and Nwose, E. (2010). Blood viscosity at different stages of diabetes pathogenesis. *British journal of biomedical science*, 67(2):67–70. 6

[Rogers et al., 1992] Rogers, M. E., Williams, D. T., Niththyananthan, R., Rampling, M. W., Heslop, K. E., and Johnston, D. G. (1992). Decrease in erythrocyte glycophorin sialic acid content is associated with increased erythrocyte aggregation in human diabetes. *Clinical science (London, England: 1979)*, 82(3):309–313. 3, 84

[Salzer et al., 2002] Salzer, U., Hinterdorfer, P., Hunger, U., Borken, C., and Prohaska, R. (2002). Ca++-dependent vesicle release from erythrocytes involves

stomatin-specific lipid rafts, synexin (annexin vii), and sorcin. *Blood, The Journal of the American Society of Hematology*, 99(7):2569–2577. 26

[Schmid-Schönbein and Wells, 1969] Schmid-Schönbein, H. and Wells, R. (1969). Fluid drop-like transition of erythrocytes under shear. *Science*, 165(3890):288–291. 28

[Schwiebert and Zsembery, 2003] Schwiebert, E. M. and Zsembery, A. (2003). Extracellular atp as a signaling molecule for epithelial cells. *Biochimica et Biophysica Acta (BBA) - Biomembranes*, 1615(1-2):7–32. 1

[Seifert, 1999] Seifert, U. (1999). Fluid membranes in hydrodynamic flow fields: Formalism and an application to fluctuating quasispherical vesicles in shear flow. *The European Physical Journal B-Condensed Matter and Complex Systems*, 8(3):405–415. 10

[Shen et al., 2017] Shen, Z., Farutin, A., Thiébaud, M., and Misbah, C. (2017). Interaction and rheology of vesicle suspensions in confined shear flow. *Physical Review Fluids*, 2(10):103101. 69

[Shen et al., 2018] Shen, Z., Fischer, T. M., Farutin, A., Vlahovska, P. M., Harting, J., and Misbah, C. (2018). Blood crystal: emergent order of red blood cells under wall-confined shear flow. *Physical review letters*, 120(26):268102. 40

[Sheremet'ev et al., 2019] Sheremet'ev, Y. A., Popovicheva, A. N., Rogozin, M. M., and Levin, G. Y. (2019). Red blood cell aggregation, disaggregation and aggregate morphology in autologous plasma and serum in diabetic foot disease. *Clinical Hemorheology and Microcirculation*, 72(3):221–227. 86

[Shi et al., 2013] Shi, X., Wang, S., and Zhang, S. (2013). Numerical simulation of the transient shape of the red blood cell in microcapillary flow. *Journal of fluids and structures*, 36:174–183. 28

[Skalak and Branemark, 1969] Skalak, R. and Branemark, P. (1969). Deformation of red blood cells in capillaries. *Science*, 164(3880):717–719. 27

[Smart and Leighton, 1991] Smart, J. R. and Leighton, D. T. (1991). Measurement of the drift of a droplet due to the presence of a plane. *Physics of Fluids A: Fluid Dynamics*, 3(1):21–28. 38

[Steffen et al., 2013] Steffen, P., Verdier, C., and Wagner, C. (2013). Quantification of depletion-induced adhesion of red blood cells. *Physical review letters*, 110(1):018102. 6, 88

[Succi, 2001] Succi, S. (2001). *The lattice Boltzmann equation: for fluid dynamics and beyond*. Oxford university press. 18

[Thiébaud and Misbah, 2013] Thiébaud, M. and Misbah, C. (2013). Rheology of a vesicle suspension with finite concentration: A numerical study. *Physical Review E*, 88(6):062707. 102

[Thiébaud et al., 2014] Thiébaud, M., Shen, Z., Harting, J., and Misbah, C. (2014). Prediction of anomalous blood viscosity in confined shear flow. *Physical review letters*, 112(23):238304. 34, 40

[Tomaiuolo, 2014] Tomaiuolo, G. (2014). Biomechanical properties of red blood cells in health and disease towards microfluidics. *Biomicrofluidics*, 8(5):051501. 1

[Tomaiuolo et al., 2009] Tomaiuolo, G., Simeone, M., Martinelli, V., Rotoli, B., and Guido, S. (2009). Red blood cell deformation in microconfined flow. *Soft Matter*, 5(19):3736–3740. 10, 27

[Tran-Son-Tay et al., 1984] Tran-Son-Tay, R., Sutera, S., and Rao, P. (1984). Determination of red blood cell membrane viscosity from rheoscopic observations of tank-treading motion. *Biophysical journal*, 46(1):65–72. 28

[Trozzo et al., 2015] Trozzo, R., Boedec, G., Leonetti, M., and Jaeger, M. (2015). Axisymmetric boundary element method for vesicles in a capillary. *Journal of Computational Physics*, 289:62–82. 10

[Veerapaneni et al., 2009] Veerapaneni, S. K., Gueyffier, D., Zorin, D., and Biros, G. (2009). A boundary integral method for simulating the dynamics of inextensible vesicles suspended in a viscous fluid in 2d. *Journal of Computational Physics*, 228(7):2334–2353. 16

[Vennemann et al., 2007] Vennemann, P., Lindken, R., and Westerweel, J. (2007). In vivo whole-field blood velocity measurement techniques. *Experiments in fluids*, 42(4):495–511. 15

[Vitkova et al., 2008] Vitkova, V., Mader, M.-A., Polack, B., Misbah, C., and Podgorski, T. (2008). Micro-macro link in rheology of erythrocyte and vesicle suspensions. *Biophysical journal*, 95(6):L33–L35. 40

[Vlahovska et al., 2009] Vlahovska, P. M., Podgorski, T., and Misbah, C. (2009). Vesicles and red blood cells in flow: From individual dynamics to rheology. *Comptes Rendus Physique*, 10(8):775–789. 40

[Yazdani and Bagchi, 2011] Yazdani, A. Z. K. and Bagchi, P. (2011). Phase diagram and breathing dynamics of a single red blood cell and a biconcave capsule in dilute shear flow. *Phys. Rev. E*, 84:026314. 52, 61

[Zhang et al., 2018a] Zhang, H., Shen, Z., Hogan, B., Barakat, A. I., and Misbah, C. (2018a). Atp release by red blood cells under flow: Model and simulations. *Biophys J*, 115(11):2218–2229. 1

[Zhang et al., 2018b] Zhang, H., Shen, Z., Hogan, B., Barakat, A. I., and Misbah, C. (2018b). Atp release by red blood cells under flow: model and simulations. *Biophysical journal*, 115(11):2218–2229. 57

[Zhao and Shaqfeh, 2011] Zhao, H. and Shaqfeh, E. S. (2011). The dynamics of a vesicle in simple shear flow. *Journal of Fluid Mechanics*, 674:578. 10

[Zhong-Can and Helfrich, 1989] Zhong-Can, O.-Y. and Helfrich, W. (1989). Bending energy of vesicle membranes: General expressions for the first, second, and third variation of the shape energy and applications to spheres and cylinders. *Physical Review A*, 39(10):5280. 11, 14